UNIVERSITY OF CALIFORNIA SAN DIEGO

Microfluidic technologies for investigating dynamics-based regulation in *S. cerevisiae*

A dissertation submitted in partial satisfaction of the
requirements for the degree
Doctor of Philosophy

in

Bioengineering (with a specialization in Quantitative Biology)

by

Richard O'Laughlin

Committee in charge:

Professor Jeff Hasty, Chair
Professor Nan Hao
Professor Lorraine Pillus
Professor Elizabeth Villa
Professor Yingxiao Wang

2020

The dissertation of Richard O'Laughlin is approved, and it is acceptable in quality and form for publication on microfilm and electronically:

_____

_____

_____

_____

_____

Chair

University of California San Diego

2020

DEDICATION

To my amazing parents.

EPIGRAPH

Through so many hard straits, so many twists and turns

our course holds firm for Latium.

—Virgil, *The Aeneid*

Robert Fagles translation,

Penguin Classics, 2006

TABLE OF CONTENTS

Signature Page . . . iii

Dedication . . . iv

Epigraph . . . v

Table of Contents . . . vi

List of Figures . . . ix

List of Tables . . . xi

Acknowledgements . . . xii

Vita . . . xvi

Abstract of the Dissertation . . . xvii

Chapter 1 Introduction . . . 1
1.1 Quantitative Biology: searching for the design principles of biological systems . . . 1
1.2 Microfluidics and time-lapse fluorescence microscopy for quantitative biology . . . 2
1.2.1 Dynamics-based regulation in biology at the single-cell level 3
1.3 Thesis overview . . . 4

Chapter 2 Microfluidic technologies for single-cell analysis of yeast . . . 5
2.1 Introduction . . . 5
2.2 Microfluidic devices for yeast replicative aging . . . 6
2.2.1 Design constraints for a yeast aging microfluidic device . . 8
2.2.2 Physical mechanisms for loading and trapping mother cells . 9
2.2.3 Microfluidic design layouts . . . 10
2.2.4 Unique device features . . . 13
2.3 Design and development of the 'microchannels' yeast aging device . 14
2.3.1 A microfluidic platform for monitoring single yeast cells over several cell divisions . . . 14
2.3.2 Trap design and optimization to allow for bidirectional budding of mother cells . . . 16
2.3.3 Design layout and validation of the first generation yeast aging microfluidic devices . . . 18
2.3.4 A second generation yeast aging microfluidic device . . . 20
2.4 Methods . . . 20

2.4.1 Design and fabrication of the the YMC microlfuidic device . 20
2.4.2 Design and fabrication of the microfluidic device for yeast aging studies 21
2.5 Acknowledgements 22

Chapter 3 Single-cell analysis of metabolic cycling during growth and division in yeast using microfluidics 29
3.1 Introduction 29
3.1.1 The yeast metabolic cycle (YMC) 30
3.2 Results 32
3.2.1 Tracking metabolic cycles in single-cells via endogenous flavin fluorescence 32
3.2.2 Metabolic cycles are synchronized with the cell division cycle across different nutrient conditions 35
3.2.3 Rapamycin perturbs the phase synchronization of the metabolic cycle and CDC 37
3.2.4 Metabolic cycling continues in respiratory deficient mutants 38
3.3 Discussion 40
3.4 Methods 41
3.4.1 Yeast strains and growth conditions 41
3.4.2 Microfluidics and time-lapse microscopy 43
3.4.3 Cell tracking and data analysis 44
3.5 Acknowledgements 58

Chapter 4 Single-cell analysis of chromatin silencing dynamics at the rDNA locus during replicative aging in yeast 59
4.1 Introduction 59
4.2 Tracking rDNA silencing dynamics in the yeast aging microfluidic device 60
4.3 Quantitative analysis of rDNA silencing dynamics 63
4.4 A phenomenological model of rDNA silencing loss and cell aging . 64
4.5 Perturbations of rDNA silencing dynamics 65
4.6 Discussion 67
4.7 Materials and Methods 68
4.7.1 Strains and plasmids construction 68
4.7.2 Setting up a microfluidics experiment 70
4.7.3 Time-lapse microscopy 72
4.7.4 Quantification of single-cell traces 72
4.7.5 Correlation analysis of single-cell data 74
4.7.6 Development of the phenomenological model of cell aging . 75
4.8 Acknowledgements 86

Chapter 5 A high-throughput microfluidic platform for monitoring gene expression dynamics in yeast 87
5.1 Introduction 87
5.1.1 The 'Dynomics' platform 88
5.1.2 The yeast diauxic shift 89
5.2 Results 90
5.2.1 Design and validation of a high-throughput microfluidic platform for *S. cerevisiae* 90
5.2.2 Quantitative real-time observation of the yeast diauxic shift using the Dynomics platform 94
5.3 Discussion 97
5.4 Methods 98
5.5 Acknowledgements 100

Chapter 6 Summary 106

Bibliography 108

LIST OF FIGURES

Figure 2.1: Microfluidic devices for single-cell replicative aging in yeast. 12
Figure 2.2: A microfluidic platform for monitoring single yeast cells over several cell divisions. 15
Figure 2.3: Bidirectional budding removes cells from the trap of the YMC chip. 16
Figure 2.4: Testing of different 'dent' styles for the traps of the yeast aging microfluidic device. 17
Figure 2.5: First generation yeast aging microfluidic device. 19
Figure 2.6: Validation of the yeast aging microfluidic device. 25
Figure 2.7: The 4-strain redesign of the first generation yeast aging microfluidic device. 26
Figure 2.8: Lifespan validation of the 4-unit yeast aging chip. 27
Figure 2.9: Flexible cell traps for a second generation of yeast aging microfluidic devices. 28

Figure 3.1: Flavin oscillations in single yeast cells visualized using a novel microfluidic device and time-lapse fluorescence microscopy 33
Figure 3.2: Tracking the dynamics of flavin fluorescence relative to the cell division cycle using fluorescently tagged CDC proteins. 34
Figure 3.3: YMC-CDC phase synchronization. (a) Summary of quantitative single-cell data obtained. (b) Metabolic cycles per CDC. (c) Summary of YMC and CDC times. (d) CDC relation to trough of YMC. (e) Lag time distributions. 48
Figure 3.4: Effect of rapamycin on YMC. (a) YMC in rapamycin treated cells. (b-e) Properties of YMC-CDC relationship in rapamycin treated cells. (f) YMC period regularity with and without rapamycin 49
Figure 3.5: Metabolic cycles continue in respiratory deficient mutants 50
Figure 3.6: Dynamic range of flavin fluorescence. 51
Figure 3.7: Trajectories of flavin fluorescence and Whi5-mCherry reporter. 52
Figure 3.8: Metabolic cycles in 1X and 0.25X YNB concentrations. 53
Figure 3.9: Metabolic cycles in 0.05X YNB and 1X YNB with 10mM urea as the nitrogen source. 54
Figure 3.10: Autocorrelation analysis of metabolic cycles. 55
Figure 3.11: Metabolic cycles in 1X YNB with 150nM rapamycin. 56
Figure 3.12: Metabolic cycles in the *atp5*Δ and *cyt1*Δ mutants. 57

Figure 4.1: Tracking the dynamics of chromatin silencing in single aging cells using a microfluidic device. 61
Figure 4.2: Dynamic patterns of silencing loss during aging. 78
Figure 4.3: Validation of the silencing reporter dynamics during aging. 79
Figure 4.4: A quantitative analysis of silencing loss dynamics in single cells. 80
Figure 4.5: A phenomenological model of cell aging. 81
Figure 4.6: Perturbations of silencing dynamics shorten life span. 82
Figure 4.7: Additional quantification of silencing loss dynamics in single cells. 83
Figure 4.8: Dynamics of silencing loss in *sgf73*Δ. 84

Figure 4.9: A constant treatment of 0.5 mM NA shortens the lifespan. 84
Figure 4.10: The effects of NAM and NA treatments on lifespan are mediated through Sir2. 85

Figure 5.1: A high-throughput microfluidic platform for gene expression dynamics in budding yeast 91
Figure 5.2: Loading of HD biopixels from the spotting region. 92
Figure 5.3: Performance of HD biopixels across the microfluidic device. 93
Figure 5.4: Growth, glucose and ethanol levels of a liquid culture undergoing the diauxic shift. 94
Figure 5.5: Heat map of gene expression dynamics during the diauxic shift. 95
Figure 5.6: Analysis of gene expression dynamics during the diauxic shift through hierarchical agglomerative clustering and gene ontology (GO) enrichment. . . 101
Figure 5.7: Expression patterns of enzymatic isoforms during the diauxic shift. 102

LIST OF TABLES

Table 3.1: YMC parent strain, strains constructed and strains used in experiments . . . 42
Table 3.2: YMC Parameters for metabolic cycle peak detection 45
Table 3.3: Metabolic cycle and cell division cycle times for all experiments 47

Table 4.1: Strains used or constructed in this study. 69
Table 4.2: Plasmids constructed in this study. 70

Table 5.1: Photolithography fabrication parameters for the yeast Dynomics device. . . 99
Table 5.2: Gene ontology terms associated with genes significantly upregulated during the diauxic shift from clusters 1 and 2 from Figure 5.5, $P < 0.05$. 103
Table 5.3: Gene ontology terms associated with genes significantly down-regulated during the diauxic shift from clusters 3 and 4 from Figure 5.5, $P < 0.05$. 104
Table 5.4: Gene ontology terms associated with genes from cluster 5 from Figure 5.5, $P < 0.05$. 105

ACKNOWLEDGEMENTS

There are so many people that I would like to thank who have supported and encouraged me over the last six years. First off, I would like to thank my family for their unconditional love, guidance and support not just throughout graduate school but also in every moment leading up to it. I had the best parents anyone could ask for and the only reason I got to where I am today is because of them. Mom and Dad, thanks for always believing in me and telling me I could do it, no matter what. Your love an encouragement pushed me through so many late nights and low moments to get to where I am today. Thank you to my absolutely amazing girlfriend Jenna Summerfield. Graduate school was so much easier when I got to come home and spend time with you. You were always there to listen to me, root for me, cook for me when I didn't have the time, calm my mind when I was down, and go have fun with me whenever we could. Thank you to all of the Hasty Bunch! Omar, Nick, Spencer, Garrett, Greg and Lizzy, it was amazing getting to know you all and becoming close friends. Thanks for all the great memories, all the adventures in Downtown, PB, Staycation, Mexico and more. Thanks for the organized lunches, from Krish to Poke to trying to find a new table when the one outside our lab was occupied.

Thank you to Yang Li and Meng Jin. Collaborating and learning from you both helped make me such a better scientist. Thank you to Dr. Xuekun Lu at nano3 for all the photolithography conversations. Thank you to Lev Tsimring for conversations on the yeast metabolic cycle. Thank you to Lorraine Pillus for advice about postdocs and for being such a great geneticist, I learned so from your insights at our Yeast Aging Meetings. Thank you to Nan Hao, who put me on an excellent research path and got me started on yeast aging research. Thanks for all the great science-based discussions and for always being available to chat. And last but not least, thank you so much to my advisor Jeff Hasty. Its been an honor to be part of your lab. Thank you for giving me the space to explore my own ideas and for always pushing me in the right directions. Thank you for all the insights about research philosophy and being a productive scientist. I'll undoubtedly take all those lessons with me moving forward.

—Ricky O'Laughlin

Chapter 2 contains material that was originally published from the following papers.

· Baumgartner, B.L.*, O'Laughlin, R.*, Jin, M.*, Tsimring, L.S., Hao, N. and Hasty, J., 2018. Flavin-based metabolic cycles are integral features of growth and division in single yeast cells. *Scientific Reports*, 8(1), pp.1-10. (*equal contribution). Reproduction of this work was granted by Springer Nature under the Creative Commons Attribution 4.0 International License (https://creativecommons.org/licenses/by/4.0/). The dissertation author, Richard O'Laughlin, was a primary investigator and author of this work.

· Li, Y.*, Jin, M.*, O'Laughlin, R.*, Bittihn, P., Tsimring, L.S., Pillus, L., Hasty, J. and Hao, N., 2017. Multigenerational silencing dynamics control cell aging. Proceedings of the National Academy of Sciences, 114(42), pp.11253-11258.(*equal contribution). The dissertation author, Richard O'Laughlin, was a primary investigator and author of this work.

· O'Laughlin, R., Jin, M., Li, Y., Pillus, L., Tsimring, L.S., Hasty, J. and Hao, N., 2019. Advances in quantitative biology methods for studying replicative aging in Saccharomyces cerevisiae. Translational Medicine of Aging. (in press). Permission was granted by Elsevier to reprint material from this article in this thesis. The dissertation author, Richard O'Laughlin, was a primary investigator and author of this work.

Chapter 2 also contains work that has been submitted for publication as:

· Li, Y., Jiang, Y., Paxman, J., O'Laughlin, R., Klepin, S., Zhu Y., Pillus, L., Tsimring, L.S., Hasty, J. and Hao, N. A programmable fate decision landscape underlies single-cell aging in yeast. The dissertation author, Richard O'Laughlin, was a primary investigator and author of this work.

This work was initially placed on the bioRxiv preprint server as:

· Li, Y., Jiang, Y., Paxman, J., O'Laughlin, R., Pillus, L., Tsimring, L.S., Hasty, J. and Hao, N., 2019. An epigenetic landscape governs early fate decision in cellular aging. bioRxiv, p.630921. The dissertation author, Richard O'Laughlin, was a primary investigator and author of this work.

Chapter 2 also contains the following material that is currently being prepared for submission for publication.

· O'Laughlin, R, Li, Y., Pillus, L., Tsimring, L.S., Hasty, J. and Hao, N. "A high-throughput and adaptive microfluidic platform for monitoring yeast replicative aging." (in prep)(title tentative). The dissertation author, Richard O'Laughlin, was a primary investigator and author of this work.

Chapter 3 contains material that was originally published as Baumgartner, B.L.*, O'Laughlin, R.*, Jin, M.*, Tsimring, L.S., Hao, N. and Hasty, J., 2018. Flavin-based metabolic cycles are integral features of growth and division in single yeast cells. *Scientific Reports*, 8(1), pp.1-10. (*equal contribution). Reproduction of this work was granted by Springer Nature under the Creative Commons Attribution 4.0 International License (https://creativecommons.org/licenses/by/4.0/). The dissertation author, Richard O'Laughlin, was a primary investigator and author of this work.

Chapter 4 contains material that was originally published as Li, Y.*, Jin, M.*, O'Laughlin, R.*, Bittihn, P., Tsimring, L.S., Pillus, L., Hasty, J. and Hao, N., 2017. Multigenerational silencing dynamics control cell aging. Proceedings of the National Academy of Sciences, 114(42), pp.11253-11258.(*equal contribution). The dissertation author, Richard O'Laughlin, was a primary investigator and author of this work.

Chapter 5 contains material that will be incorporated into a manuscript for eventual submission and publication. The following individuals were involved in the work described in this chapter which will be utilized for submission: O'Laughlin, R.*, Stasiowski, L.*, Thouvenin,

G.* and Hasty, J. (*equal contribution). ”A genome-scale microfluidic platform for monitoring gene expression dynamics in yeast.” (title tentative). The dissertation author, Richard O’Laughlin, was a primary investigator and author of this work.

VITA

2008-2012	B. S. in Biomedical Engineering *summa cum laude*, The College of New Jersey
2013-2020	Ph. D. in Bioengineering, with a specialization in Quantitative Biology, University of California, San Diego

PUBLICATIONS

6. Richard O'Laughlin, Meng Jin, Yang Li, Lorraine Pillus, Lev S. Tsimring, Jeff Hasty, Nan Hao. "Advances in quantitative biology methods for studying replicative aging in *Saccharomyces cerevisiae*." *Translational Medicine of Aging* (*in press*)
5. Yang Li, Yanfei Jiang, Julie Paxman, Richard O'Laughlin, Lorraine Pillus, Lev S. Tsimring, Jeff Hasty, and Nan Hao. "An epigenetic landscape governs early fate decision in cellular aging." bioRxiv (2019): 630921. *in revision*
4. Meng Jin, Yang Li, Richard O'Laughlin, Philip Bittihn, Lev S. Tsimring, Lorraine Pillus, Jeff Hasty, and Nan Hao. "Divergent Aging of Isogenic Yeast Cells Revealed through Single-Cell Phenotypic Dynamics." *Cell Systems* 8, no. 3 (2019): 242-253.
3. Bridget L. Baumgartner*, Richard O'Laughlin*, Meng Jin*, Lev S. Tsimring, Nan Hao, and Jeff Hasty. "Flavin-based metabolic cycles are integral features of growth and division in single yeast cells." *Scientific Reports* 8, no. 1 (2018): 18045.
2. Yang Li*, Meng Jin*, Richard O'Laughlin*, Philip Bittihn, Lev S. Tsimring, Lorraine Pillus, Jeff Hasty, and Nan Hao. "Multigenerational silencing dynamics control cell aging." *PNAS* 114, no. 42 (2017): 11253-11258.
1. Richard O'Laughlin, Kevin Abbruzzese, Daniel Lee, D. Gordon Allan, and Manish Paliwal. "Failure analysis of surrogate tibial constructs with medium and fast setting bone cements." *Engineering Failure Analysis* 32 (2013): 312-321.

(*equal contribution)

ABSTRACT OF THE DISSERTATION

Microfluidic technologies for investigating dynamics-based regulation in *S. cerevisiae*

by

Richard O'Laughlin

Doctor of Philosophy in Bioengineering (with a specialization in Quantitative Biology)

University of California San Diego, 2020

Professor Jeff Hasty, Chair

Technological advances in molecular biology over the last several decades have enabled researchers to probe the inner workings of living systems at unprecedented scale and resolution. These new capabilities have resulted in the emergence of the field of quantitative biology, which seeks to utilize mathematical modeling along with techniques from systems biology and synthetic biology in order to ascertain the design principles that underlie the structure and function of biological regulatory networks. In pursuit of this goal, it has become clear that heterogeneity at the single-cell level and the dynamics, or time-dependent behavior, of these networks are critical features of a multitude of biological processes. Much of the foundational work establishing the importance of these themes began from the study of microbes such as the budding yeast *Saccha-*

romyces cerevisiae. However, even in unicellular organisms such as *S. cerevisiae*, significant challenges remain in tracking and analyzing single cells over long periods of time, as well as monitoring gene expression dynamics at scale. Development of these capabilities is critical, not only for understanding the cell biology of *S. cerevisiae*, but also for being able to apply the mechanistic insights obtained from yeast to evolutionarily conserved pathways in higher eukaryotes. In this thesis, I describe the design and application of microfluidic technologies for *S. cerevisiae* that address these limitations. In Chapter 1, I detail the utility of microfluidic devices and time-lapse fluorescence microscopy for analyzing single cells and recording biological dynamics. In Chapter 2, I describe the development of novel microfluidic devices that enable long-term isolation and tracking of single yeast cells, culminating in a design that can monitor cells over the course of their entire replicative lifespans. In Chapters 3 and 4, I discuss applications of the microfluidic technologies described in Chapter 2. Chapter 3 concerns the discovery of metabolic cycles in flavin fluorescence at the single-cell level, which can oscillate along with and independently of the cell division cycle, persisting even when cellular respiration is blocked. Chapter 4 describes the uncovering of two divergent paths taken by single yeast cells during replicative aging, in which distinct dynamics of heterochromatin silencing at the rDNA region that modulate cellular lifespan can be detected in each group. In Chapter 5, I apply the design principles validated in the construction of microfluidic devices for tracking single cells in order to develop a high-throughput microfluidic platform for recording gene expression dynamics of thousands of yeast strains simultaneously. I demonstrate a proof-of-principle of this technology by monitoring changes in gene expression across more than 4000 yeast strains in real-time during the diauxic shift. The microfluidic devices developed and described herein underscore the importance of single-cell analysis and dynamics-based regulation by elucidating novel sources of heterogeneity at the single-cell level and demonstrating how metabolic, chromatin silencing and gene expression dynamics contribute to the regulation of complex processes such as cell division, replicative aging and growth in changing environments. Further, these technologies establish a foundation

upon which future studies can continue to pursue quantitative biology work in yeast, from the single-cell level to the genome scale.

Chapter 1

Introduction

1.1 Quantitative Biology: searching for the design principles of biological systems

Modern molecular biology has become an increasingly quantitative discipline thanks to a bevy of new technologies that have been introduced to the field. While no means an exhaustive lists, these technologies include advancements in molecular cloning, DNA sequencing , DNA synthesis, microfluidics, imaging and fluorescent molecular reporter systems such as green fluorescent protein (GFP). By leveraging the early work of many pioneering biologists who have characterized and discovered a plethora of individual features, genes, molecules, and pathways inside cells, technologies such as these have enabled scientists to study these biological components in fundamentally new ways. Systems and synthetic biology are two fields that emerged from these new capabilities.

Both systems and synthetic biology are relatively new disciplines that encompass many subfields, and exact definitions of what they entail may vary [1, 2]. For example, the field of systems biology includes the mathematical modeling of small genetic regulatory networks that contain a handful of core components [3], the computational modeling of metabolic fluxes through

biochemical cellular reactions on the genome-scale [4, 5], and even the holistic modeling of entire cells [6, 7]. Likewise, the field of synthetic biology can include the *de novo* design, construction and mathematical analysis of simple gene circuits such as toggle switches [8], oscillators [9–11], and logic gates [12, 13], as well as the metabolic engineering of organisms to produce medically relevant compounds compounds [14, 15], genome editing with CRISPR-Cas9 [16–18] and the synthesis and construction of entirely synthetic genomes and chromosomes [19, 20]. Although these various research areas have different goals and focus areas, one unifying theme amongst many of these topics is the utilization of quantitative analysis techniques, mathematical modeling and computational approaches in order to gain insight into their data. Quantitative biology is the field that focuses on utilizing these approaches in order to understand the design principles of the biological networks that give rise to cellular functions, or in other words, why the regulatory networks inside cells appear the way they are and what advantages do particular network configurations have [3, 21].

1.2 Microfluidics and time-lapse fluorescence microscopy for quantitative biology

Two technologies that have proved very useful for systems and synthetic biology studies have been microfluidic devices and time-lapse fluorescence microscopy [22]. Microfluidic devices offer a well controlled environment where cells receive a constant supply of nutrients. The optically clear and soft plastic polydimethylsiloxane often used for constructing microfluidic devices [23], allows for time-lapse fluorescence microscopy to be performed on cells growing in the device. Thus, various cellular process can be monitored during experiments, including the expression of different genes, cell division, and cell morphology just to name few. Two important themes that have emerged from studies that have combined these two technologies has been the importance of single-cell analysis and dynamics-based regulation.

1.2.1 Dynamics-based regulation in biology at the single-cell level

Dynamic phenotypes are pervasive throughout biology and govern many important biological processes such as cellular differentiation [24, 25], stress response [26, 27] and epigenetic regulation [28]. By utilizing microfluidic technologies or time-lapse fluorescence microscopy or both to analyze single cells, a number of examples across different kingdoms of life have been discovered. For example, in the bacterium *Bacillus subtilis*, entry into a state that allows cells to uptake DNA from the environment, termed competence, depends on the dynamics of a gene regulatory network involving two genes, ComK and ComG [24]. Similarly in yeast, the transcription factors Msn2 and Msn4 respond to different cellular stressors with distinct patterns of nuclear localization [26, 27]. Depending on the dynamics of these transcription factors, this can result in different forms of genetic regulatory logic on the downstream genes they control, being able to act as together as AND or OR gate in different situations [26, 27]. Likewise in mammalian cells, modulating the length of time that certain chromatin regulators are recruited to genetic loci can result in different patterns of silencing dynamics at that region [28].

Often, studies such as those mentioned above are conducted at the single-cell level. At this resolution, phenotypic differences between individual cells that could potentially be obscured by bulk measurements can be made apparent. This idea was crystallized when Elowitz et al. [29] described how two identical promoters in single bacteria cells can give rise to a range of gene expression levels of a fluorescent reporter both within and between individual cells. Since then, a multitude of different studies have described how individual isogenic cells can differ from one another in surprising ways and how this phenotypic heterogeniety at the single-cell level plays an important role in a variety of processes [30–32].

1.3 Thesis overview

As detailed above, single-cell analysis and dynamics-based regulation are two growing areas of quantitative biology research that are greatly expanding our understanding of a variety of biomolecular processes. During my time in graduate school, I worked to further these lines of inquiry by combining novel microfluidic technologies with time-lapse fluorescence microscopy to study replicative aging and metabolic oscillations in budding yeast; two areas where single-cell analysis and dynamics-based regulation have not been extensively explored in the literature. Chapter 2 of this thesis details the design and development of the microfluidic devices I have designed to accomplish these tasks. Chapter 3 and Chapter 4 document the results from single-cell studies on metabolic oscillations during the cell division cycle and chromatin silencing dynamics during replicative aging, respectively. In Chapter 5, I describe the development of a high-throughput microfluidic platform for monitoring gene expression dynamics in thousands of yeast strains simultaneously, and demonstrate its utility by monitoring, in real-time, a yeast culture undergoing the diauxic shift. The work described herein not only showcases the powerful insights that can be gained from analyzing single-cells and investigating the dynamics of biological regulation, but also lays the groundwork for future studies to apply these microfluidic technologies and biological insights to continue explore and uncover the regulatory nature of a variety of biological processes.

Chapter 2

Microfluidic technologies for single-cell analysis of yeast

2.1 Introduction

In this Chapter, I detail the design, construction and validation of microfluidic devices that are able to trap, isolate and track single haploid yeast cells. The main motivation for this is to be able to conduct time-lapse fluorescence microscopy experiments during replicative aging in single yeast cells. To acheive this goal, I began by designing a microfluidic platform that could track cells over several cell divisions, which was an improvement over then currently available yeast microfluidic devices designed by the Hasty Lab. I eventually modified this device to be suitable for replicative aging studies. We begin this Chapter by covering the study of yeast replicative aging in microfluidic devices. I describe the utility of yeast a model organism for aging research and then introduce the published microfluidic devices for studying replicative aging. After covering the 'microchannel' design that I developed, I describe this device, as well as the process of developing it, in greater detail. Applications of these microfluidic devices to scientific problems are described in Chapters 3 and 4.

2.2 Microfluidic devices for yeast replicative aging

Rapid technological advances over the past several decades have enabled an increasingly quantitative understanding of biological systems. Cutting-edge imaging [33], sequencing [34, 35], microfluidics [36] and genome editing [37, 38] methods are generating increasingly complex data sets that, when combined with the requisite quantitative analysis, are producing groundbreaking biological insights. One such area benefitting from these new developments is the field of geroscience, which seeks to understand the basic biological mechanisms of aging and apply this knowledge to treat human diseases and prolong healthy lifespan [39, 40]. While progress is being made by applying new experimental techniques to directly study aging in humans [41, 42], conducting aging experiments in humans is difficult and in certain cases impossible. However, work from a variety of model eukaryotic organisms has revealed a number of evolutionarily conserved molecular processes that drive aging [43, 44], which helps to point the way for future work in and therapies for humans. In particular, the use of the budding yeast Saccharomyces cerevisiae as a genetically tractable single-celled model system for studying aging has helped illuminate a number of important conserved pathways underlying aging [43–48] as well as potential interventions for mitigating its effects [49].

Aging in S. cerevisiae is primarily studied in two modalities, chronological aging and replicative aging [50]. For chronological aging, cells are held in stationary phase, then periodically tested for their capacity to resume division when the stationary-inducing conditions are relieved. The time in which the cells can successfully survive in stationary is defined as their chronological lifespan (CLS) [50]. In contrast, replicative aging is defined by the number of daughter cells that can be produced by a single mother cell before it stops reproducing and dies, termed as replicative lifespan (RLS) [50, 51]. Because replicative aging occurs on a timescale of days rather than weeks, it has the potential of seamlessly interfacing with microfluidic devices and time-lapse fluorescence microscopy, widely used tools for studying dynamic biological processes

in real-time [22, 52]. However, until the last seven years, the field of yeast replicative aging relied on microdissection [51, 53] as the only tool for RLS measurements. For this method, an experimenter uses a micromanipulator to separate mother and daughter cells growing on an agar pad under a microscope, thereby keeping track of and recording the number of divisions of each mother cell for RLS analysis [53]. Although microdissection has provided valuable knowledge about lifespans under various genetic and environmental conditions, its manual nature results in a number of drawbacks, including its tedium and the inability to dynamically modify the growth environment. An additional significant drawback of this technique is that the thick agar pad on which the cells grow prevents high-quality time-lapse fluorescence microscopy from being conducted [54, 55]. Consequently, dynamic and quantitative single-cell measurements cannot be performed, which greatly impedes understanding of the genetic regulatory networks governing the cell aging process, which are dynamic by their very nature. To circumvent these shortcomings, new technologies and methods have been developed in recent years that offer alternatives to the microdissection approach.

Here we review the recent advances in studying yeast replicative aging using microfluidics, time-lapse fluorescent microscopy, computational modeling and high-throughput technologies. We cover recent studies utilizing each technique and discuss the unique insights provided by these approaches compared to traditional methods. Taken together, these advances provide novel insights and challenges for the field of yeast aging and suggest important and creative new avenues for applying this research to higher organisms. We conclude by discussing open questions and new directions raised by these approaches in this field that is ripe for new findings.

To address the drawbacks of the traditional microdissection method, various polydimethylsiloxane (PDMS) based microfluidic devices have been developed. These devices automate mother-daughter separation during aging and allow RLS measurements to be interfaced with time-lapse fluorescence microscopy. These technologies have provided an unparalleled look at the aging process in single yeast cells by allowing the dynamics of various molecular and cellular

processes to be tracked and quantified. The construction and design of such devices, however, is challenging, and microfluidic platforms capable of tracking large numbers of single mother cells throughout their lifespans require new features not necessary in the design of devices for more short-term cell tracking [23, 56–59]. In this section, we discuss the design strategies that enable microfluidics to be applied to yeast replicative aging.

2.2.1 Design constraints for a yeast aging microfluidic device

One of the first considerations to have in designing microfluidics for yeast aging is the operation time of the device. An often noted feature of replicative aging is the wide distribution of lifespans one obtains from a population [51, 60], with reported RLS values for long-lived wild-type (WT) cells from microdissection studies [51, 53] exceeding 40 divisions. As the population doubling time for yeast is about 90 minutes [61], 40 divisions for single cells equates to approximately two and a half days. Considering that certain long-lived mutants can divide 60 or more times [62], it is clear that a successful microfluidic device must be able to trap mother cells for more than 4 days. Indeed, these long operation times for RLS studies result in another problem: the accumulation of a large number of daughter cells in the device. If not rapidly removed, the cells can dislodge mother cells, interfere with automated cell tracking or clog the device. Finally, the mechanisms used to trap mother cells must not stress the cells and RLS measurements should be comparable to microdissection studies. Taking these issues into account, a number of yeast aging microfluidic devices have been successfully designed (Fig. 1A), with lifespan measurements being validated in WT cells and various longevity mutants [54, 55, 63–69]. While each device design has its own unique features that allow it to fulfill the aforementioned criteria, the currently available microfluidic devices employ some common strategies to load and trap mother cells. Before detailing the particularities of each yeast aging microfluidic device, we describe these shared mechanisms in order to properly contextualize the motivations behind each design.

2.2.2 Physical mechanisms for loading and trapping mother cells

There are a plethora of methods for trapping single cells in microfluidic chambers. However, for replicative aging applications, the asymmetric nature of yeast division [70], wherein for most of their lifespans, mother cells give rise to daughters that are smaller than themselves [71], favors three primary strategies for loading cells into the trapping regions and retaining mother cells throughout their entire lifespans, as well as removing daughter cells: contact-based mechanical trapping, geometric confinement and hydrodynamic trapping. Contact-based mechanical trapping entails immobilization of cells from above, that is, between the PDMS ceiling of the microfluidic device and the glass slide. Using this approach, trapping regions smaller than or approximately the same size as a typical yeast diameter are used to push down on cells and hold them in place. Loading cells requires the ceilings or heights of these traps be raised, so that cells can actually get into the trapping regions. This is done by increasing the pressure at both the inlet and outlet of the device to generate hydrostatic pressure that raises the height of the ceiling, allowing cells to pass under the trapping areas [54, 63] (Fig. 1B, left). Release of the pressure by allowing flow toward the waste port lowers the ceiling back down, immobilizing cells and trapping them [54, 63] (Fig. 1B, right). Since daughter cells are smaller than their mothers, they are not as restrained by the low ceilings and can more easily escape from the trap and flow toward the waste port.

As an alternative to contact-based mechanical trapping, most recently published microfluidic devices utilize a physical mechanism known as hydrodynamic trapping. In the context of this review, hydrodynamic trapping can be defined as a technique for capturing and immobilizing cells against structures in a microfluidic device by exploiting the hydraulic forces that act on particles in a fluid [72–77]. Hydrodynamic trapping enables a number of desirable features for yeast aging microfluidic devices such as trapping areas with ceilings taller than the diameter of a typical yeast cell (i.e. < 4 μm). For devices of this kind, microstructures are positioned along the flow path to capture and immobilize cells. Because loading of cell traps increases the fluidic resistance along that path, this increases the flow through adjacent empty traps, which

facilitates cell loading. From this point, mother cells can be obtained from daughters that enter isolated trapping regions that geometrically confines their movement (Fig. 1C) or directly from the immobilized cells that are trapped (Fig. 1D). With the physical principles used by different microfluidic devices for loading and trapping mother cells during their entire lifespans in hand, we now turn to a discussion of the design layouts of various devices.

2.2.3 Microfluidic design layouts

Three of the earliest published microfluidic devices for yeast aging relied on contact-based mechanical trapping of mother cells. This was accomplished via vertical micropads [54, 63] or dead-end microcavities [64] (Fig. 1A, top row). The device reported by Zhang et al. [63] was an improvement on an original device developed by this group that used chemical modification of the glass coverslip and cell wall as part of its trapping mechanism [55]. The use of vertical micropads to trap cells allowed them to jettison this requirement. In the designs by Lee et al. [54] and Zhang et al. [63], the vertical micropads traps are positioned within an "open room" that is much taller than the height of the traps (for example, 15 μm in the device by Lee et al. [54]) in which media flows. The cross-sectional area of these traps is large enough to accommodate multiple mother cells under a single micropad. For the design by Fehrmann et al. [64], media channels 40 μm tall flank 3.3 μm trapping areas with dead-end cavities. Here, cells grow to fill the trapping area until a newborn cell reaches the end of the cavity where it is subsequently tracked as a mother cell for RLS analysis. While lifespan measurements of these devices produced similar results to those obtained with microdissection, the trapping methods for these devices are relatively inefficient. For designs relying on contact-based mechanical trapping, it can be difficult to retain mother cells over their entire RLS. It is also difficult to control the number of cells trapped in the case of the vertical micropad designs [54, 63], or the timing at which cells reach the end of the cavities [64] . For example, in the micropad designs [54, 63] larger daughter cells or cells washing down from upstream can be caught under a single micropad and dislodge mother cells from the trapping

regions. Similarly, the dead-end microcavities design [64] relies on mother cells budding in a single direction for the entire course of their lifespan and a single polarity switch can remove the mother from the trap. Further, the contact-based mechanical trapping employed by these devices may not be suitable for various longevity mutants that could have altered cell size compared to wild-type cells.

With devices from Lee et al. [54], Zhang et al. [63] and Fehrmann et al. [64] paving the way for applications of microfluidics to yeast replicative aging, a new generation of devices was developed that built upon and extended these foundational technologies. As previously mentioned, these devices use hydrodynamic trapping and/or geometric confinement for loading and retaining mother cells in the traps throughout their entire lifespans. An example of a device that uses both hydrodynamic trapping and geometric confinement for operation is the three-bar "jail" design [56] that was optimized to trap single cells for replicative aging experiments by Liu et al. [67] (Fig. 1A, middle right). In this device, cells are guided toward the openings between two of the bars by the fluid flow, eventually producing a bud that enters the jail. Once there it is tracked as the mother cell. The 5.3 μm tall PDMS bars spanning the entire space between the ceiling of the device and the glass slide spatially confine each mother cell while also allowing for increases in cell size that accompany aging [78]. Buds can be produced out of three openings in the jail small enough for daughters to pass through and periodic pulses of high velocity flow are used to aid in daughter cell removal. A variation of this design was created to analyze aging in diploid cells, where a two-bar jail structure was created which functions using the same basic principles as the three-bar jail [69].

Another set of devices more fully rely on hydrodynamic trapping for proper device operation. Here, traps consist of arrays of cup shaped two-bar traps [65, 66] or open-ended microchannels [68]. Devices developed by Crane et al. [65] and Jo et al. [66] are single layer devices where traps are positioned parallel to the direction of flow in an open room layout similar to devices using vertical micropads [54,63]. The device developed by Li et al. [68] consists of two

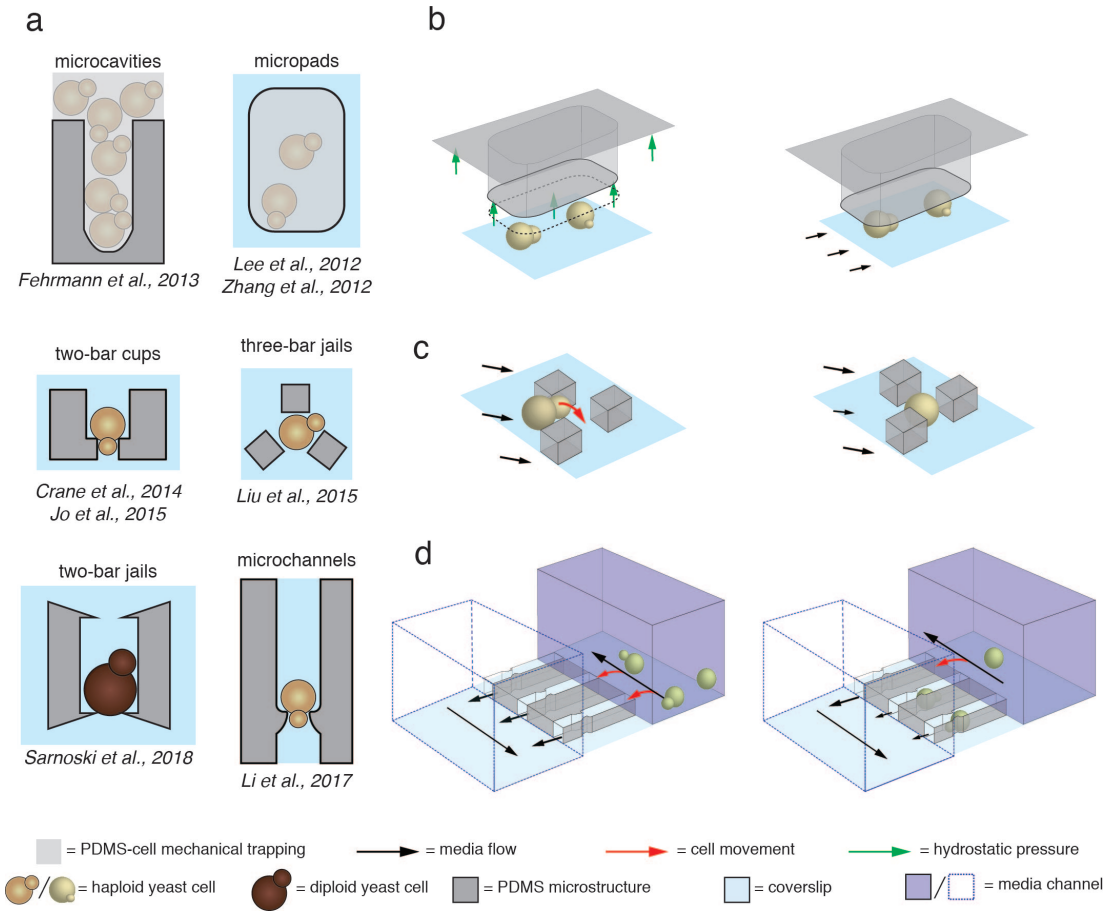

Figure 2.1: Microfluidic devices for single-cell replicative aging in yeast.(a) The cell trap designs for currently published yeast aging microfluidic devices [54, 63–69]. (b) Example of loading in a device relying on contact-based mechanical trapping, where hydrostatic pressure is used to raise the height of the micropad traps (left). Releasing pressure by allowing fluid flow to the waste port lowers the height of the micropads once more and traps cells underneath them [54, 63]. (c) Devices that use hydrodynamic trapping to guide cells to the outside of the jails. Cells can produce a daughter cell through the openings in the jail (left). The cell that enters the jail is geometrically confined, and is analyzed as the mother cell for RLS experiments [67] . (d) Loading of microchannel traps [68] using hydrodynamic trapping. Cells are guided into the traps by the flow and can produce buds through a small opening at the bottom of the trap or toward the entrance (left). Loading of a cell into the trap increases the hydraulic resistance of this path for fluid flow, facilitating the loading of adjacent traps (right). (Figure adapted from refs. 2 [54, 63–69]).

layers, with 20 μm tall media channels positioned perpendicular to the 4.3 μm cell traps. In each design, traps feature small 3 µm openings that provide a docking site for mother cells, preventing their movement beyond this point while allowing passage of budding daughters. Furthermore,

these openings allow for constant fluid flow through the trap, which provides the hydrodynamic force needed to secure mother cells over the course of their entire RLS. With openings on each side of the trap, mothers are able to produce buds in either direction, which are eventually washed away by the media flow. The use of hydrodynamic trapping allows the ceilings of the trapping regions to be taller than the height of the cells [65, 66, 68]. Along with the wider width of these traps compared to that of the cells, these designs allow room for increases in cell size during aging. Importantly, the use of hydrodynamic trapping enables very efficient loading [66, 68] and also robust retention rates of mother cells [65, 66, 68].

2.2.4 Unique device features

Due to the different design layouts of each, there are a number of unique capabilities for the aforementioned microfluidic devices. A feature exclusive to the devices with dead-end microcavities [64] and and jail structures [67, 69] is the requirement of newborn daughter cells to load their traps. As a result, RLS analysis begins with virgin cells that have not yet divided, yielding exact lifespan measurement for all analyzed cells. Although undoubtedly useful, given that populations are disproportionally composed by young cells, with only 12.5% of cells are expected to be older than two generations [79, 80], this feature is not an absolute necessity for obtaining accurate RLS measurements for WT cells or longevity mutants. In regards to lifespan measurements of large numbers of cells (500 or more) or multiple strains in a single experiment, the device by Jo et al. [66] is particularly suited for such applications. Another feature that is unique to devices using microcavities [64], micropads [54, 63] and microchannels [68] as traps is the ability to visualize daughter cells for some time without them being immediately washed away. For example, daughter cells, especially of old mothers can be maintained under micropads for some time before removal. Similarly, for the microchannels used by Li et al. [68] daughters born toward the entrance of the microchannel can be retained for some time. Although removal of daughter cells is critical to prevent device clogging and for later image analysis and tracking

of mothers, the daughter cells are a potential valuable source of data. Monolayer open room style devices [65–67, 69] are designed to immediately remove all daughters from the field of view and therefore sacrifice the possibility of obtaining daughter cell information. In particular, the micropad design by Zhang et al. [63] and microchannel design by Li et al. [68] have been leveraged to analyze daughter cell gene expression [81] and cell morphology [68, 82]. Finally, devices by Crane et al. [65] and Li et al. [68] allow media switches to be performed in their devices. This enables dynamic modifications of the cellular environment in the form of chemical perturbations or changes to the nutrient conditions. For more technical details about the design, validation and testing of many of the microfluidic devices described here, we refer the interested reader to a recent thorough review on this topic [83].

2.3 Design and development of the 'microchannels' yeast aging device

2.3.1 A microfluidic platform for monitoring single yeast cells over several cell divisions

As discussed in section 2.2.3, the 'microchannels' yeast aging device is highly robust and optimized for the study of replicative aging. Perhaps the most critical feature of this device is that it allows cells to bud bidirectionally, either toward the entrance of the trap or toward the exit of the trap. However, before developing the specific trap design that allowed for bidirectional budding, I first developed a microfluidic chip that was geared toward monitoring single yeast cells over several cell divisions (Fig. 2.2). The main purpose of this device was to be used for studying the yeast metabolic cycle (YMC) in single cells, which will be discussed in Chapter 3. As such, I will refer to this device as the 'YMC chip' moving forward.

As mentioned previously in section 2.2, several of the currently published microfluidic

devices [23, 56–58] were not well suited to long term monitoring of large numbers of yeast cells over multiple cell divisions. In most cases [23, 57, 58], the cell trapping area was quickly filled to confluence, making it difficult to track single cells over multiple divisions and limiting throughput. The YMC chip circumvents these issues by utilizing hydrodynamic trapping to arrange cells in monolayer rectangular traps (Fig. 2.2a, b). A 1.3 μm tall conduit region fluidically connects the cells traps and media channels, allowing flow through the trap (which provides the hydrodynamic trapping effect) while also blocking cell movement past the 4.7 μm trapping region, since cells are too large to pass under the 1.3 μm tall conduits. As a result, cells are efficiently loaded into the trapping regions where cells at the bottom of the trap are immobilized at the boundary between the trap and the conduit region (Fig. 2.3a), making them much easier to monitor with automated cell tracking algorithms. However, cells can not be trapped indefinitely using this strategy.

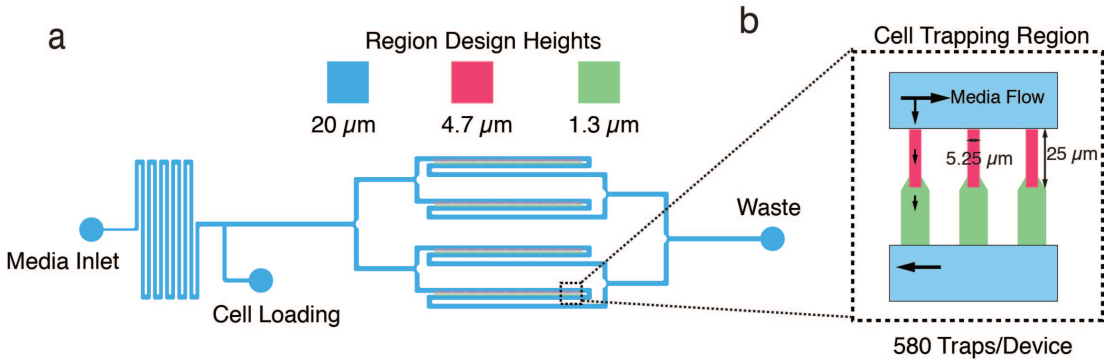

Figure 2.2: A microfluidic platform for monitoring single yeast cells over several cell divisions (a) Four parallel branches contain cell trapping regions of 4.7 μm tall (red) and media conduits (1.3 μm tall), with a total of 580 traps on the entire device. (b) This design permits the flow of media from the main channel (20 μm tall, blue) through the cell trapping region but does not allow cells to pass through the media conduits as they are too low in height. In this way cells are stably maintained at the bottom of the trap (for as long as they bud up toward the entrance of the trap) while constantly being supplied media throughout the course of the experiment. .

Cells at the bottom of the trap can only be maintained in this position as long as they bud upwards toward the entrance of the trap. Despite the asymmetric nature of yeast cell division, whereby the mother cell produces a daughter cell that is smaller than itself (until late in the mother's lifespan [71]), the daughter cells are still not small enough to pass under the 1.3 μm

conduits. Because of this, a polarity switch where the mother cell produces a bud downward toward the conduit will push the mother cell out from the bottom of the trap and eventually remove it from the trapping region completely (Fig. 2.3b). Consequently, that cell can no longer be tracked. For this device, observing a single cell for more than 10 generations is rare. Since wild-type yeast cells can produce around 20-30 daughter cells on average before death [53], it is clear that this style of trapping yeast cells is not suitable for studying replicative aging.

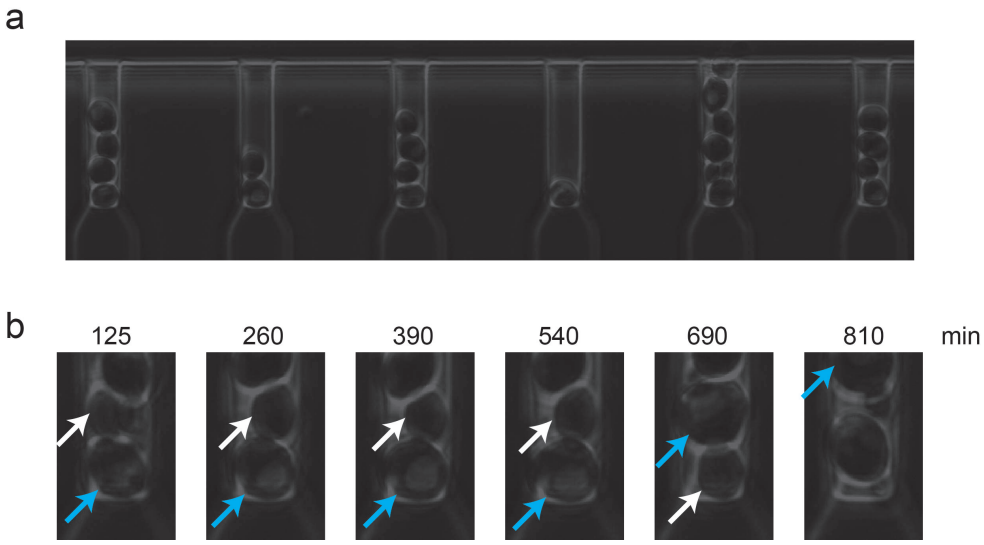

Figure 2.3: Bidirectional budding removes cells from the trap of the YMC chip. (a) Single position image with cells loaded. (b) Time-lapse of budding, showing that when budding polarity switches, cells are pushed out from the bottom of the trap where they can no longer be tracked. Blue arrows indicated tracked cells while white arrows indicate daughter cells. .

2.3.2 Trap design and optimization to allow for bidirectional budding of mother cells

While it was clear that the YMC chip could not allow replicative aging to be studied in single cells, it was also apparent that this design was not too far off from being able to do just that. If the conduit was made just tall enough so that the daughter cell could pass under it and exit the trap, while the mother cell was held in place, this could allow for full lifespan observation of

the mother. Despite its potential, through numerous design iterations, successful implementation of this strategy was not able to be attained. However, a similar strategy was also tried in addition to changing the height of the conduit. Instead of using a conduit which was smaller in height than the cell trap, a number of trap designs were tested in which a narrowing or 'dent' was designed into the cell trap itself. The idea behind this design was that, since the daughter cells are smaller than their mother for most of their lives [71], and buds produced by the mother cells initially are very small, it may be possible to design the dent such that the budding daughter cells can fit through it, while the mother cells cannot. Through numerous design iterations of this strategy, two main trap designs emerged as possible successful strategies and microfluidic devices with these trap styles were built and tested.

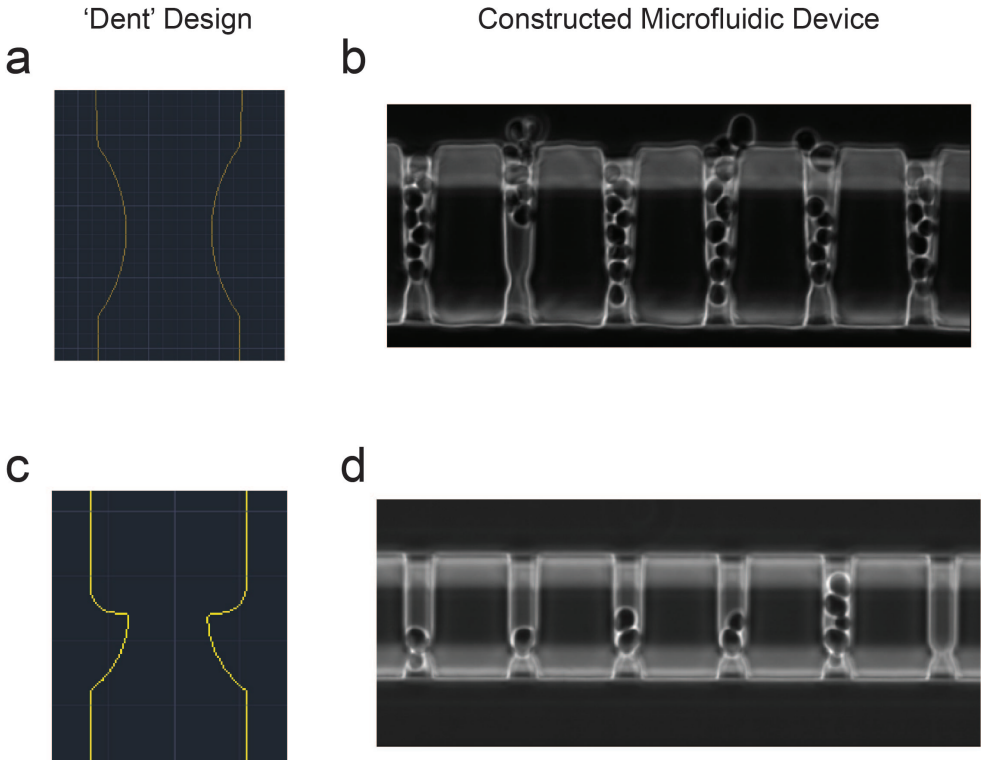

Figure 2.4: Testing of different 'dent' styles for the traps of the yeast aging microfluidic device. (a) Arch-styled 'dent' design. (b) Yeast aging microfluidic device built with arch-styled 'dent' traps. The traps also have a 'V' shape, where they are wider at the inlet of the trap. (c) Chalice-styled dent' traps. (d) Yeast aging microfluidic device built with chalice-styled 'dent' traps. .

With these two 'dent' styles for the traps, microfluidic experiments were conducted to test how well each trap style worked in retaining mother cells. Various widths of the dents for the arch-styled and chalice-styled traps were tested including 2.8, 3.0 and 3.2 μm widths. Additionally, different trap widths were tested from 5 to 6 μm. I note here that the media channel layouts were also varied for both dent styles to test the impact that this factor had on mother cell retention and lifespan. Ultimately it was determined that the trap style is a much more critical factor for retaining mother cells. Flow rate in the media channel was also very important, however since the flow rate could be adjusted by changing the height of the media syringe, media channel layout played a much more minor role than the trap style. After several rounds of testing it was determined that the chalice-styled traps with a 3.0 μm wide dent were the optimal traps, as they were able to robustly retain mother cells over the course of several days for their full replicative lifespans while also allowing daughter cells to pass through the dent and not interfere with mother cell retention. Therefore this chalice-styled styled trap was used moving forward.

2.3.3 Design layout and validation of the first generation yeast aging microfluidic devices

Having optimized the trap design to retain mother cells and allow for bidirectional budding and removal of daughter cells using the chalice-styled traps, we settled on a three inlet media channel design to create the first generation yeast aging device (Fig. 2.5). We next sought to fully test the lifespan and functionality of the device. We developed a growth protocol involving two steps for obtaining high numbers of newborn yeast cells. Yeast cells were inoculated into 2 ml of synthetic complete medium (SC, 2% dextrose) and cultured overnight at 30°C. 2 μl of saturated culture was diluted into 20 ml of fresh SC medium and grown at 30°C overnight. To evaluate the bud scar distribution of yeast cells, a cell culture with OD600 of about 1.0 was sampled and stained with 5 μg/ml WGA conjugates (Alexa Fluor 647 conjugate, Thermo Fisher) for 10 min at 37°C. Cells were washed twice with PBS after incubation then examined with a Leica TCS SP8

Stimulated Emission Depletion (STED) superresolution microscope using a Cy5.5 channel to visualize the bud scars (Fig. 2.6a). We also validated that cells were not squeezed when they were loaded into the traps (Fig. 2.6b). Further, we were able to obtain a healthy lifespan for mother cells, with the mean replicative lifespan in our device being approximately 21 to 22 generations (Fig. 2.6c). We were also able to recapitulate the lifespan extending effects of deletion of SGF73 (Fig. 2.6c). Finally, we identified fluorescence imaging settings for GFP, mCherry and iRFP that did not effect cellular lifespan, allowing us to utilize fluorescent markers to track different cellular processes during aging (Fig. 2.6d). See Chapter 4.7 for details on fluorescence imaging settings.

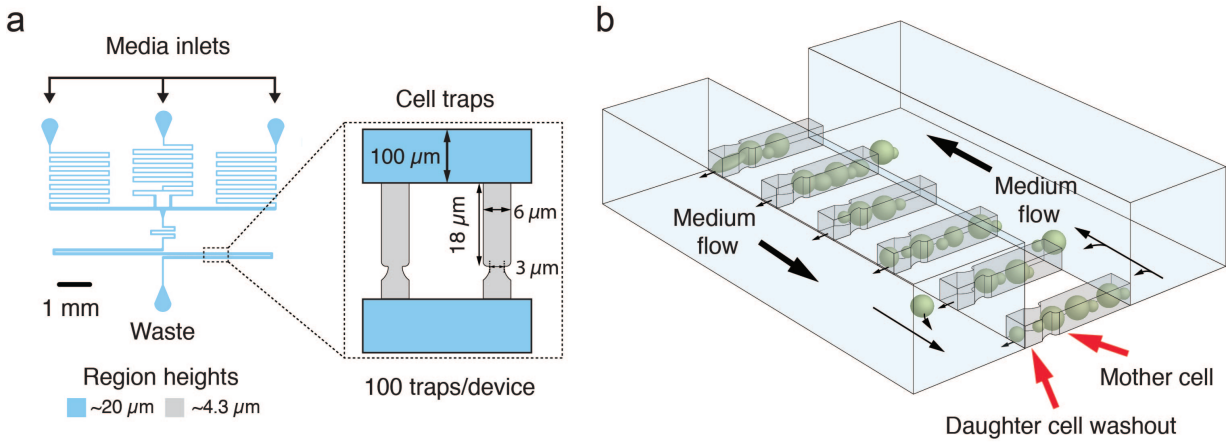

Figure 2.5: First generation yeast aging microfluidic device. (a) Device layout consisting of features of two different heights, approximately 20 μm tall media channels and 4.3 μm tall cell traps. A three inlet media channel design was used. (b) Schematic of device operation showing where mother cells are retained, bidirectional budding and hydrodynamic trapping.

In Chapter 4 of this thesis I discuss in-depth the application of this first generation yeast aging microfluidic device to the study of chromatin silencing at the rDNA region during aging. However, along with work in studying the molecular biology of yeast aging using this device, I continued to improve the microfluidic device itself. The first such improvement was simply a redesign of the media channel layout in order to reduce the number of syringes needed, increase throughput and increase the number of different strains that could be tested in a single experiment. This device is shown in Figure 2.7. Performance of this device versus the three-inlet media

channel design were essentially identical, as flow rate in the device and the trapping style using the chalice-style dent traps were kept constant. Lifespan validation for this device using various longevity mutants and lifespan extension under calorie restriction are shown in Figure 2.8. Further experiments with this device can be found in Li et al. 2019 [85].

2.3.4 A second generation yeast aging microfluidic device

The most recent yeast aging microfluidic device was designed with a fundamentally new feature that may allow for enhanced functionality and more precise measurements of aging cells, with further increased throughput over the 4-unit device Figure 2.7. The design of this device contains cell traps that are designed to be flexible, allowing cells to stretch and expand past the original size of the traps (Fig. 2.9). This was done by adding rectangular structures next to each trap. These structures are fluidically closed and only served to create a blank space that creates a thin wall between the cell trapping region of the blank space in the PDMS left by the rectangular structures. Surprisingly, this wall could be made as thin as 2 μm. Cells were able to stretch the width of these straps under various different wall thicknesses (Fig. 2.9). Currently, these traps are being implented in the design of a final second generation yeast aging microlfuidic device.

2.4 Methods

2.4.1 Design and fabrication of the the YMC microlfuidic device

The microfluidic device used in this study was designed to trap short single rows of cells in individual rectangular traps that would minimized intercellular communication and provide good resolution of single cells. To accomplish this cell traps were 25 μm by 5.25 μm and approximately 4.7 μm tall. Cell traps are open on both ends allowing media to flow through the traps and provide continuous nutrients to the cells. The device design (see Chapter 2) was drawn in AutoCAD

(Autodesk) and then printed on chrome glass masks (HTA Photomask). Standard procedures similar to those detailed by Ferry et al. [23] for photolithography with SU8 (MicroChem) were used to pattern silicon wafers (University Wafer) with an EVG620 mask aligner (EV Group) and then make PDMS (polydimethylsiloxane, Dow SYLGARD) molds of the devices.

2.4.2 Design and fabrication of the microfluidic device for yeast aging studies

In designing a microfluidic device for studying aging in budding yeast, the viability of the cells, efficiency of cell trapping and robustness of the device were our primary concerns. Multiple designs were built and tested to optimally satisfy these criteria. The robustness of the device is affected by clogging due to excess cells around the traps and at the waste port, which can interfere with mother cell lifespan and retention. Supplying media through approximately 20 [65–67]. The device was optimized for using continuous gravity-driven flow during operation, with the three-inlet design also facilitating media switching experiments. The height and width of cell traps were optimized for cell loading and retention. Cell loading efficiencies and final retentions until cell death are approximately 93% and 75% respectively. See Quantification of single-cell traces (Chapter 4.7.4) for a consideration of cell retention. We quantified the widths of cells in the culture population immediately before loading and cells that are just loaded into the device, respectively. As shown in Fig. 2.6b, the distributions of cell widths are similar for the population before loading and for the loaded population, confirming that the device loading does not select for a subpopulation of cells. A potential caveat of microfluidic devices for aging studies is that the limited size of cell traps might affect the lifespan. However, given that lifespans measured using our device are comparable to those from classical microdissection studies (Fig. 2.6c), the effect of the trap size on lifespan, if any, should be modest.

To construct the microfluidic device, designs were first drawn in AutoCAD (Autodesk Inc.). Modeling of fluid flow in the device using COMSOL Multiphysics aided in design

(COMSOL Inc.). Two chrome quartz glass masks (HTA Photomask), one for each layer of the device, were used to pattern SU-8 negative epoxy photoresist (MicroChem Corp.) onto clean silicon wafers (University Wafer Inc.). SU-8 2005 was used to build the first layer (cell trapping region) and was spun at 3250 rpm while SU-8 2015 was used to build the second layer (main channels), spun at 2000 rpm. These spin parameters yield approximately 4.3 μm and 20 μm tall features for the cell trapping and main channel layers respectively, as measured by a Dektak 150 surface profiler (Veeco Instruments Inc.). The mask for the second layer was aligned to the first layer of the wafer using an EVG620 mask aligner (EV Group Inc.). Once patterning of the SU-8 was complete, the wafer was exposed to 40 μl of trichloro(1H, 1H, 2H, 2H-perfluoro-octyl)silane (Sigma-Aldrich Co.) in a vacuum chamber for 7 minutes. After this, poly-dimethylsiloxane (PDMS, Sylgard 184, silicone elastomer kit with base and curing agent, Dow Corning Corp.) molds of the features on the wafer were made, cleaned and bonded to glass coverslips for experiments as described in Ferry et al [23]. Other yeast aging devices described in this chapter were built similarly using these methods.

Strain information can be found in Chapter 4 tests done in three inlet yeast aging device (Fig. 2.5). Strain information and details for experiments using the 4-unit variant of the aging device can be found in Li et al. 2019 [85]. Cell divisions were recorded manually by monitoring the seperation of the mother and daughter nuclei, visualized by the Nhp6a-iRFP reporter present in all strains. Likewise other details of the microfluidic experiments can be found in Chapters 3 and 4. Experimental details relevant to the use of the 4-unit device can be found in Li et al. 2019 [85].

2.5 Acknowledgements

This chapter contains material that was originally published from the following papers.

· Baumgartner, B.L.*, O'Laughlin, R.*, Jin, M.*, Tsimring, L.S., Hao, N. and Hasty, J., 2018.

Flavin-based metabolic cycles are integral features of growth and division in single yeast cells. *Scientific Reports*, 8(1), pp.1-10. (*equal contribution). Reproduction of this work was granted by Springer Nature under the Creative Commons Attribution 4.0 International License (https://creativecommons.org/licenses/by/4.0/). The dissertation author, Richard O'Laughlin, was a primary investigator and author of this work.

· Li, Y.*, Jin, M.*, O'Laughlin, R.*, Bittihn, P., Tsimring, L.S., Pillus, L., Hasty, J. and Hao, N., 2017. Multigenerational silencing dynamics control cell aging. Proceedings of the National Academy of Sciences, 114(42), pp.11253-11258.(*equal contribution). The dissertation author, Richard O'Laughlin, was a primary investigator and author of this work.

· O'Laughlin, R., Jin, M., Li, Y., Pillus, L., Tsimring, L.S., Hasty, J. and Hao, N., 2019. Advances in quantitative biology methods for studying replicative aging in Saccharomyces cerevisiae. Translational Medicine of Aging. (in press). Permission was granted by Elsevier to reprint material from this article in this thesis. The dissertation author, Richard O'Laughlin, was a primary investigator and author of this work.

This chapter also contains work that has been submitted for publication as:

· Li, Y., Jiang, Y., Paxman, J., O'Laughlin, R., Klepin, S., Zhu Y., Pillus, L., Tsimring, L.S., Hasty, J. and Hao, N. A programmable fate decision landscape underlies single-cell aging in yeast. The dissertation author, Richard O'Laughlin, was a primary investigator and author of this work.

This work was initially placed on the bioRxiv preprint server as:

· Li, Y., Jiang, Y., Paxman, J., O'Laughlin, R., Pillus, L., Tsimring, L.S., Hasty, J. and Hao, N., 2019. An epigenetic landscape governs early fate decision in cellular aging. bioRxiv, p.630921. The dissertation author, Richard O'Laughlin, was a primary investigator and author of this work.

This chapter also contains the following material that is currently being prepared for submission for publication.

- O'Laughlin, R, Li, Y., Pillus, L., Tsimring, L.S., Hasty, J. and Hao, N. "A high-throughput and adaptive microfluidic platform for monitoring yeast replicative aging." (in prep)(title tentative). The dissertation author, Richard O'Laughlin, was a primary investigator and author of this work.

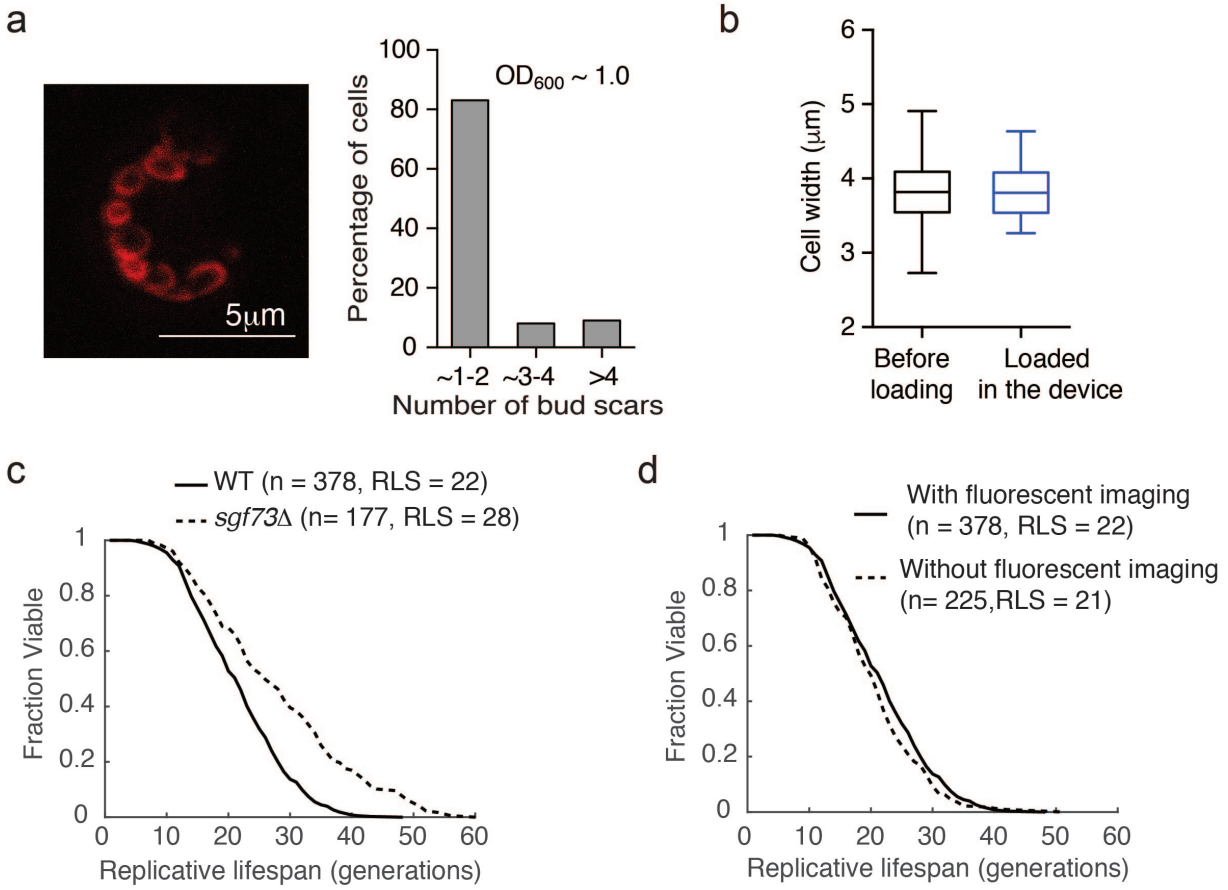

Figure 2.6: Validation of the yeast aging microfluidic device. (a) Left: A representative confocal image showing bud scars stained with wheat germ agglutinin (WGA). Right: Bud scar distribution of cells at OD600 of approximately 1.0. (b) A boxplot showing the distributions of cell widths for cells from the culture population before loading (black) and cells loaded in the device (blue). Snapshot images were taken with cells from the culture population immediately before loading or with cells just loaded into the device, respectively. Cell widths for single cells were quantified using ImageJ. In the plot, the bottom and top of the box are first (the 25th percentile of the data, q1) and third quartiles (the 75th percentile of the data, q3); the band inside the box is the median; the whiskers cover the range between q1-1.5 x (q3-q1) and q3+1.5 x (q3-q1). These results confirm that the device loading does not select for a subpopulation of cells.(c) Replicative lifespans measured using the microfluidic device. Lifespan curves have been shown for WT and *sgf73*Δ cells in SC medium supplemented with 2% glucose. In our device, deletion of SGF73 increases lifespan by 27% comparing to that of WT, consistent with the previouse reprot (McCormick et al. [84], Cell Metabolism 2015, Table S2; the sgf73 mutant increases lifespan by 25.8% in MATa strains). (d) Replicative lifespans measured in the device with or without fluorescent imaging. Fluorescent imaging setting and acquisition frequency are given in the Methods section of Chapter 4. For experiments without fluorescent imaging, only phase images (50 ms exposure) were taken every 15 mins.

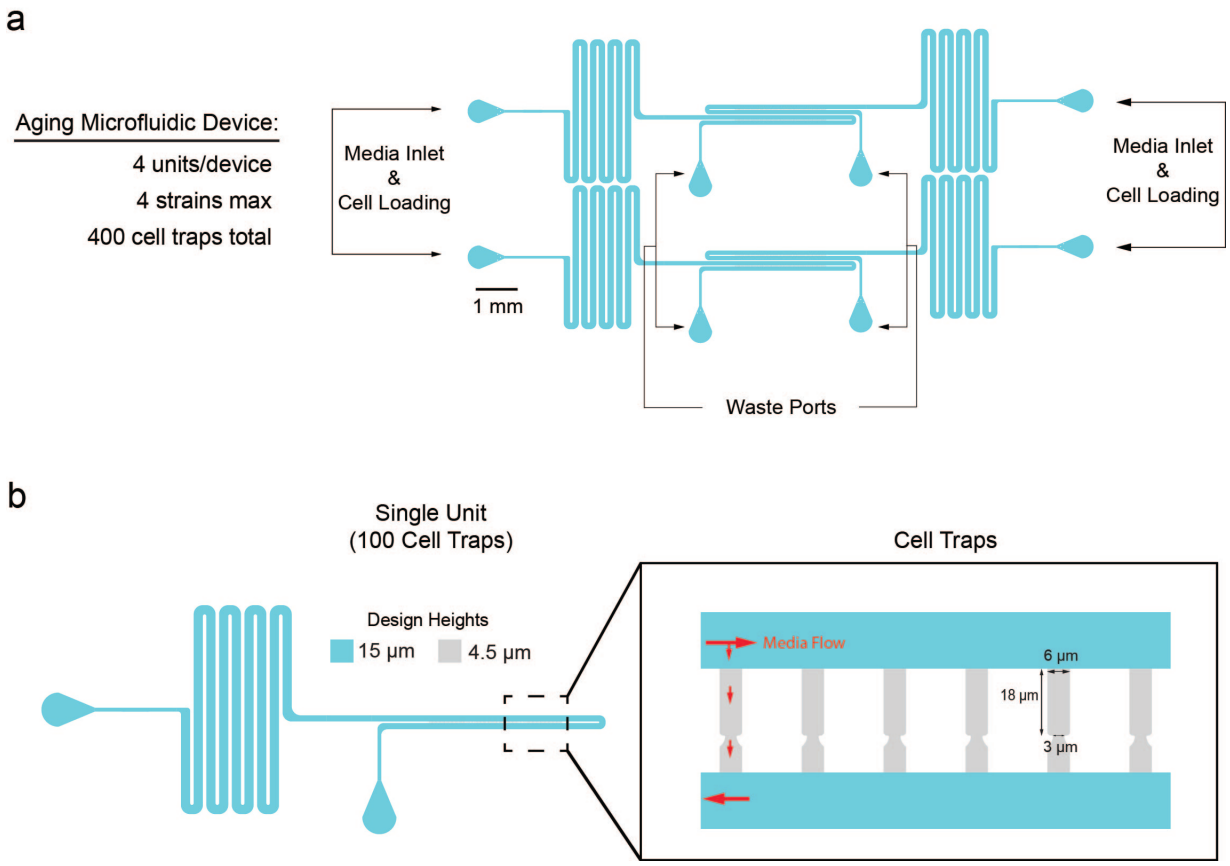

Figure 2.7: The 4-strain redesign of the first generation yeast aging microfluidic device. (a) Device layout for the redesign of the first generation device, with 400 traps per device and 4 individual units which allow 4 different strains to be analyzed in a single experiment. (b) Close-up of a single unit of the device, which has one inlet and one outlet.

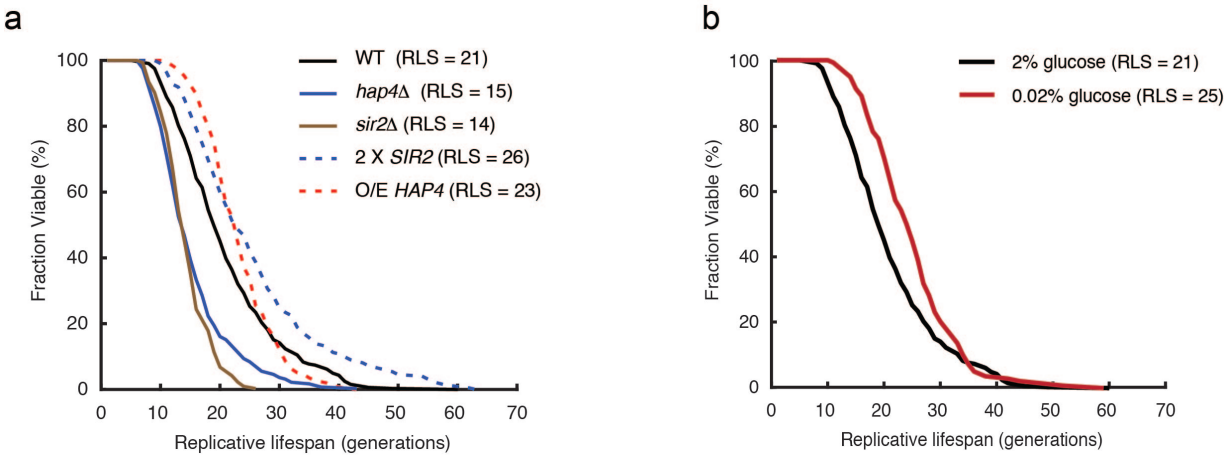

Figure 2.8: Lifespan validation of the 4-unit yeast aging chip. (a) Lifespan measurement of WT cells (n = 189 cells) and different longevity mutants. Double expression of SIR2, a histone deacetylase, results in lifespan extension (n = 222 cells), while deletion (*sir2*Δ, n = 98 cells) results in a much reduced mean RLS, demonstrated by Kaeberlein et al. [86], and also demonstrated in the microfluidic device. We found that deletion of HAP4 (n = 99 cells), involved in regulating cellular respiration [87], resulted in a decreased RLS while overexpression of HAP4 with the GPD promoter (n = 123 cells) had a mean RLS close to that of WT. (b) Lifespan extension under calorie restriction conditions (n = 138 cells). Similar to the microfluidic device study by Jo et al. [66], we found that dramatically reducing the glucose level in the media (in our case a 100-fold reduction in glucose from 2% weight by volume to 0.02%) resulted in lifespan extension.

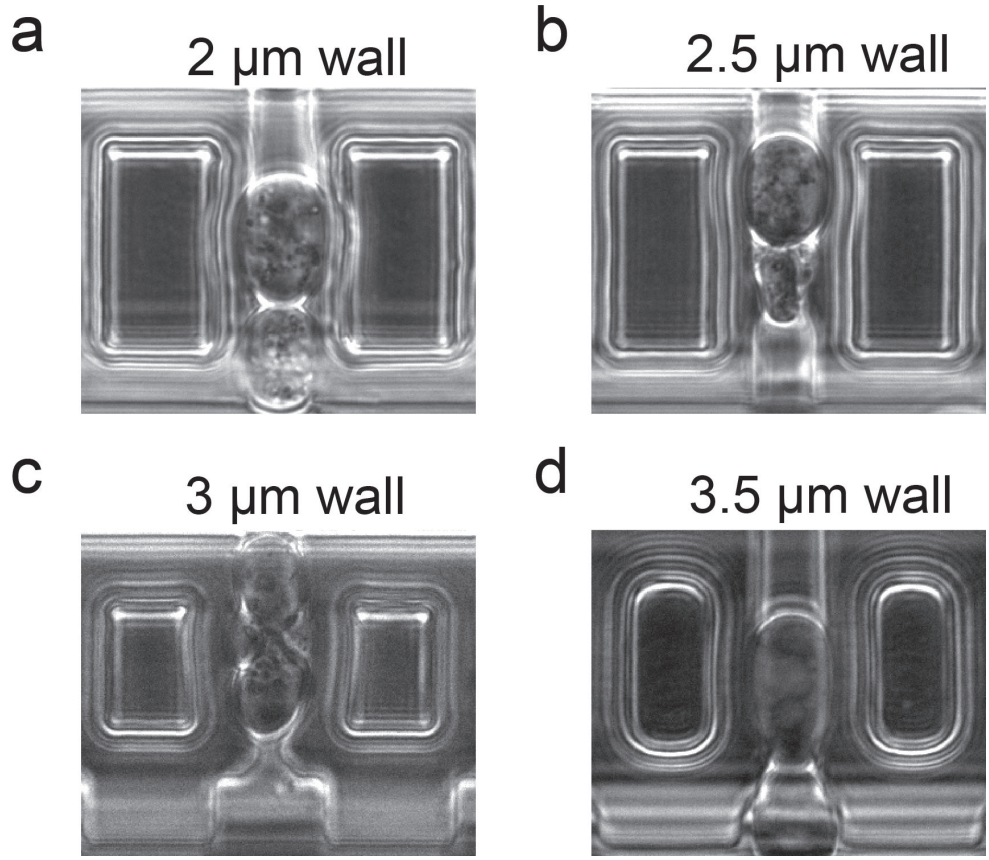

Figure 2.9: Flexible cell traps for a second generation of yeast aging microfluidic devices. (a) Flexible traps with a 2 μm wall. (b) Flexible traps with a 2.5 μm wall. (c) Flexible traps with a 3 μm wall. (d) Flexible traps with a 3.5 μm wall. Cells were able to stretch the width of the traps in all cases. The shapes of the cell traps were slightly varied in each case.

Chapter 3

Single-cell analysis of metabolic cycling during growth and division in yeast using microfluidics

3.1 Introduction

Oscillations underlie a wide variety of biological phenomena. Their unique dynamical characteristics allow organisms across diverse kingdoms of life and at multiple length scales to perform a myriad of complex functions such as timekeeping [88], resource allocation and sharing [89], as well as coordinated behavior [90]. At the level of single cells, the networks of interacting genes and proteins that generate oscillatory behavior have traditionally been the focus of investigation [88, 91–94]. However, it is becoming increasingly clear that metabolic processes are also capable of periodic behavior, and that these oscillations may be integral parts of core biological processes such as glycolysis [95, 96], the cell division cycle [97–99] and circadian rhythms [100, 101].

3.1.1 The yeast metabolic cycle (YMC)

One of the most well-studied examples of metabolic oscillations is known as the yeast metabolic cycle (YMC). Since its initial observations about 50 years ago [102, 103], the YMC has come to be known as the bursts of respiratory metabolism and oxygen consumption by synchronized cultures of budding yeast growing in a nutrient-limited chemostat environment [104–106]. It has been shown that these oscillations correspond to a global coordination of cellular activity, where specific stages of the dissolved oxygen oscillations are associated with the expression of certain genes, the accumulation of distinct metabolites and progression through different phases of the cell division cycle [105, 107, 108]. Yet, despite the importance of these findings, the extent to which the many features of the YMC are recapitulated at the single-cell level remains to be determined. Answering these questions is made all the more difficult by the fact that different experimental set-ups can lead to markedly different observations about the period of the metabolic cycle and its relationship to the cell division cycle. For example, varying the strain background and chemostat conditions can lead to YMC periods ranging from 40 minutes [104, 106] to 5 hours [105], and the YMC can even oscillate multiple times per cell cycle [109] in specific deletion mutants or possibly disappear altogether at certain dilution rates [110]. Indeed, answering questions about the biological basis of metabolic cycles is challenging using synchronized cultures because it is difficult to decouple perturbations that affect cycling from those that merely prevent synchrony. As such, studies that could directly observe the dynamics of metabolism in single yeast cells would circumvent many of these challenges and greatly facilitate understanding of the mechanisms that generate the YMC.

Toward this end, seminal work by Papagiannakis et al. [99] demonstrated the existence of metabolic cycles in the form of NAD(P)H and ATP oscillations in unsynchronized single yeast cells growing in a microfluidic device. A critical finding from their work was that cell cycle progression was synchronized with and gated by the metabolic cycle [99] in multiple different media conditions. This distinguishes these oscillations from previously described

glycolytic oscillations in single yeast cells, which are associated with NADH [95,96] and pH [96] oscillations that have periods of approximately one minute [95,96] and appear to not manifest in all conditions [111,112] or in all cells of a population [96,113]. While the work by Papagiannakis et al. [99] establishes the existence of metabolic oscillations in single cells and supports previous findings [114–116] along this line, questions remain about the degree to which other features of the YMC, as observed in synchronized chemostat cultures, are also extant at the single-cell level.

In this chapter, we used novel microfluidic technology and time-lapse fluorescence microscopy to directly observe and quantitatively characterize the dynamics of metabolic cycling in unsynchronized single yeast cells. To accomplish this we monitored changes in cellular redox state via endogenous flavin fluorescence. We observed clear and robust oscillations that displayed the expected phase relationships relative to the cell division cycle as reported from YMC chemostat studies [105,107,110]. Our results indicate that the metabolic cycle is a robust oscillator that typically couples one-to-one to the cell division cycle across four different nutrient conditions, however, we found that treatment with rapamycin can alter phase synchrony between these two oscillators, leading to multiple metabolic cycles per CDC and increased variability of metabolic cycling. Additionally, in contrast to the chemostat studies of the YMC, we found that cellular respiration is dispensable for metabolic cycling, as flavin oscillations persisted in deletion mutants impaired in oxidative phosphorylation. These results are in general agreement with the previous findings from Papagiannakis et al. [99], and demonstrate that another critical cellular metabolite, flavin, also oscillates during the cell division cycle. Our work provides new insights into metabolic cycling in budding yeast and provides a foundation and methodology for future studies of its role at the level of single cells.

3.2 Results

3.2.1 Tracking metabolic cycles in single-cells via endogenous flavin fluorescence

To investigate metabolic cycling in unsynchronized single cells, we designed a custom microfluidic device to minimize the accumulation of possible synchronizing agents such as hydrogen sulfide and acetaldehyde . At the high cell densities experienced in chemostats, such compounds are thought to accumulate in the media and synchronize nearby cells by phase shifting the YMC [106, 117]. Our microfluidic platform minimizes such effects by trapping single cells in physically isolated monolayer columns (Chapter 2.3.1), thus preventing cell-to-cell communication. Experiments were conducted with the CEN.PK strain previously shown to produce metabolic cycles with a period of several hours in chemostat environments [105].

As a readout of metabolic cycling, we used the natural redox-sensitive fluorescence of riboflavin, flavin mononucleotide (FMN) and flavin adenine dinucleotide (FAD). It has been shown that the abundance of these molecules is highly periodic during the YMC in chemostats, exhibiting a near anti-phase relationship with the dissolved oxygen concentration [106, 107]. We reasoned that we could utilize flavin molecules as dynamic reporters of metabolic cycling in single cells because of their unique fluorescent properties; they fluoresce in the visible spectrum (peak excitation/emission: 450/535 nm) [118] and their reduced equivalents ($FADH_2$ and $FMNH_2$) have negligible fluorescence in this range [119], allowing their oxidized and reduced states to be distinguished. This approach obviates the need for expression of fluorescent proteins as YMC reporters, which may not be dynamic enough to observe multiple cycles or could influence the natural period.

We used a customized filter cube (excitation at 438-458 nm and emission at 515-565 nm) to image flavin fluorescence during time-lapse microscopy experiments (Fig. 3.1a). The flavin fluorescence signal was clearly visible in individual cells growing in the microfluidic device

(Fig. 3.1b) and exhibited good dynamic range, increasing more than 2-fold with the addition of hydrogen peroxide to the media (Fig. 3.6). By imaging and tracking individual cells growing in minimal yeast nitrogen base (YNB) media, we observed strikingly clear oscillations in flavin fluorescence over multiple cell divisions (Fig. 3.1c).

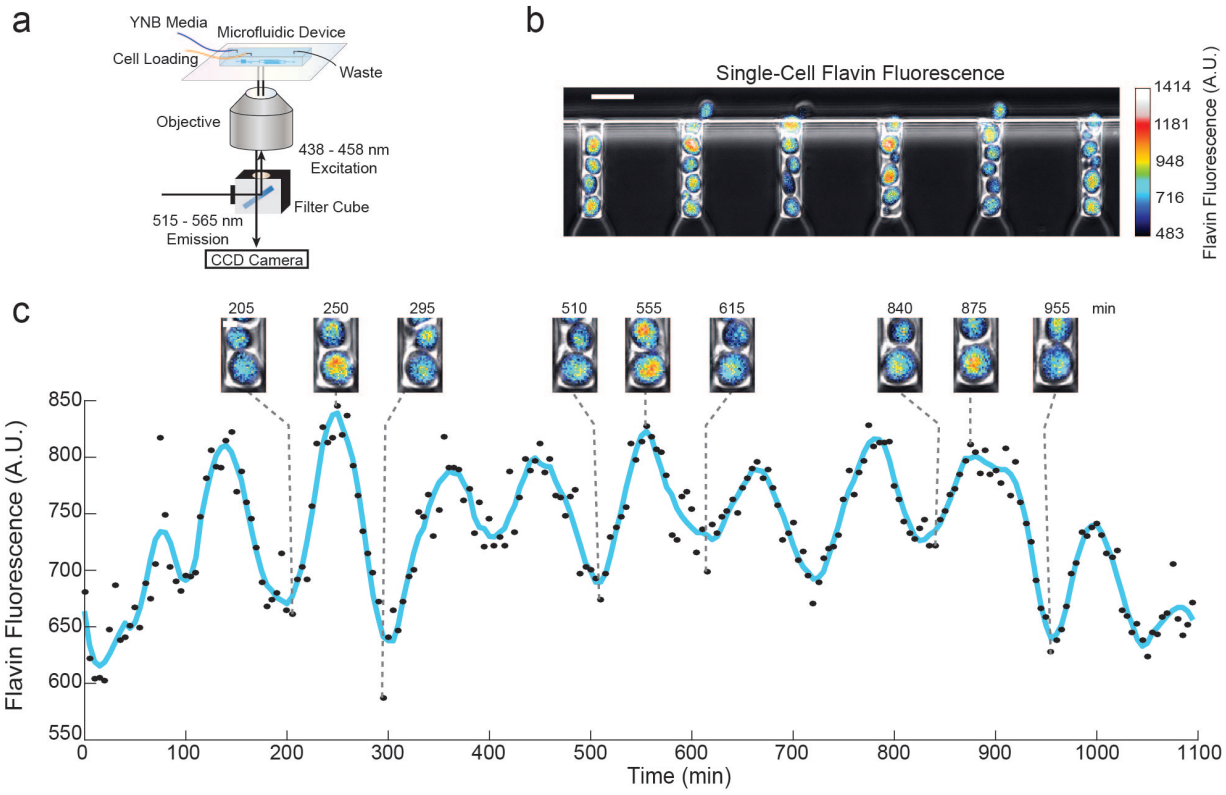

Figure 3.1: Flavin oscillations in single yeast cells.(a) Experimental setup for observing flavin oscillations in single cells. (b) Snapshot of flavin fluorescence in single cells growing in the microfluidic device during an experiment. The phase and flavin fluorescence channels were overlayed and false coloring using the ImageJ [120] 'royal' colormap was applied to the flavin channel in order to increase visual contrast for presentation. The colorbar to the right indicates the intensity of the measured flavin signal [120]. The scale bar is 10 μm. (c) Single-cell trajectory of measured flavin fluorescence including snapshots of the cell undergoing oscillations at the labeled time points. The color bar is the same as in panel b. The scale bar is 2 μm.

Having observed oscillatory flavin dynamics in single cells, we next sought to determine the extent to which these oscillations were related to the metabolic cycles reported in chemostat cultures. The cell division cycle has been shown to be highly correlated with phase specific

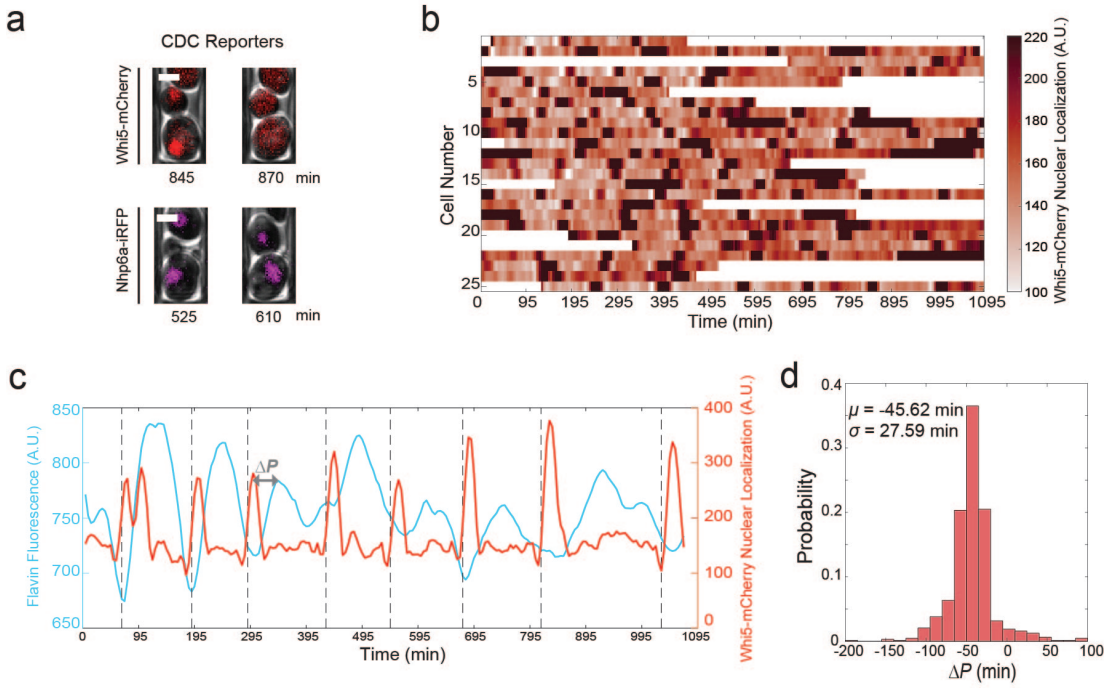

Figure 3.2: Tracking the dynamics of flavin fluorescence relative to the cell division cycle. (a) Snapshots of the dynamics of fluorescent markers of the cell division cycle in single cells. Fluorescently tagged proteins Whi5-mCherry and Nhp6a-iRFP were used for demarcating the early and late phases of the cell cycle respectively. All scale bars are 2 μm. (b) Representative heatmap of Whi5-mCherry nuclear localization from 25 single cells as a visual aid to demonstrate a lack of CDC synchrony. (c) Example trace of flavin and Whi5-mCherry fluorescence measured in the same single cell. Pulses of the Whi5-mCherry signal correspond to nuclear localization. The lag time between the Whi5-mCherry and flavin peaks was denoted as ΔP and was calculated as the difference between the time of the Whi5-mCherry peak and the flavin fluorescence peak within each cell division cycle. The black dotted vertical lines indicate separation of the mother and daughter nuclei as visualized by the Nhp6a-iRFP reporter. (d) Distribution of the time difference between flavin and Whi5-mCherry peaks (n = 156 cells, the mean (μ) and standard deviation (σ) for the distribution are ΔP = -45.62 $\pm$ 27.59 minutes).

processes during the YMC in synchronized cultures, with budding occurring near the trough of the oxygen oscillations in the chemostat [105, 110]. Further, Papagiannakis et al. [99] demonstrated a strong coupling between NAD(P)H and ATP oscillations and the cell division cycle in single cells. Here, we decided to explore the quantitative relationship between the observed flavin oscillations and the CDC. To accomplish this we constructed strains with fluorescent reporters that allowed us to monitor different phases of the cell division cycle. We analyzed the relationship of flavin

oscillations to the early part of the cell cycle by tracking the nuclear localization of Whi5-mCherry (Fig. 3.2a top row), which exits the nucleus before budding [121]. We also tracked how flavin oscillations related to the late part of the cell cycle by monitoring the separation of the mother and daughter nuclei using NHP6a-iRFP as a nuclear marker (Fig. 3.2a bottom row). By tracking Whi5-mCherry nuclear localization, we verified that cells growing in the microfluidic device were not synchronized (Fig. 3.2b), and subsequently moved to analyzing the relationship between the flavin oscillations and the early part of the cell division cycle. We found that the flavin signal reached its peak shortly after Whi5-mCherry exited the nucleus (Fig. 3.2c, Fig. 3.7). Peak nuclear localization of Whi5-mCherry occurred approximately 45 minutes before the peak of the flavin signal (Fig. 3.2d). The troughs of the flavin oscillations closely corresponded with the separation of the mother and daughter nuclei (Fig. 3.2c dashed lines). The timing of the flavin peak relative to the CDC is consistent with findings from synchronized chemostat cultures [107] and also closely matches the timing of peak NAD(P)H fluorescence observed by Papagiannakis et al. [99]

These findings validate our use of flavin fluorescence as a reliable reporter of metabolic cycling in single cells. Further, by using fluorescent reporters to monitor the cell division cycle we were able to demonstrate that cells growing in the microfluidic device are not synchronized and that the flavin dynamics, with respect to the CDC, in single cells are similar to those observed for synchronized chemostat cultures [107, 110]. Having validated our methodology and uncovered evidence of metabolic cycling, we next sought to quantify properties of the metabolic cycle and further explore its relationship with the cell division cycle in single cells.

3.2.2 Metabolic cycles are synchronized with the cell division cycle across different nutrient conditions

We then turned to investigate the dynamics of the metabolic cycle and its coupling to the cell division cycle under different nutrient environments. First, we measured flavin oscillations in unsynchronized cells growing in media with a range of yeast nitrogen base (YNB) concentrations.

For media preparation, YNB containing ammonium sulfate as a nitrogen source, as well as other nutrients such as vitamins and minerals, was diluted relative to 1X YNB media. We also tested the effect of varying the nitrogen source alone by analyzing cells growing in 1X YNB media with urea as the nitrogen source, a non-preferred option for yeast [122]. In all four media conditions the level of glucose was kept constant at 1%.

Metabolic cycles robustly persisted in all nutrient environments, with more than 150 cells being analyzed in each experiment. Multiple example traces can be seen in Fig. 3.8 and Fig. 3.9. For cells in each media condition, we determined the period of the metabolic cycle and the cell division cycle (Fig. 3.3a, see Fig. 3.10 for estimation of metabolic cycle periods using autocorrelation analysis). The relative coupling between the metabolic cycle and CDC was quantified by measuring the lag time between the trough of the metabolic cycle and the separation of the mother and daughter nuclei at the end of each CDC. This quantity and was termed ΔT (Fig. 3.3a).

Across all media conditions one metabolic cycle accompanied each CDC in at least 85% of all cases. (Fig. 3.3b). As nutrient quality of the media decreased, the mean period of the metabolic cycle increased. The 1X YNB and 0.25X YNB conditions gave similar mean metabolic cycle periods of $\sim$136 minutes and the less nutrient-rich 0.05X YNB and 10 mM urea conditions both gave mean periods of $\sim$163 minutes. The period of the metabolic cycle and the cell division cycle were similar for all nutrient conditions as well (Fig. 3.3c). For the 1X YNB and 0.25X YNB conditions the median CDC and metabolic cycle times were both 130 minutes (Fig. 3.3c). For the 0.05X YNB condition the median CDC time was 160 minutes, while the median metabolic cycle time was 150 minutes, and both the median CDC and metabolic cycle times were 150 minutes in the 10 mM urea media (Fig. 3.3c). These results suggest that the metabolic cycle can function over a range of periods, and that it is tuned along with the cell division cycle in accordance with the nutrient conditions of the environment.

Phase synchronization of the metabolic cycle and cell division cycle was further estab-

lished by analyzing the ΔT values for cells in each nutrient condition. Regardless of the length of the CDC, separation of the mother and daughter nuclei occurred, in almost all cases, near a metabolic cycle trough in all four media conditions (Fig. 3.3d and e). Taken together, these findings suggest that the CDC is strongly coupled to and gated by the metabolic cycle; division of the mother and daughter nuclei occurs at a relatively fixed time near a trough of the metabolic cycle. This is true even for prolonged cell division cycles where the metabolic cycle can oscillate multiple times before division occurs. Further, these results demonstrate that carbon source limitation, as commonly used in the literature [105, 110], is not a requirement for generating or modulating the metabolic cycle.

3.2.3 Rapamycin perturbs the phase synchronization of the metabolic cycle and CDC

The strong relationship we found between the metabolic cycle and CDC in different media conditions led us to investigate ways in which we could possibly alter the relationship between these two oscillators. Since previous work in synchronized cultures showed that the addition of rapamycin can phase shift metabolic cycles into a prolonged reductive phase [108], and that rapamycin is a known CDC inhibitor [123], we reasoned that it could be used to perturb the connection between the metabolic cycle and the cell division cycle.

When cells were grown in 1X YNB media in the presence of 150 nM rapamycin around half of the cells continued dividing but at a greatly reduced rate. In such cases we often observed multiple metabolic cycles occurring within a single cell division cycle (Fig. 3.4a left panel and Fig.3.11). Other cells divided only once or were delayed in the early phases of the CDC and did not complete a full division during the course of our experiment, yet metabolic cycles were able to continue in these cells as well (Fig. 3.4a right panel). Overall, there was an increase in the number of metabolic cycles occurring in each cell division cycle. In 1X YNB without rapamycin about 90% of all cell divisions condition contained only one metabolic cycle (Fig. 3.3b) while this

dropped to less than 50% with the addition of rapamycin (Fig. 3.4b). Cells exposed to rapamycin had a significantly greater ($P < 0.0001$) number of metabolic cycles during each CDC than cells in the 1X YNB condition without rapamycin (Fig. 3.4c).

Compared to the cells in 1X YNB media without rapamycin (Fig. 3.3c), the period of the metabolic cycle and cell division cycle was much longer in the rapamycin exposed cells (Fig. 3.4d). Indeed the mean metabolic cycle period of the rapamycin treated cells was more similar to that of cells grown in 0.05X YNB media (191.73 ± 75.41 min for rapamycin treated cells and 162.80 ± 47.52 min for cells in 0.05X YNB media). Although exposure to rapamycin increased the period of both the metabolic cycle and CDC, the metabolic cycle was not prolonged to the same extent as the cell division cycle. The mean CDC time in rapamycin was $\sim$190% greater than without, while the mean metabolic cycle period was increased $\sim$40% (Fig. 3.4d and Table 3.3). Interestingly, despite the differences in mean metabolic and cell division cycle periods, nuclear separation between the mother and daughter nuclei still occurred close to a metabolic cycle trough (Fig. 3.4e). Additionally, there was a loss of periodicity in the metabolic cycle, where successive period times became more irregular (Fig. 3.4f).

These findings demonstrate that rapamycin can affect the phase synchrony of the metabolic cycle and CDC. Under these conditions we observed more instances of multiple metabolic cycles occurring before a cell division event, however nuclear division of mother and daughter nuclei still occurred near the metabolic cycle trough, just as in 1X YNB media without rapamycin. Furthermore, metabolic cycles could persist even without cells completing the cell division cycle. These results support the model proposed by Papagiannakis et al. [99] where CDC progression is gated by an autonomous metabolic oscillator.

3.2.4 Metabolic cycling continues in respiratory deficient mutants

Having established that metabolic cycles occur under multiple conditions and can be decoupled from the cell division cycle, we turned to studying the role of cellular respiration in

metabolic cycling. Chemostat studies of the YMC have mainly used the dissolved oxygen content in the media as a readout of the YMC [104–106]. Indeed, cellular respiration has been viewed as instrumental to the function of these cycles, as the yeast metabolic cycle has sometimes been referred to as yeast respiratory oscillations [124–126]. However, given that such studies have been conducted using synchronized chemostat cultures, it remains unclear if oxidative respiratory metabolism is required for metabolic cycles to occur, or if that mode of metabolism is simply the most favorable for synchronizing the culture and generating oscillations.

To address this question, we tracked the dynamics of flavin fluorescence in the respiratory-deficient *atp5*Δ and *cyt1*Δ strains growing in 1X YNB media. The *ATP5* gene codes for a subunit of the ATP synthase complex [127] while the *CYT1* gene codes for cytochrome *c*1 [128]. Both are critical components of mitochondrial respiration, and both genes have been shown to be required for respiratory growth [129, 130]. We verified that the *atp5*Δ and *cyt1*Δ strains in the CEN.PK background were respiratory deficient by growing cells on the non-fermentable carbon source glycerol. No growth of either strain was observed on YPG (yeast extract, peptone and 3% glycerol) plates over the course of two days (Fig. 3.5a). Further, *atp5*Δ and *cyt1*Δ cultures did not exhibit post-diauxic shift growth, also indicating an inability to carry out respiratory metabolism [130] (Fig. 3.5b). Despite this, we continued to observe metabolic cycles in these strains (Fig. 3.5c, d and Fig. 3.12). As in other media conditions tested (Fig. 3.3), predominantly one metabolic cycle occurred per CDC (Fig. 3.5e), and separation of mother and daughter nuclei was near a metabolic cycle trough (Fig. 3.5f). These results suggest that metabolic cycles are respiration independent, as neither their maintenance nor their coupling to the cell division cycle were significantly effected in the *atp5*Δ and *cyt1*Δ strains.

3.3 Discussion

Elucidating the workings of biological processes often benefits from multiple methods of investigation. Through the use of microfluidics and time-lapse fluorescence microscopy we directly observed metabolic cycling in single yeast cells. These metabolic cycles operated across four different nutrient conditions, could exist synchronized and unsynchronized with the cell division cycle, continued without the need of significant cellular respiration and seemed to gate progression of the CDC. These findings both validate and expand the current understanding of metabolic cycles and build off of the work reported in foundational studies conducted with synchronized cultures [104, 105, 109, 110, 117, 124, 125] and in single cells [99]. The unique insights provided in this work by analyzing single cells suggests that metabolic cycling is an integral feature of yeast metabolism that is not confined to any specific environmental condition.

With regard to the generality of metabolic cycles in different yeast strains, it is of particular interest that Papagiannakis et al. [99] conducted their work in the YSBN strain background (derived from S288C [131]), while we carried out our work in the CEN.PK strain background. It has been shown that these two popular lab strains have key differences in their metabolism, particularly with respect to amino acid and protein synthesis as well as glucose catabolism, that manifest as differences in maximal specific growth rate [131]. Yet, despite these differences between the two strains, metabolic cycles with similar periods were observed in both strains [99]. Our work here and that of Papagiannakis et al. [99] support the notion that metabolic cycling is a general phenomenon that occurs across different yeast strains in coordination with the cell division cycle.

The single-cell approach to studying metabolic cycles could offer a whole host of interesting research directions, as the dynamics of cellular metabolic activity can be studied in relationship to numerous other processes. Perturbations to chromatin regulation, cellular redox state and specific metabolic pathways have yielded interesting insights into YMC dynamics in

synchronized cultures [132] and such results could be greatly complemented by similar studies at the single-cell level. Hypotheses regarding the biological functions of the metabolic cycle, such as its possible role as a biological clock in the cell aging process [125], could be investigated using the methods described here combined with microfluidic technology capable of studying dynamic processes during cell aging as recently described [68, 133, 134]. Additionally, it has been proposed that signaling networks such as target of rapamycin complex I (TORC1) and protein kinase A (PKA) could play important roles in metabolic cycling [98]. This hypothesis is supported by our data showing that rapamycin can slow the metabolic cycle (Fig. 3.4) and that respiratory related mitochondrial activity does not appear to play a critical role in generating or maintaining metabolic cycles (Fig. 3.5). As the TOR and PKA regulated processes of ribosome biogenesis and translation are both energetically costly and critically important for cell growth and entry into division [98, 135], a connection with the metabolic cycle is an intriguing possibility. Indeed, as metabolic cycles are studied in greater detail, they may come to be critically important for our understanding of how cells function, as they represent one more biological knob that can be dynamically modulated to optimize cellular fitness.

3.4 Methods

3.4.1 Yeast strains and growth conditions

In all experiments prototrophic strains derived from the haploid CEN.PK2-1c strain (MATa, trp1-289, his3Δ1, ura3-52, leu2-3_112) were used (Table 3.1). The CEN.PK2-1c strain was purchased through EUROSCARF (Accession Number: 30000A) and standard yeast integration vectors were used to repair auxotrophies (Table 3.1).

The standard lithium-acetate method was used for transformations. Before experiments, cells were cultured overnight in 1X yeast nitrogen base (YNB) media that contained 6.7g/L of

Table 3.1: YMC parent strain, strains constructed and strains used in experiments. To repair the histidine, leucine and uracil auxotrophies the parent strain CEN.PK2-1c was transformed with standard yeast integration plasmids pRS403 (for repair of histidine auxotrophy), pRS405 (for repair of leucine auxotrophy), or pRS406 (for repair of uracil auxotrophy) where indicated below. To repair the tryptophan auxotrophy we used restriction enzymes to swap a Trp1 selection marker from a pFA6 plasmid into a pKT-mCherry plasmid, replacing the kanMX marker. We then PCR amplified the mCherry-Trp1 fragment and inserted it at the C-terminal end of the *WHI5* gene using standard lithium acetate transformation. Similarly, iRFP-kanMX was PCR amplified and inserted at the C-terminal end of the *NHP6a* locus. Colony PCR was used to verify insertions. To create the respiratory deficient deletion mutants the hphMX marker was PCR amplified from plasmid pAG32 and the natNT2 marker was amplified from plasmid pFA6-natNT2. Colony PCR was used to verify deletions.

Strain Name	Genotype	Additional Details
CEN.PK2-1c	MATa; his3Δ1; leu2-3_112; ura3-52; trp1-289; MAL2-8c; SUC2	Parent strain. Purchased from EUROSCARF (Accession Number: 30000A)
yBB107	CEN.PK2-1c his3::pRS403, leu2::pRS405, ura3::pRS406	Constructed for this study
yBB108	CEN.PK2-1c leu2::pRS405, ura3::pRS406	Constructed for this study
yBB109	CEN.PK2-1c his3::pRS403, leu2::pRS405	Constructed for this study
yYMC1	CEN.PK2-1c his3::pRS403, leu2::pRS405, ura3::pRS406, Nhp6a-iRFP-kanMX, Whi5-mCherry-Trp1	Constructed for this study
yYMC4	CEN.PK2-1c his3::pRS403, leu2::pRS405, ura3::pRS406, Nhp6a-iRFP-kanMX, Whi5-mCherry-Trp1, *cyt1*::hphMX	Constructed for this study
yYMC5	CEN.PK2-1c his3::pRS403, leu2::pRS405, ura3::pRS406, Nhp6a-iRFP-kanMX, Whi5-mCherry-Trp1, *atp5*::natNT2	Constructed for this study

Difco yeast nitrogen base without amino acids (Becton, Dickson and Company) and 1%(wt/vol) glucose (Sigma-Aldrich). The day of the microfluidics experiment the overnight culture was diluted in 1X YNB media to an OD600 of 0.05 and grown to a final OD600 between 0.2 and 0.6 before being loaded into the microfluidic device. In experiments where 0.25X YNB or

0.05XYNB media was used, yeast nitrogen base without amino acids was diluted to 0.25X or 0.05X as indicated in sterile filtered deionized water. Glucose was kept constant at 1%(wt/vol) in all media conditions. For the 1X YNB with 10mM urea media, 1.7g/L of Difco yeast nitrogen base without amino acids and without ammonium sulfate (Becton, Dickson and Company) was used and 1%(wt/vol) glucose (Sigma-Aldrich) was added. Urea (Sigma-Aldrich) was added to a final concentration of 10mM and the pH was then adjusted to 5.4 to match that of the standard 1X YNB with ammonium sulfate. The rapamycin (Sigma-Aldrich) was added to a final concentration of 150 nM.

For assessing the respiratory growth of the WT, *atp5*Δ and *cyt1*Δ strains, overnight cultures were diluted to an OD600 of 0.3, 0.03, 0.003 and 0.0003, then spotted on YPD (1% bacto-yeast extract (Becton, Dickson and Company), 2% bacto-peptone (Becton, Dickson and Company), 2% glucose (Sigma-Aldrich)) and YPG (1% bacto-yeast extract (Becton, Dickson and Company), 2% bacto-peptone (Becton, Dickson and Company), 3% glycerol (v/v) (Sigma-Aldrich)) plates. Plates were incubated at 30°C and imaged after 24 and 48 hours using a BioDoc-It Imaging System (UVP). To test for post-diauxic shift growth, overnight cultures were grown in YPD media, diluted to an OD600 of 0.2 and 0.5μl was added to wells of a 96 well flat bottom tissue culture plate (Falcon) containing 50μl YPD. There were four biological replicate wells for each strain. A blank YPD well containing no cells was included, and surrounding wells were filled with water to prevent evaporation during the experiment. The plate was placed in a Infinite 200 PRO plate reader (Tecan) and grown at 30°C for 48 hours with 600nm absorbance values being recorded every 5 minutes. For data analysis, the value of the blank well at each time point was subtracted from each well. The mean and standard deviation across the four replicates was plotted in (Fig. 3.5b).

3.4.2 Microfluidics and time-lapse microscopy

Construction of the microfluidic device is described in Chapter 2.4.1.

Log-phase cells as described above were loaded into the microfluidic device with the appropriate media. Images were taken on a Nikon Eclipse Ti inverted microscope with a CoolSnap HQ2 camera (Photometrics) and Lumencor SOLA system (Lumencor) fluorescent light source at 60X magnification using an oil immersion objective. The microfluidic device was surrounded by a plexiglass case that maintained the temperature at 30°C throughout the experiment. Flavin fluorescence was measured using a customized filter cube (Semrock) that allowed excitation at 438-458 nm and emission at 515-565 nm. Exposure settings were 150 ms at 15% lamp intensity for flavin, 200 ms at 20% lamp intensity for mCherry and 100 ms at 15% lamp intensity for iRFP. For all fluorescent signals 2-by-2 binning was used. Images were acquired every 5 minutes for the 1X YNB experiment and every 10 minutes in all other experiments.

The Whi5-mCherry background strain (yYMC1 from Table 3.1) was used for experiments in Figures 3 and 4. The Whi5-mCherry background strain (yYMC1 from Table 3.1) was used to create the *atp*5Δ and *cyt*1Δ strain (yYMC4 and yYMC5 from Table 3.1). For Figure 5 the 'WT' strain in panels A and B is the Whi5-mCherry strain yYMC1. Experiments lasted approximately 18 hours for analyzing metabolic cycling in different nutrient environments (Fig. 3.3, 3.4 and 3.5).

3.4.3 Cell tracking and data analysis

Time-lapse image stacks were pre-processed in Image-J [120] for background subtraction and registration. Fluorescence values of single cells were obtained with custom MATLAB (Mathworks) scripts for cell tracking. We tracked and analyzed one viable cell at the bottom of each trap. Most cells eventually bud in the direction opposite the trap opening and move up the trap, eventually exiting it. In these cases we often tracked cells for some time before they exited the trap until the automated tracking code or manual tracking was no longer accurate or convenient for that cell. Cells tracked for less than 4.5 hours were excluded from analysis. In all experiments cell masks generated by tracking code were manually inspected to ensure their

accuracy, and manually edited when necessary. For period analysis, fluorescence trajectories were first detrended using a polynomial function of order 7 fit to the data. Each trace was then normalized by their maximum value and filtered using the MATLAB Savitzky-Golay filter. These smoothed trajectories were used for analysis where custom MATLAB scripts detected metabolic cycle peaks based on fixed and standardized criteria (Table 3.2).

Table 3.2: YMC Parameters for metabolic cycle peak detection. In order to quantify properties of the metabolic cycles we wrote custom MATLAB code that allowed peak and minima detection in metabolic cycles using a fixed set of criteria across all experiments. First, the data was detrended by fitting and then subtracting a polynomial of order 7 from the raw data. Qualitatively, the results did not depend on the order of polynomial used for detrending. In general, lower order polynomials failed to remove all baseline drift in the signal, which made applying uniform peak and minima detection difficult across different experiments, while higher order polynomials gave a very even baseline but ran the risk of adding peaks to a signal by being overly sensitive to noise. We found order 7 to be the best balance between these two concerns for our data. After the signal was detrended each signal was normalized according to its maximum and minimum value to between 0 and 1. A Savitsky-Golay filter of order 4 and frame length 17 was then applied to each signal. The MATLAB function 'findpeaks' was used on the filtered signals to detect peaks and mimima according to the specifications listed in the table below.

Order of polynomial used for detrending	7
Savitsky-Golay filter order	4
Savitsky-Golay frame length	17
Amplitude Threshold	0.09
Minimum distance between peaks	65 min
Minimum peak prominence	0.09
Minimum minima prominence	0.045
Minimum distance between	50 min

The period values were calculated by the code and obtained by determining the time between successive peaks (T_P) or successive minima (T_M). If a tracked cell appeared to become sickly or near death, we made special note of these cells and excluded from analysis cell division times that occurred one division before this and only considered fluorescence values that were five time points after this for peak and minima detection. For determining the cell division times, in all cases we manually recorded the separation times of the mother and daughter nuclei for

each single cell, with the division time being the time difference between each nuclear separation and the one that follows for the next division. For tracking the dynamics of Whi5-mCherry we followed the method used by Cai et al. [136] for determining nuclear localization, where, for each cell mask, we took the difference between the averages of the top five brightest pixels and of all other pixels in the cell mask. This process gave fluorescence traces with spikes that corresponded well to Whi5-mCherry nuclear localization. The peak of the Whi5-mCherry nuclear localization signal was taken to be the maximum peak value within each cell cycle. The color map used in Fig.3.2 and Fig.3.7 is from Thyung et al. [137] For quantifying the flavin fluorescence we took the mean intensity over the entire cell mask.

Table 3.3: Metabolic cycle and cell division cycle times for all experiments. The mean peak-to-peak metabolic cycle periods and CDC periods (calculated from successive nuclear division events as visualized by the Nhp6a-iRFP marker) are displayed for each experiment below. In some media conditions, there were cells that we tracked for only two cell divisions but during one of these divisions, our peak finding code did not detect a peak during one of the divisions. Therefore for such cells a peak-to-peak period could not be calculated, but a CDC period could; hence the one or two cell discrepancy in some cases. For the rapamycin experiment the difference in the number of cells used for metabolic cycle and CDC period calculation is due to the fact that some cells did not divide twice during the experiment, thus a CDC period was not able to be calculated.

Experiment	**Metabolic Cycle Period Mean (min)**	**Metabolic Cycle Period Standard Deviation (min)**	**Cell Division Cycle Mean (min)**	**Cell Division Cycle Standard Deviation (min)**	**Total Number of Cells for Calculation (Metabolic Cycle, CDC)**
1X YNB	135.91	40.56	142.53	45.95	155, 156
0.25X YNB	136.43	36.11	138.30	40.93	224, 225
0.05X YNB	162.80	47.52	178.83	63.73	174, 175
1X YNB with 10mM urea	161.48	54.52	181.19	90.49	174, 176
1X YNB with 150nM rapamycin	191.73	75.41	416.94	238.51	180, 85
atp5, 1X YNB	186.58	54.37	218.44	65.40	54, 54
cyt1, 1X YNB	162.81	42.04	168.70	53.20	51, 52

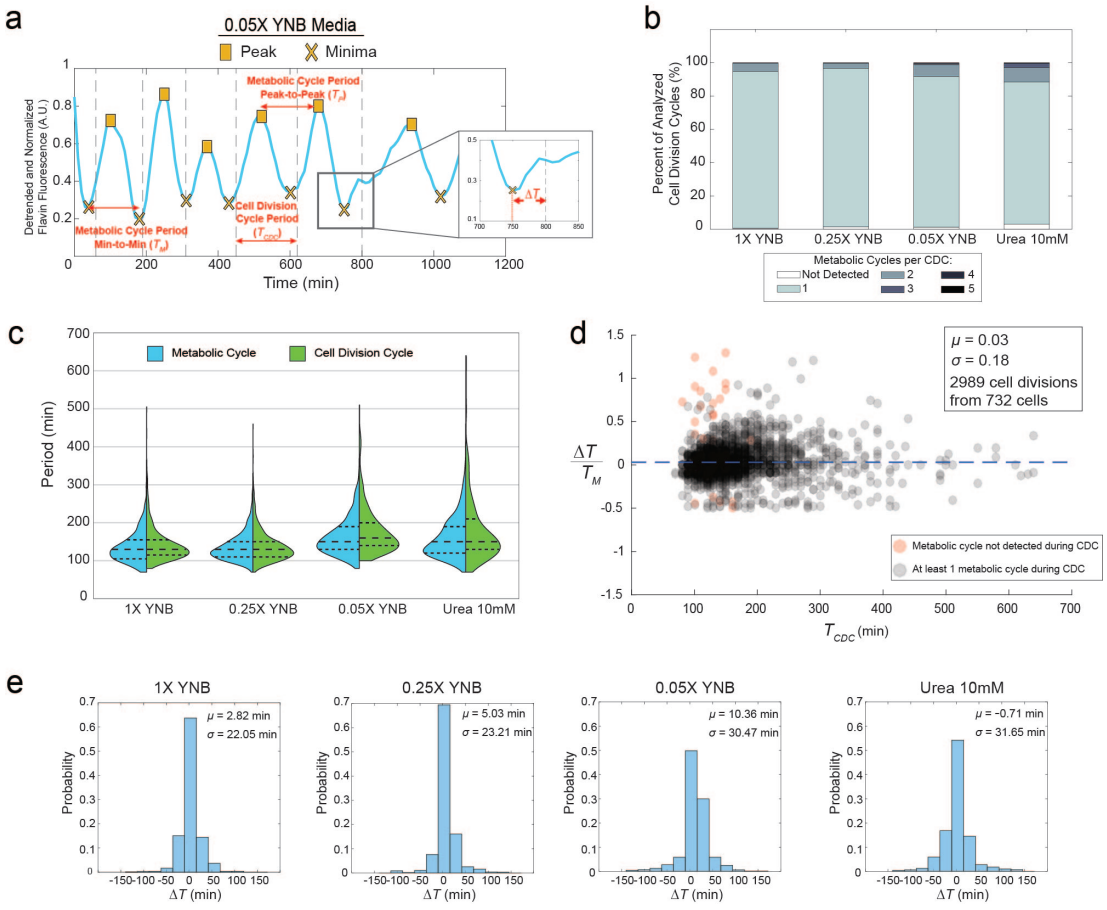

Figure 3.3: Phase synchronization between the metabolic cycle and CDC in different nutrient environments. (a) Summary of the information collected from each single-cell. Across four media conditions we recorded the peaks and troughs (yellow squares and 'X' marks respectively) of normalized and detrended metabolic cycles, the separation of the mother and daughter nuclei (black dotted lines), and the time difference between the metabolic cycle trough nearest to each mother-daughter nuclear separation event (ΔT). Thus for each condition we could quantify the metabolic cycle period (both the peak-to-peak (T_P) and min-to-min (T_M) period), the CDC period and the coupling or lag between the metabolic cycle and CDC. (b) Number of observed metabolic cycles occurring during each cell division. (c) Split violin plots of the distributions of peak-to-peak periods (T_P) of the metabolic cycle and the CDC period (T_{CDC}) for cells in each nutrient condition. Dotted lines represent the quartiles of the distributions. (d) Single cell data of each ΔT scaled by the metabolic cycle period (min-to-min period T_M) versus the CDC period (T_{CDC}) shows that regardless of the length of the cell division cycle, division is completed near a metabolic cycle trough. Data collected from all four media conditions is displayed from a total of 2989 cell divisions, where μ is the mean and σ is the standard deviation. The dashed blue line at $\Delta T/T_M = 0$ is shown as a reference. (e) Distributions of the absolute lag time ΔT for each media condition. The number of cells analyzed for the 1X YNB, 0.25X YNB, 0.05X YNB and 10 mM urea conditions are as follows: 156 cells, 225 cells, 175 cells and 176 cells.

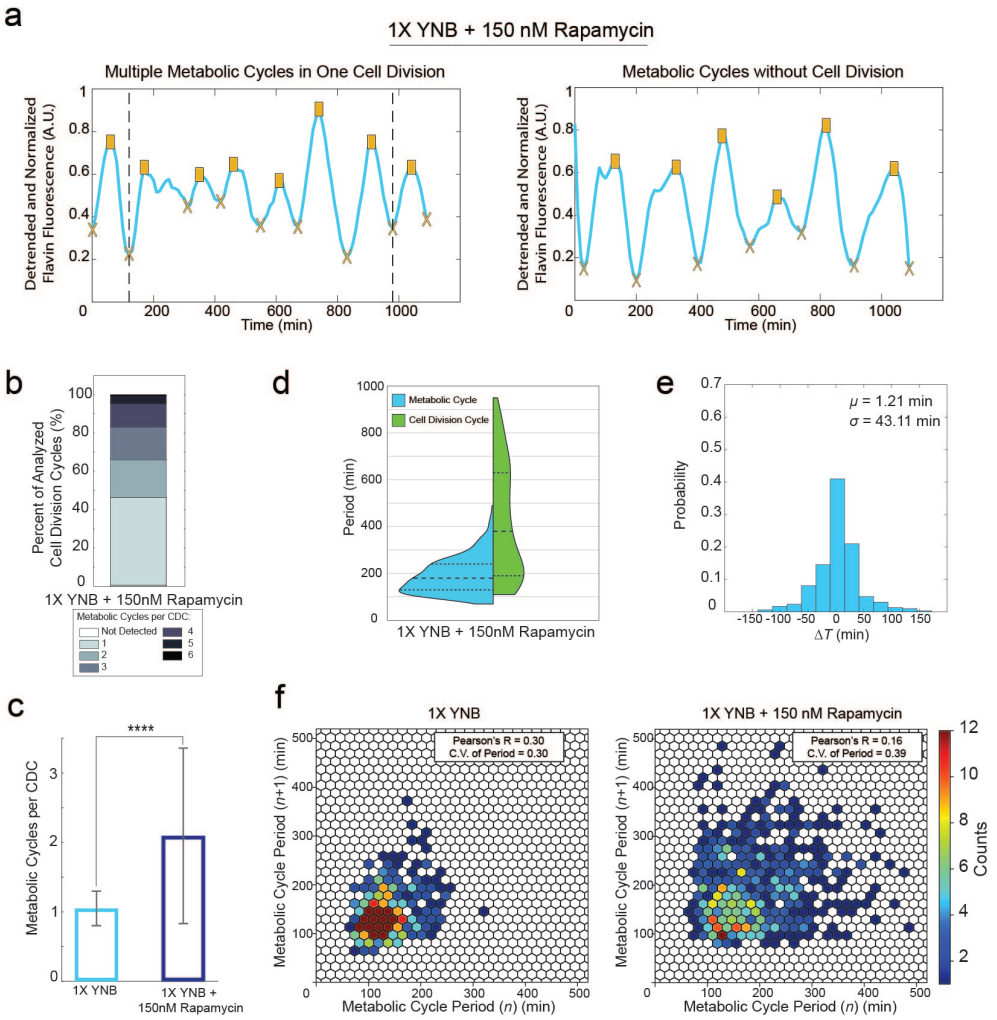

Figure 3.4: Rapamycin alters the periodicity of the metabolic cycle and its phase synchronization with the CDC.(a) Example of metabolic cycles in cells treated with 150 nM rapamycin. There was an increased occurrence of multiple metabolic cycles occurring during each cell cycle (left panel). Further some cells displayed metabolic cycles in the absence of complete cell cycle progression (right panel). (b) Number of observed metabolic cycles occurring during each cell division cycle. Metabolic cycles not occurring during a division event were not included here. (**C**) Comparison of the number of metabolic cycles during each CDC in 1X YNB media and 1X YNB media with 150 nM rapamycin, showing a significant increase for the rapamycin treated cells (Kolmogorov-Smirnov test; $****P < 0.0001$, $P = 2.89 \times 10^{-25}$). Error bars are the standard deviation. (d) Split violin plot of the metabolic cycle (T_P) and CDC periods for rapamycin treated cells. The number of cells used to calculate YMC periods was 180 and the number used to calculate CDC periods (cells that divided at least twice) was 85. (e) Distribution of ΔT values for rapamycin treated cells that divided at least once during the experiment ($n = 151$). ΔT is defined the same as in Fig.3.3. (f) Hexagonal binning plot of each metabolic cycle period n versus the next period n+1. Colors correspond to number of values within each hexagon.

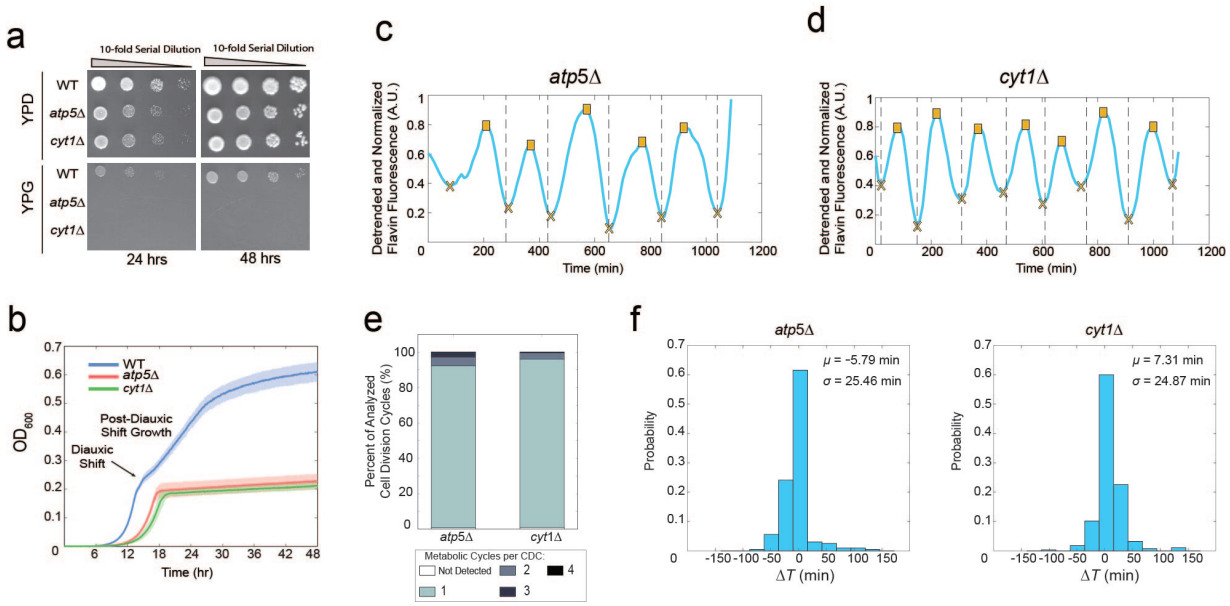

Figure 3.5: Metabolic cycles continue in respiratory deficient mutants. (a) The *atp5*Δ and *cyt1*Δ mutants do not exhibit noticeable growth on YPG plates containing the non-fermentable carbon source glycerol. Cells growing on YPD served as a control. (b) Growth curves demonstrating that cultures of *atp5*Δ and *cyt1*Δ strains display no post-diauxic shift growth, indicating an inability to conduct respiratory metabolism. Solid lines and shaded regions represent the means and standard deviations, respectively, from four replicates for each strain. (c) Representative metabolic cycling in the *atp5*Δ strain. (d) Representative metabolic cycling in the *cyt1*Δ strain. (e) The number of metabolic cycles occurring per cycle division cycle for each strain (n = 54 cells for *atp5*Δ, and n = 52 cells for *cyt1*Δ). (f) Distributions of ΔT, the time between the metabolic cycle trough and separation of the mother and daughter nuclei for each strain.

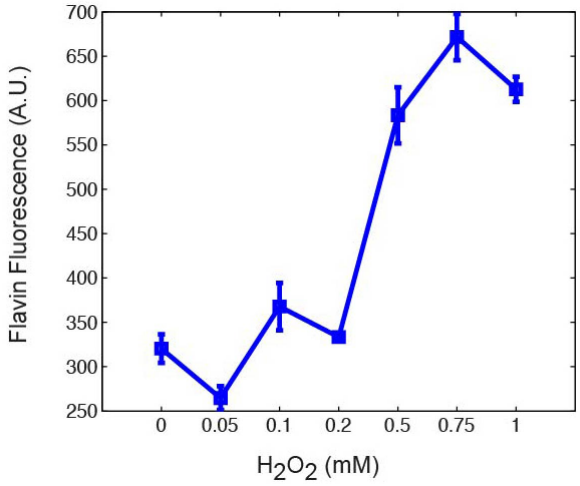

Figure 3.6: Flavin oscillations in single yeast cells. Dose response of flavin fluorescence intensity over a range of H_2O_2 concentrations. Cells were treated with various concentrations of hydrogen peroxide for 20 minutes after reaching log phase in 1X YNB. Cells were imaged for flavin fluorescence under coverslips. The number of cells collected for each condition is as follows: n = 41 (0 mM), n = 64 (0.05mM), n = 61 (0.1 mM), n = 106 (0.2 mM), n = 30 (0.5 mM), n = 38 (0.75 mM) and n = 101 (1 mM). Error bars are standard error of the mean of measurements from individual cells.

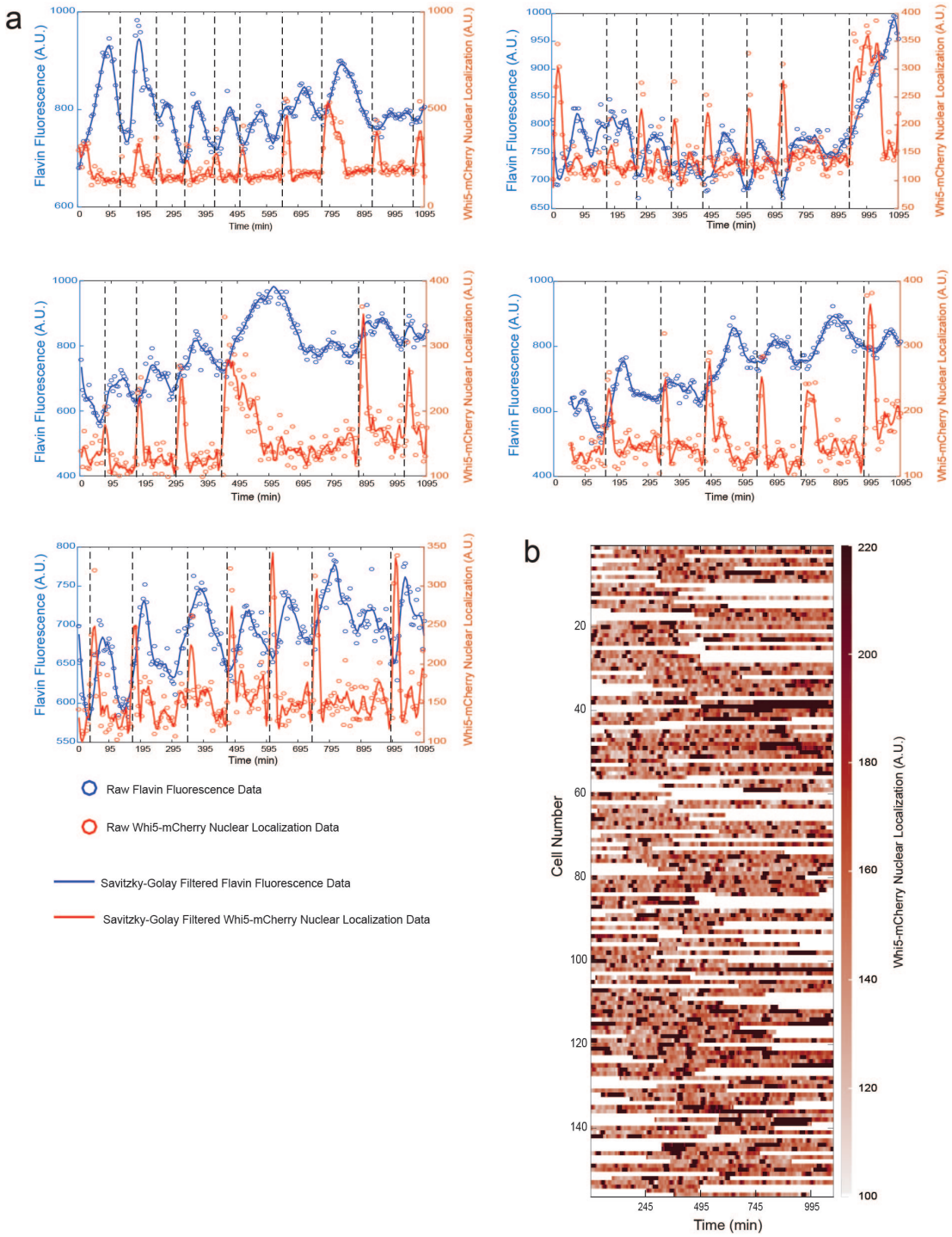

Figure 3.7: Trajectories of flavin fluorescence and Whi5-mCherry reporter.(a) Sample trajectories of flavin fluorescence and the Whi5-mCherry nuclear localization signal. (b) Heatmap of Whi5-mCherry nuclear localization in all cells, demonstrating lack of cell division cycle synchrony. The black dotted lines represent separation of the mother and daughter nuclei (from Nhp6a-iRFP reporter).

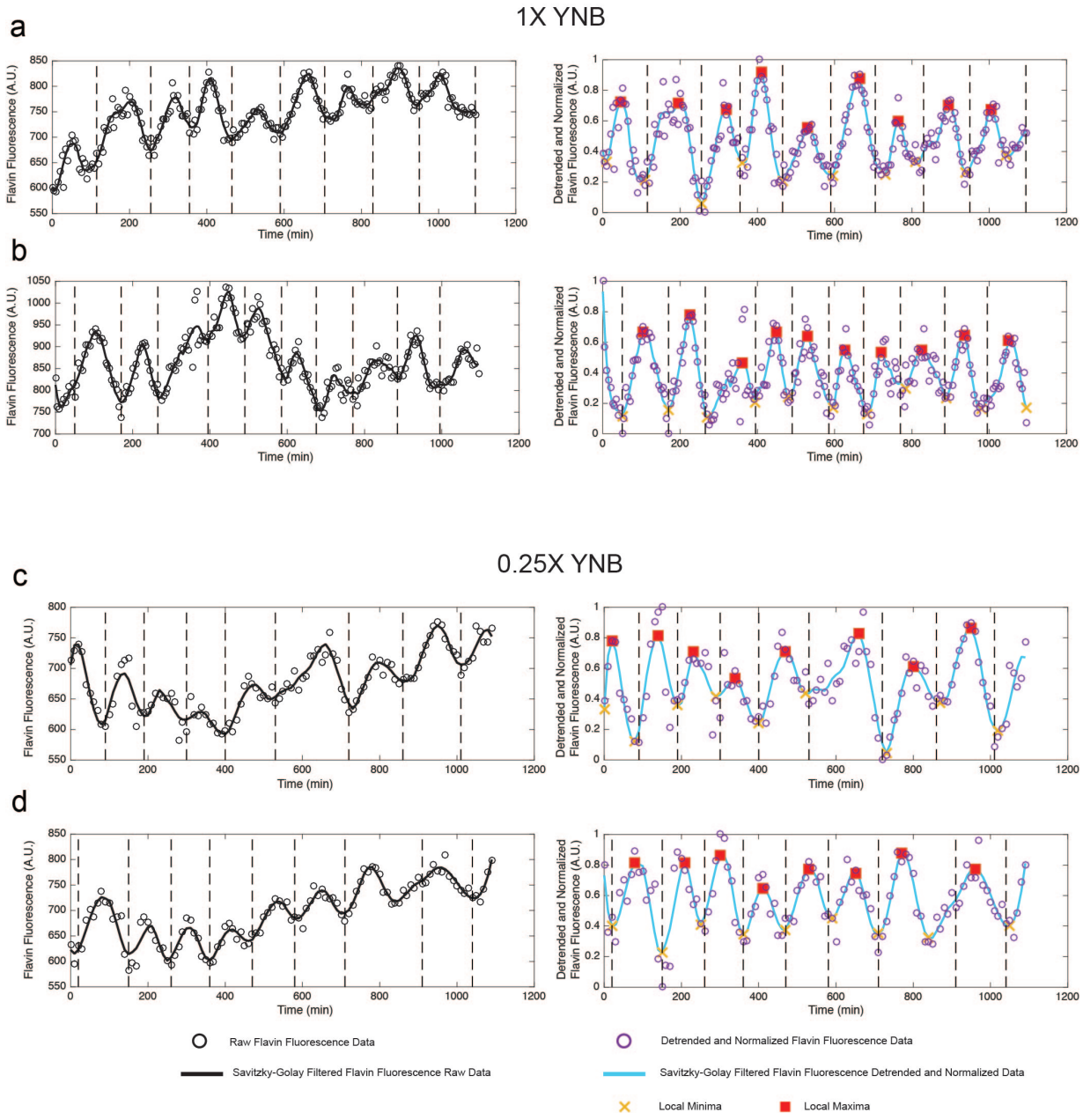

Figure 3.8: Metabolic cycles in 1X and 0.25X YNB concentrations. (a) Sample trajectory for 1X YNB media. (b) Additional sample trajectory for 1X YNB media. (c) Sample trajectory for 0.25X YNB. (d) Additional sample trajectory for 0.25X YNB media. For all detrended and normalized trajectories the red squares represent recorded local YMC peaks, the yellow 'X' marks local metabolic cycle troughs and the black dotted lines represent separation of the mother and daughter nuclei as determined by the Nhp6a-iRFP reporter. In all panels, the raw data and Savitzky-Golay filtered data are shown on the left and the corresponding detrended and normalized trajectory and filtered trajectory are shown on the right.

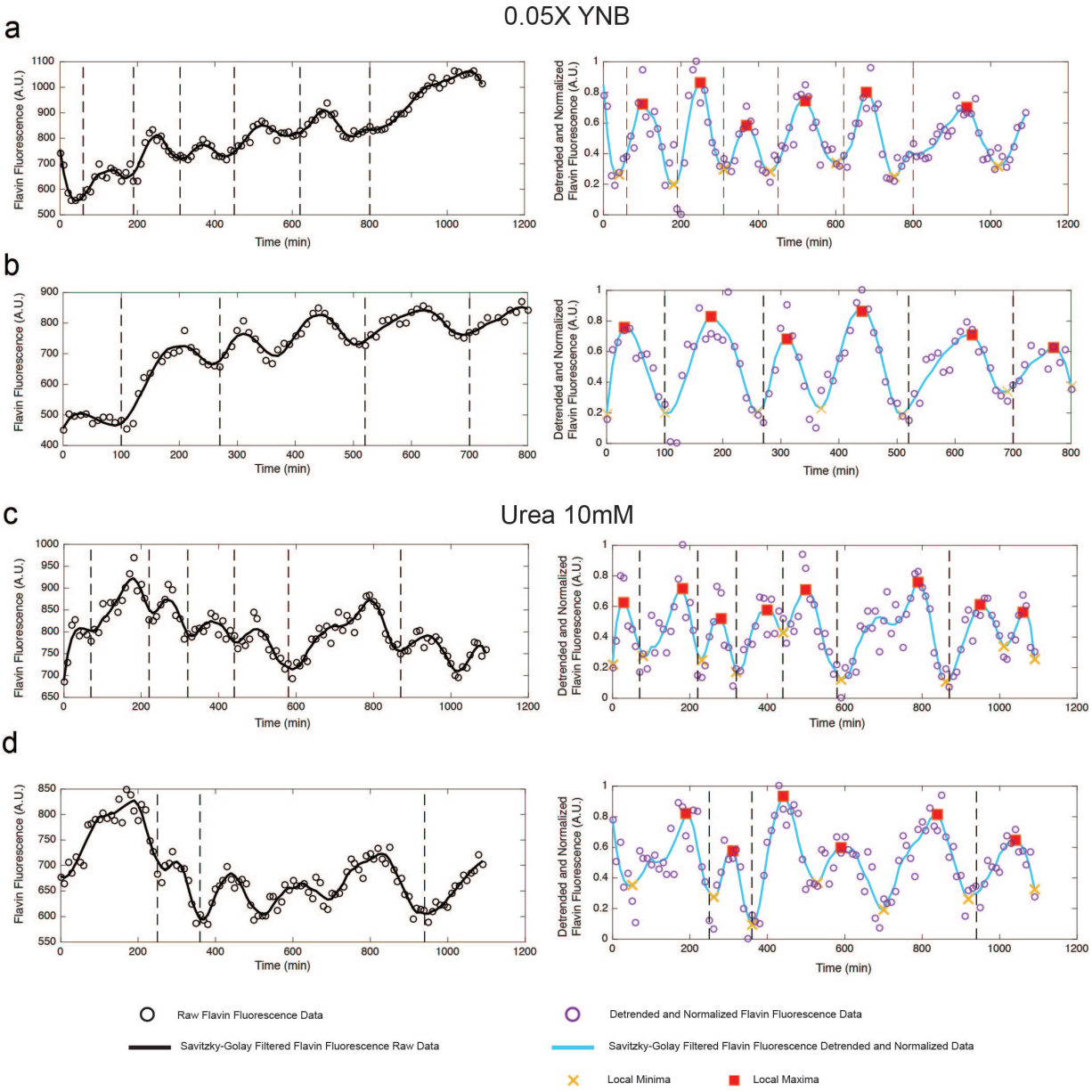

Figure 3.9: Metabolic cycles in 0.05X YNB and 1X YNB with 10mM urea as the nitrogen source. (a) Sample trajectory for 0.05X YNB media. (b) Additional sample trajectory for 0.05X YNB media. (c) Sample trajectory for 1X YNB with 10mM urea. (d) Additional sample trajectory for 1X YNB with 10mM urea. As in Fig. S4, raw data and Savitzky-Golay filtered data are shown on the left and the corresponding detrended and normalized trajectory and filtered trajectory are shown on the right.

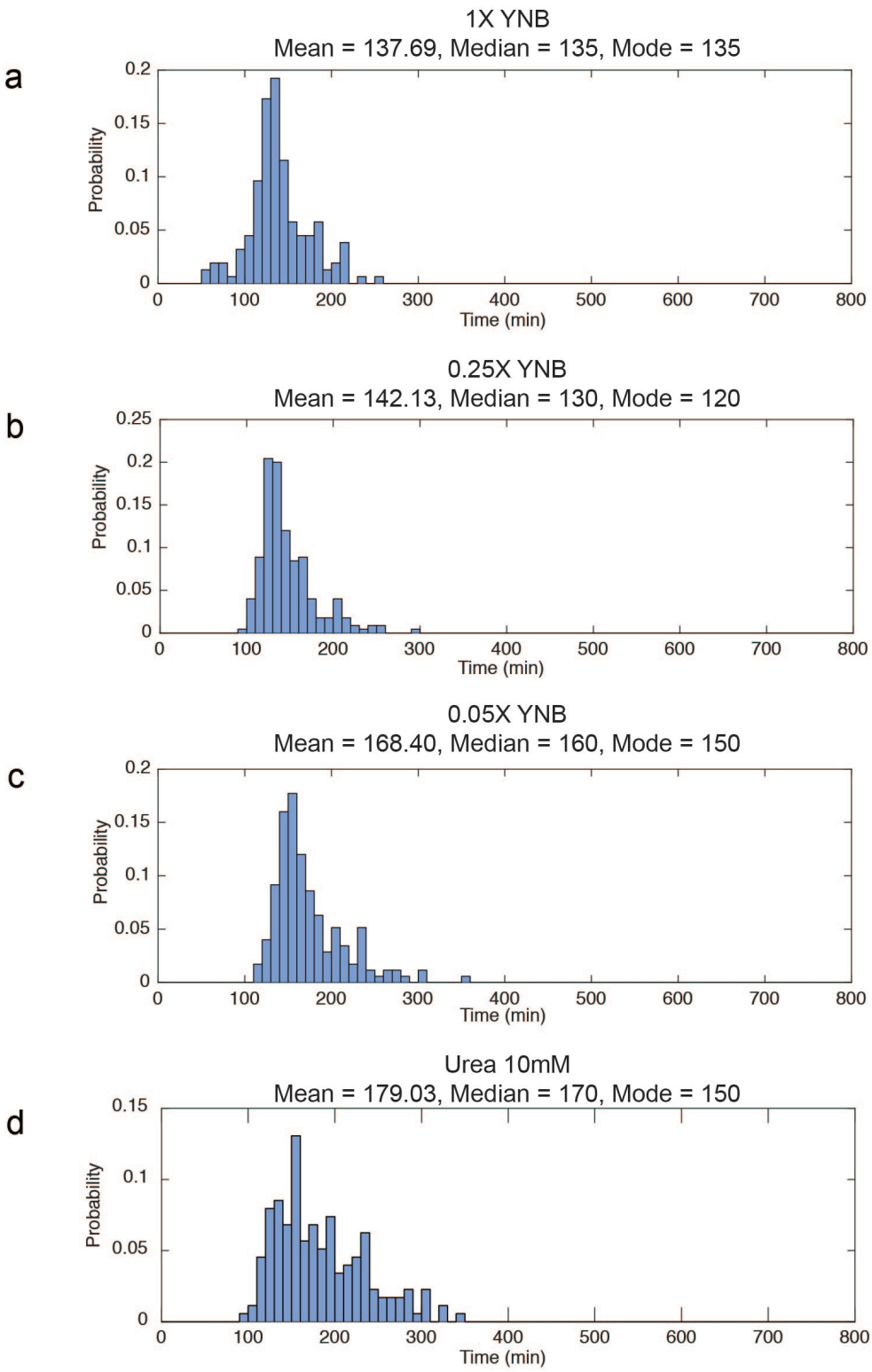

Figure 3.10: Autocorrelation analysis of metabolic cycles. Summaries of the location of the first autocorrelation peak for each cell for the (a) 1X YNB, (b) 0.25X YNB and (c) 0.05X YNB (d) 1X YNB with 10mM urea media conditions.

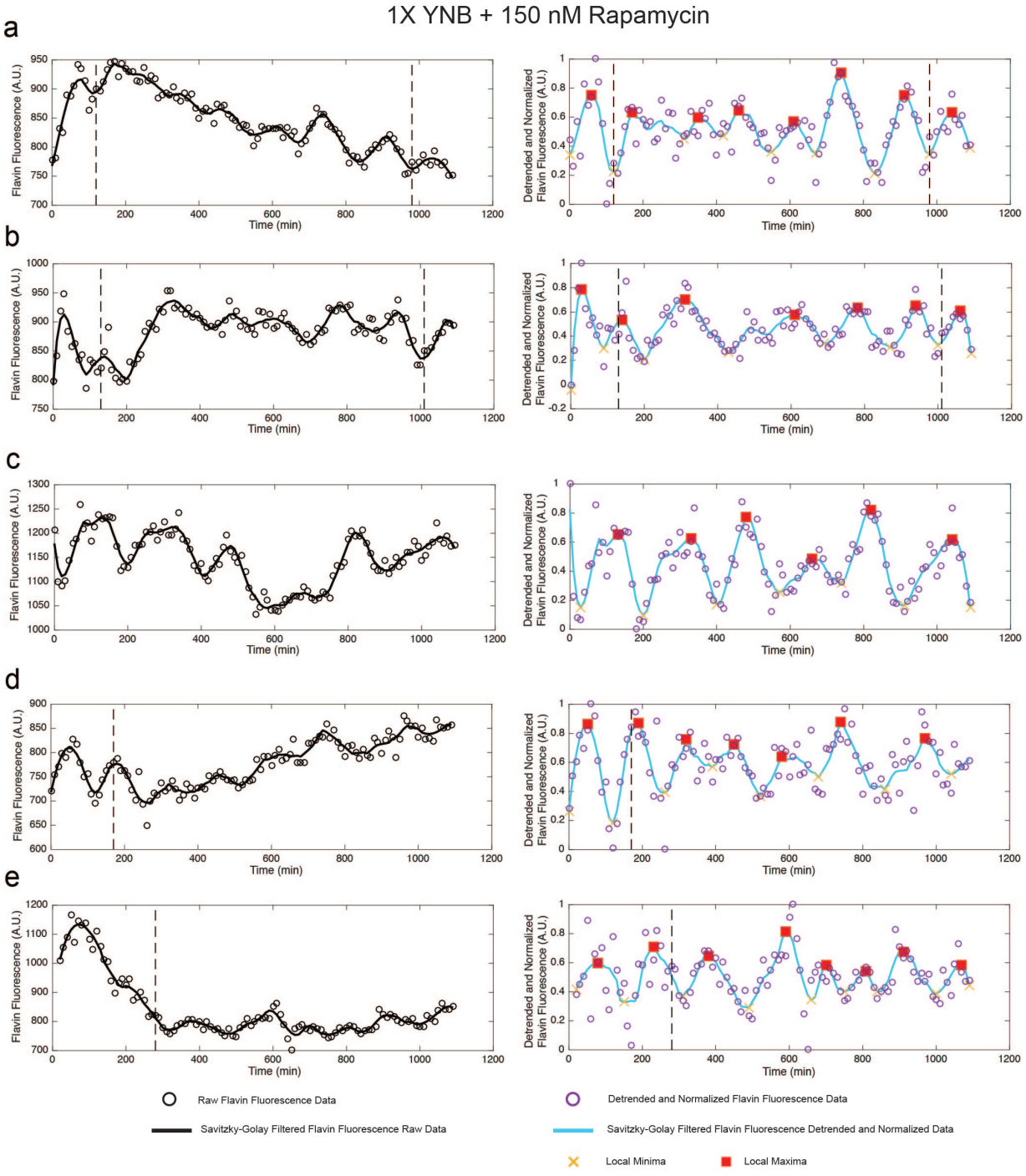

Figure 3.11: Metabolic cycles in 1X YNB with 150nM rapamycin. (a-e) Sample trajectories for 1X YNB with 150nM rapamycin. As in Fig. S4 and Fig. S5, raw data and Savitzky-Golay filtered data are shown on the left and the corresponding detrended and normalized trajectory and filtered trajectory are shown on the right.

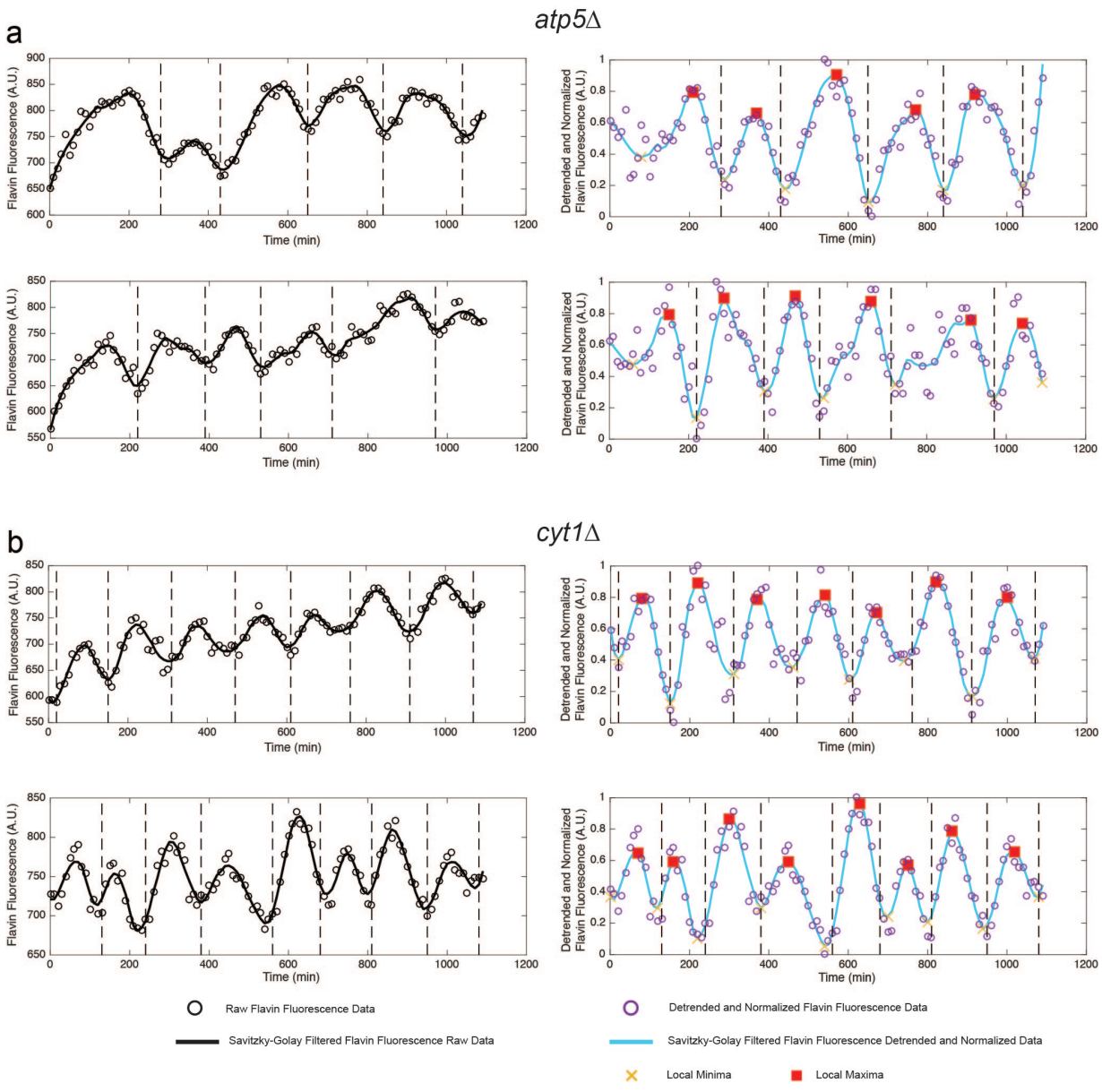

Figure 3.12: Metabolic cycles in the *atp5*Δ and *cyt1*Δ mutants. (a) Sample trajectories for *atp5*Δ. (b) Sample trajectories for *cyt1*Δ. Raw data and Savitzky-Golay filtered data are shown on the left and the corresponding detrended and normalized trajectory and filtered trajectory is shown on the right.

3.5 Acknowledgements

This chapter contains material that was originally published as Baumgartner, B.L.*, O'Laughlin, R.*, Jin, M.*, Tsimring, L.S., Hao, N. and Hasty, J., 2018. Flavin-based metabolic cycles are integral features of growth and division in single yeast cells. *Scientific Reports*, 8(1), pp.1-10. (*equal contribution). Reproduction of this work was granted by Springer Nature under the Creative Commons Attribution 4.0 International License (https://creativecommons.org/licenses/by/4.0/). The dissertation author, Richard O'Laughlin, was a primary investigator and author of this work.

Chapter 4

Single-cell analysis of chromatin silencing dynamics at the rDNA locus during replicative aging in yeast

4.1 Introduction

Cellular aging is generally driven by the accumulation of genetic and cellular damage [138, 139]. Although much progress has been made in identifying molecular factors that influence life span, what remains sorely missing is an understanding of how these factors interact and change dynamically during the aging process. This is in part because aging is a complex process wherein isogenic cells have various intrinsic causes of aging and widely different rates of aging. As a result, static population-based approaches could be insufficient to fully reveal sophisticated dynamic changes during aging. Recent developments in single-cell analyses to unravel the interplay of cellular dynamics and variability hold the promise to answer that challenge [140–142]. Here we chose the replicative aging of yeast *S. cerevisiae* as a model and exploited quantitative biology technologies to study the dynamics of molecular processes that control aging at the single-cell

level.

4.2 Tracking rDNA silencing dynamics in the yeast aging microfluidic device

Replicative aging of yeast is measured as the number of daughter cells produced before the death of a mother cell [51]. The conventional method for studying yeast aging requires laborious manual separation of daughter cells from mother cells after each division and does not allow tracking of molecular process over multiple generations during aging [143].Recent advances in microfluidics technology have automated cell separation and enabled continuous single-cell measurements during aging [54, 55, 63–67]. Building upon these efforts, we developed a new microfluidic aging device. As discussed in Chapter 2, the device traps mother cells at the bottom of finger-shaped chambers, allowing them to bud continuously, while daughter cells are removed via a waste port. Each chamber also has a small opening at the bottom, allowing daughter removal when mother cells switch budding direction. The long trapping chambers allow tracking of each daughter cell during its first several divisions, useful for studying age-related daughter morphologies. Furthermore, the device can deliver precise environmental waveforms to culture chambers.

Genome instability has been considered a significant causal factor of cell aging [138, 144]. A major contributor to the maintenance of genome stability is chromatin silencing, which causes a locally inaccessible heterochromatin structure that suppresses transcription, recombination and DNA damage. The heterochromatic regions in yeast include the silent mating-type (*HM*) loci, rDNA and subtelomeric regions [145]. Among them, the rDNA region on chromosome XII consists of approximately 100-200 tandem repeats and is a particularly fragile genomic site, the stability of which closely connects to the RLS [146–148]. Previous studies showed that silencing loss induced by chemical or genetic perturbatinos leads to increased recombination at the rDNA

region and shorter life spans [86, 149]. However, the dynamic changes of rDNA silencing during cell aging remain largely unknown. To measure chromatin silencing in single aging cells, we constructed a strain with a fluorescent reporter gene under the control of a constitutive TDH3 promoter at a non-transcribed spacer region (NTS1) of rDNA. Because expression of the reporter gene is repressed by silencing, decreased fluorescence indicates enhanced silencing, whereas increased fluorescence indicates reduced silencing [150, 151] (Fig. 4.1a, b).

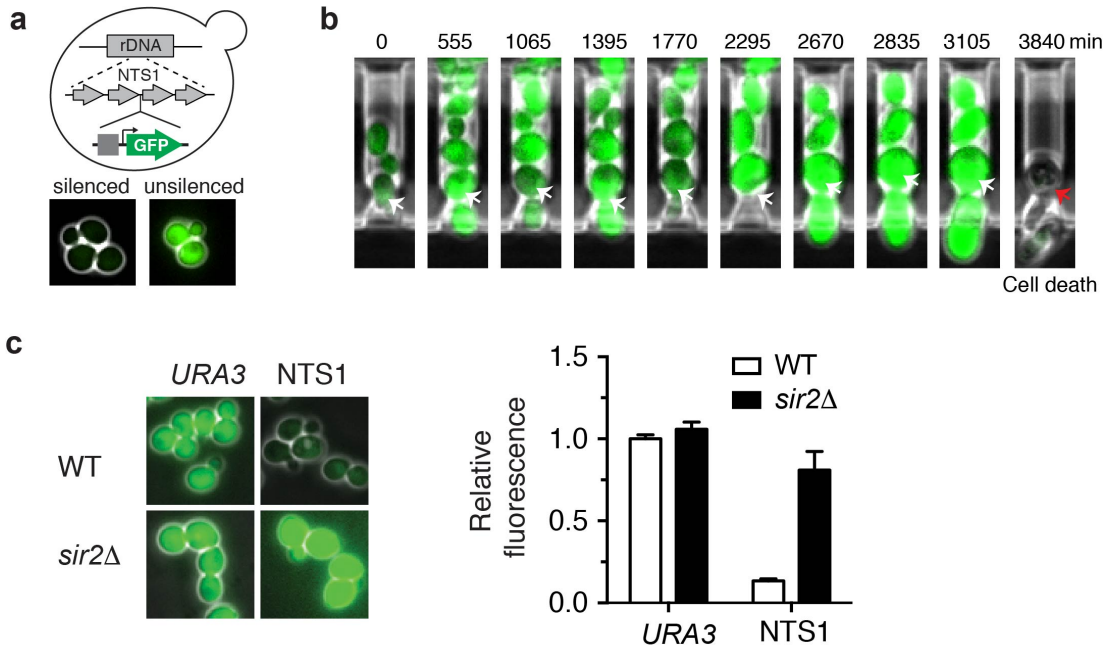

Figure 4.1: Tracking the dynamics of chromatin silencing in single aging cells using a microfluidic device. (a) Illustrative schematic of the reporter for chromatin silencing. A GFP reporter under a strong constitutive promoter (TDH3) is inserted at an NTS1 repeat within the rDNA. Chromatin silencing at the rDNA is reflected by fluorescence intensity: low, silenced; high, decreased silencing. (b) Time-lapse images of a single cell trap throughout an entire life span. Arrows point to the mother cell. (c) Validation of the reporter. Left: Representative images of WT or *sir2*Δ cells with the fluorescence reporter gene inserted at URA3, or NTS1 at the rDNA. Right: Average fluorescence intensities quantified from different strains in the left panel and normalized to the reporter level at URA3 in WT cells.

We observed that cells with the rDNA reporter gene exhibit weak fluorescence; in contrast, cells carrying the same reporter at the URA3 locus, which is not subject to silencing, show very high fluorescence. In addition, deletion of SIR2, which is required for rDNA silencing [145],

yields significantly increased reporter expression at the rDNA, but not at URA3 (Fig. 4.1c).

Using the microfluidic device and the reporter, we tracked the dynamics of rDNA silencing throughout the entire lifespans of individual cells (Fig. 4.2). We found intermittent fluorescence increases in most cells, indicating sporadic silencing loss during aging. About half (about 46%) of the cells, during the later stages of aging, continuously produced daughter cells with a characteristic elongated morphology until death (Fig. 4.2a, blue arrows). These cells also exhibited a sustained and dramatic increase in fluorescence, indicating sustained loss of silencing in aged cells (Fig. 4.2a, color map). In contrast, the other half of the cells, at later phases of their life spans, continuously produced small round daughter cells (Fig. 4.2b, blue arrows) with sharply increased cell cycle length.These cells had a shorter average life span than the other aging type (with a mean RLS of 18 compared to 24) and did not show sustained silencing loss during aging (Fig. 4.2b, color map). These two distinct types of age-associated phenotypic changes suggest different molecular causes of aging in isogenic cells [54, 55, 66]. Previous studies showed that the aging phenotype with small round daughters could be related to an age-dependent mitochondrial dysfunction [55, 64], but the molecular mechanisms underlying the other aging type characterized by elongated daughters remain largely unclear. In support of this, young mother cells can also sporadically produce a few elongated daughters, the occurrence of which correlates with the transient silencing loss during the early phase of their life spans (Fig. 4.2c). In addition, cross-correlation analysis revealed an approximately 140 minute time delay between the occurence of silencing loss in mother cells and the production of elongated daughters (Fig. 4.2d). This temporal order suggested a potential causal relationship between silencing loss and the elongated daughter phenotype. In this work, we focused our analysis on the dynamics and heterogeneity of the type of aging process with sustained silencing loss and elongated daughters.

To exclude the possibility that the observed fluorescence patterns are caused by age-associated global effects on gene expression [152], we simultaneously monitored two distinguishable fluorescent reporters inserted at the rDNA and at URA3. Whereas the rDNA reporter showed

early sporadic and late sustained induction of fluorescence, the reporter at URA3 exhibited relatively constant fluorescence during aging (Fig. 4.3a). To confirm that the observed silencing dynamics are not specific to the NTS1 region, we measured the reporter response at another non-transcribed spacer region of rDNA (NTS2) and observed similar dynamic patterns as those found at NTS1 (Fig. 4.3b). Together, these results validate the reporter responses during aging. We observed very rare events of recombination or extrachromosomal rDNA circles of the reporter gene, which can be easily distinguished from silencing loss in single-cell time traces Fig. 4.3c). We have excluded those cells from analysis.

4.3 Quantitative analysis of rDNA silencing dynamics

To evaluate how dynamic patterns of chromatin silencing influence cell aging, we quantitatively analyzed the time traces of silencing loss in individual cells producing elongated daughters before death. With very diverse lifespans ranging from 9 to 48 generations, all the cells show sustained silencing loss toward later stages of aging. Most cells also exhibit early sporadic waves of silencing loss, each of which spans multiple cell divisions (Fig. 4.4a). This unprecedented long-wavelength dynamics is distinct from most previously characterized molecular pulses, which are on timescales faster than or close to a cell cycle [142]. We further dissected each single-cell time trace into two phases: an early phase with sporadic silencing loss and a late phase with sustained silencing loss (Fig. 4.4b, "Intermittent Phase" and "Sustained Phase"). The length of Intermittent Phase (or the number of silencing waves) is highly variable among cells (Coefficient of Variation – CV: 0.63; Fig. 4.6) correlates closely with final life span, suggesting the longevity of a cell is largely determined by the time it stays in this phase (Fig. 4.4c, left). Long-lived cells generally have a longer Intermittent Phase and produce more silencing silencing waves than short-lived cells (Fig. 4.4a, Fig. 4.6b and d). In contrast, the length of Sustained Phase is more uniform among cells (CV: 0.29; Fig. 4.6a) and shows little relationship with life span, suggesting

sustained silencing loss defines cell death within a relatively constant period of time (Fig. 4.4c, right). We further quantified the rise time of each fluorescence increase in single aging cells (the duration of silencing loss; Fig. 4.4b, t1 and t2) and found a significant difference between the durations of early sporadic and later sustained silencing loss: a sporadic silencing loss on average lasts for about 300 minutes, whereas sustained silencing loss lasts for about 1200 minutes until death (Fig. 4.4d). Moreover, sporadic waves of silencing loss show modest effects on the basal silencing level during aging, as indicated by the trough levels of silencing loss pulses in single-cell time traces (Fig. 4.6b and c), yet do not contribute additively onto sustained silencing loss to inducing cell death (Fig. 4.6e).

Together, our analyses reveal that cells undergo spontaneous silencing loss during aging. The early phase of aging features a reversible process, in which cells can effectively reestablish silencing and produce non-detrimental short waves of silencing loss. The late phase is irreversible: aged cells cannot re-establish silencing [153], resulting in sustained silencing loss and death. Individual cells might have different intrinsic capacities to maintain the reversible phase and thereby the ultimate life span.

4.4 A phenomenological model of rDNA silencing loss and cell aging

To provide a quantitative framework for understanding aging dynamics, we developed a simple phenomenological model. The model postulates that an aging cell can be in one of the two states: state 0 is the silencing state in which it produces normal daughters, and state 1 is the loss of silencing state with elongated daughters (Fig. 4.5a). The transitions between the states are characterized by transition probabilities p_{01} and p_{10} that depend linearly on the cell age (Fig. 4.5b). In the silenced state (state 0), D is set to zero. We fit the model only using the experimental data on phenotypic changes and simulated this model stochastically. The model reproduced

the main statistical properties of age-dependent phenotypic changes and RLS remarkably well (Fig. 4.5c–f). We also generated individual cell state trajectories (Fig. 4.5g) that qualitatively and quantitatively reproduce the data in Fig. 4.2a. To predict how silencing dynamics influence aging, we further simulated the effects of an induced silencing loss. Whereas a short pulse of silencing loss does not affect life span, a sustained silencing loss dramatically shortens life span (Fig. 4.5h and i). To test these predictions, we set out to modify silencing dynamics using genetic or chemical perturbations.

4.5 Perturbations of rDNA silencing dynamics

Chromatin silencing at the rDNA is primarily mediated by the lysine deacetylase Sir2, encoded by the best-studied longevity gene to date, which is conserved from bacteria to humans [145]. To examine the role of Sir2 in regulating silencing dynamics, we monitored the aging process of sir2Δ cells. We observed that *sir2*Δ cells do not exhibit sporadic silencing loss; instead, most cells show sustained silencing loss throughout their life spans (Fig. 4.6a), indicating that the intermittent silencing dynamics is dependent on Sir2-mediated silencing reestablishment. Most (70%) *sir2*Δ cells continuously produce elongated daughters until their death, in accordance with the observed correlation between silencing loss and elongated daughters. Furthermore, in *sir2*Δ cells, sustained silencing loss leads to cell death within a relatively uniform time frame, strikingly resembling the Sustained Phase in WT cells (Fig. 4.6a, red dashed line). These results suggest Sir2 promotes longevity by generating intermittent silencing dynamics and delaying entry into the Sustained Phase. We also examined *sgf73*Δ, a mutant with an extended longevity [154](28), and observed intermittent silencing dynamics during aging and elongated daughters at the late phase of aging. This long-lived mutant shows more silencing loss pulses than WT, consistent with the possibility that the intermittent silencing dynamics promotes longevity (Fig. 4.8).

To further test predictions of the model and examine the causative roles of silencing

dynamics on aging, we exposed cells to nicotinamide (NAM), an inhibitor of Sir2 (29), to chemically disrupt silencing with physiologically relevant durations. In response to a 1,000-min NAM input mimicking the Sustained Phase, the majority of cells cannot recover from silencing loss (Fig. 4.6b). All (100%) of the treated cells, although young, continuously produce elongated daughters and die within a similar time frame to sustained silencing loss in sir2 mutant or WT cells (Fig. 4.6b). The cells also show an elevated DNA damage response, as reported by the induction of RNR3 (30, 31) (Fig. 4.6b, Inset), and have a significantly shortened life span (mean RLS, 12), comparable to that of sir2 mutants. These results suggested that sustained silencing loss causes the elongated daughter phenotype and accelerates cell death in young cells. In contrast, in response to a 240-min NAM input, mimicking the sporadic silencing loss, most cells exhibit a synchronized silencing loss followed by effective silencing reestablishment on the removal of NAM (Fig. 4.6c). This short-term silencing loss does not induce the DNA damage response (Fig. 4.6c, Inset) and does not affect life span, in accord with the sporadic silencing loss in the Intermittent Phase of naturally aging cells. These perturbation experiments validate the model's predictions and confirm that a prolonged duration of silencing loss triggers an irreversible process sufficient to induce cell death, whereas short-term silencing loss is fully reversible and does not promote aging or death.

Finally, we considered the role of the intermittent pattern of silencing, as opposed to continuous chromatin silencing. To this end, we used nicotinic acid (NA), an activator of Sir2 [155], to prevent sporadic silencing loss in aging cells. As shown in Fig. 4.6d, most cells show continuous silencing with few sporadic losses of silencing. The repression of silencing loss during aging results in the absence of the elongated daughter phenotype in the majority (about 98%) of cells. Importantly, this sustained chromatin silencing also results in significantly shortened life span (mean RLS, 11), suggesting constant chromatin silencing can activate a different aging or death pathway. Furthermore, we confirmed that the effects of NA on life span are not likely a result of direct cellular toxicity (Fig. 4.9), but are instead primarily mediated

through Sir2 (Fig. 4.10). Our results suggest the intriguing possibility that chromatin silencing may be a double-edged sword with both anti-aging and pro-aging functions, probably depending on target genomic regions. Whereas sustained rDNA silencing loss increases heterochromatin instability, sustained chromatin silencing may repress genes that benefit longevity; either state would accelerate cell aging and death. The intermittent silencing dynamics driven by Sir2 allow the cell to periodically alternate between the two states, avoiding a prolonged duration in either state and maintaining a time-based balance important for longevity.

4.6 Discussion

Further analysis will continue to identify downstream targets that mediate the negative effects of sustained silencing on life span. For example, potential candidates include genes in other heterochromatic regions, such as subtelomeric genes that encode metabolic enzymes or have mitochondrial functions [158], or Sir2-repressed genes with prolongevity functions [159], or critical processes influenced by rDNA transcription, such as ribosomal biogenesis, a potential regulator of yeast aging [78, 160] . Interestingly, a recent study [133] demonstrated that aggregation of a cell-cycle regulator, but not the previously reported loss of silencing at HM loci [79], causes sterility in old yeast cells. This work, together with our findings here, suggests chromatin silencing at various genomic regions might undergo different age-dependent changes, probably because of their specific silencing complexes. For example, whereas the silencing at HM loci is regulated by a protein complex containing Sir2, Sir3, and Sir4 [161], a different complex containing Sir2, Net1, Cdc14, and Nan1 is required for the silencing at the rDNA [162, 163]. Furthermore, it has been shown that rDNA and HM silencing have different sensitivities to NAM or genetic perturbations [164–166], implying different regulatory modes at these loci. We anticipate that further systems-level analysis will enable a more comprehensive understanding of chromatin regulation during aging. Another interesting question for future investigation is the fate

of elongated daughters. One possibility is that the production of these abnormal daughters may serve as a rescue strategy to alleviate damage accumulation in mother cells. Future technological advances that allow life span tracking of selected daughter cells would enable us to examine the silencing dynamics, life span, and aging type decision of these elongated daughters and their daughters.

Dynamics-based regulation is an emerging theme in biology, the role of which has been increasingly appreciated in many biological processes across a wide range of organisms [26,136,140,141,167–169]. Our analysis here uncovered the significant role of silencing dynamics in cellular aging and opened the possibility of designing temporally controlled perturbations to extend life span. For example, although constant NA exposure shortens life span, it might be possible to design dynamic regimes of NA treatment to specifically prevent sustained silencing loss, and thereby delay aging. Given the observed single-cell heterogeneity in silencing and aging dynamics (Figs. 4.2 and 4.4), future efforts will focus on technologies that enable distinct real-time NA treatments to individual cells based on their silencing states.

4.7 Materials and Methods

4.7.1 Strains and plasmids construction

Standard methods for the growth, maintenance and transformation of yeast and bacteria and for manipulation of DNA were used throughout. The yeast strains used in this study were generated from BY4741 (MAT a his3Δ1 leu2Δ0 met15Δ0 ura3Δ0) strain background. Strain and plasmid information is provided in Tables 4.1 and 4.2. To make the nuclear reporter for single cells, a IRFP::KanMX fragment was PCR amplified and integrated into the C-terminus of NHP6a at the native locus by homolog recombination. To make sir2Δ mutants, a CgHIS3 [170] fragment was amplified to replace the SIR2 open reading frame by homolog recombination. Similarly, the SGF73 ORF was replaced with CgHIS3. The URA3 ORF is deleted in the BY4741 background.

To add a mutated URA3 gene (ura3-1) back to its native locus, a CgURA3 fragment [170] was amplified and inserted at URA3, then CgURA3 was replaced with a ura3-1 allele from the W303 strain. To make the NTS1 silencing reporter, a Xho1-NTS1-EcoRI fragment from pDM704 [171] was ligated into the pRS306 plasmid vector. A EcoRI-PTDH3-GFP-EagI fragment contains 680 bp of TDH3 promoter and GFP ORF was made by fusion PCR and then ligated into pRS306 and the plasmid pRS306 with Xho1-NTS1-EcoRI fragment to get plasmids NHB0206 and NHB0200. Plasmids NHB0213 and NHB0214 were constructed in the same way. The NTS2 fragment for plasmid NHB0214 was derived from plasmid pDM312 [171]. Yeast strains with rDNA silencing reporter were generated by transformation with NHB0200 cut with HindIII to integrate at NTS1, NHB0213 cut with HindIII to integrate at NTS1, NHB0214 cut with SmaI to integrate at NTS2, and NHB0206 cut with StuI to integrate at ura3-1. All transformations were performed with the lithium acetate method [172], and integration was confirmed by PCR.

Table 4.1: Strains used or constructed in this study.

NH0256	BY4741 MAT a his3Δ1 leu2Δ0 met15Δ0 ura3Δ0
NH0268	BY4741 MAT a his3Δ1 leu2Δ0 met15Δ0 ura3Δ0, NHP6a-iRFP-kanMX
NH0270	BY4741 MAT a his3Δ1 leu2Δ0 met15Δ0 ura3Δ0, RDN1::NTS1-P_{TDH3}-GFP, NHP6a-iRFP-kanMX
NH0273	BY4741 MAT a his3Δ1 leu2Δ0 met15Δ0, NHP6a-iRFP-kanMX, ura3Δ0::ura3-1
NH0277	BY4741 MAT a his3Δ1 leu2Δ0 met15Δ0 ura3Δ0, NHP6a-iRFP-kanMX, RDN1::NTS1-P_{TDH3}-GFP-URA3, sir2::HIS3
NH0321	BY4741 MAT a his3Δ1 leu2Δ0 met15Δ0 ura3Δ0, NHP6a-iRFP-kanMX, RDN1::NTS1-P_{TDH3}-GFP-URA3, RDN1::NTS2-P_{TDH3}-mCherry-LEU2
NH0322	BY4741 MAT a his3Δ1 leu2Δ0 met15Δ0 ura3Δ0, NHP6a-iRFP-kanMX, RDN1::NTS1-P_{TDH3}-mCherry-LEU2, ura3-1::URA3-P_{TDH3}-GFP
NH0465	BY4741 MAT a his3Δ1 leu2Δ0 met15Δ0 ura3Δ0, NHP6a-iRFP-kanMX, RDN1::NTS1-P_{TDH3}-GFP-URA3, sgf73::HIS3

Table 4.2: Plasmids constructed in this study.

NHB0200	pRS306_XhoI_NTS1_EcoRI_P_{GPD}-GFP_EagI
NHB0206	pRS306_EcoRI_P_{GPD}-GFP_EagI
NHB0213	pRS305_ApaI_NTS1-P_{GPD}-mCherry_SacI
NHB0214	pRS305_ApaI_NTS2-P_{GPD}-mCherry_SacI

4.7.2 Setting up a microfluidics experiment

Each microfluidic device was checked carefully before use to ensure no dust or broken features were present. Before setting up a microfluidics experiment, the device was vacuumed for 20 min.After vacuum, all of the inlets of the device were covered with 0.075% Tween 20 (Sigma-Aldrich Co.) for 5 min. The microfluidic device was placed on the stage of an inverted microscope with a 30C incubator system. Three media ports were connected to plastic tubing, which connected to 60 ml syringes with fresh SC medium containing 0.04% Tween-20. The height of all three medium syringes is about 20 inches above the stage. The waste port of the microfluidic device was connected to plastic tubing, which was set to stage height. Yeast cells were inoculated into 2 ml of synthetic complete medium (SC, 2% dextrose) and cultured overnight at 30C. 2 μl of saturated culture was diluted into 20 ml of fresh SC medium and grown at 30C overnight until it reached OD600nm of about 1.0. For loading, cells were diluted by 10-fold and transferred into a 60 ml syringe (Luer-Lok Tip, BD) connected to plastic tubing (TYGON, ID 0.020 IN, OD 0.060 IN, wall 0.020 IN). To load cells, the connected syringe on the middle port was replaced with a syringe filled with yeast culture. The height of the cell loading syringe is also about 20 inches above the stage. The flow of medium in the device was maintained by gravity and drove cells into traps. Most traps were filled with cells within 2-5 minutes, after which cell loading tubing was replaced with media supply tubing and syringe as above. Then the height of all medium tubing and the waste tubing were adjusted to make the height difference around 60 inches. Waste medium was collected in a 50 ml tube to measure flow rate, which was about 2.5 ml/day.

For experiments with media switching, left and right medium ports were connected to syringes with fresh SC medium containing 0.04% Tween-20 and the middle medium port was connected to a syringe containing medium with NA or NAM and 0.1 g/ml Atto 655 cy5 dye (Sigma 93711). The waste port of the microfluidic device was connected to plastic tubing set to a position about 20 inches below the stage. Before cell loading, the heights of syringes need to be calibrated for media switching. Syringes connected to the left and right medium ports were moved to the same height as the microscope stage and the syringe containing NA or NAM was moved to about 33 inches above the stage. To further calibrate the positions, the junction of all three media channels was imaged under the cy5 channel and the positions of syringes were adjusted to ensure the cell trapping region was fully filled with the NA or NAM medium. The position of all syringes were marked and used for NA or NAM during the experiment. To switch from the NA or NAM medium to SC medium, the left and right syringes were moved to about 33 inches above the stage and the middle syringes was moved to the same height as the stage. The positions of all syringes were further calibrated under the cy5 channel to ensure only SC medium went into the cell trapping region and then marked the positions of all syringes for the condition of no NA or NAM in the cell culture chamber. Cell loading was as for experiments without media switching. After cell loading, all syringes were moved to previously marked positions. The flow rate is about 2.5 ml/day. We note that Tween-20 is a non-ionic surfactant capable of coating the hydrophobic PDMS surface of microfluidic devices, thereby reducing protein interactions and cell friction on the PDMS [173, 174]. We have used Tween-20 or Tween-80 at very low concentrations in all the microfluidic experiments for more than 10 years on a variety of organisms including budding yeast [10, 11, 58, 175–178] without any adverse effects on cells. We have found that Tween-20 aids in preventing clogs and air bubbles from forming and therefore helps with the robustness and reproducibility of microfluidics experiments [23]. We have observed no difference in the cell doubling times in media with or without Tween-20 and have obtained lifespan measurements using our microfluidics setup that are comparable to values in the literature, confirming that

Tween-20 has no significant effect on lifespan or physiology.

4.7.3 Time-lapse microscopy

Time-lapse microscopy experiments were performed using a Nikon Ti-E inverted fluorescence microscope with Perfect Focus, coupled with an EMCCD camera (Andor iXon X3 DU897). The light source is a spectra X LED system. Images were taken using a CFI plan Apochromat Lambda DM 60X oil immersion objective (NA 1.40 WD 0.13MM). During experiments, the microfluidic device was taped to a customized device holder inserted onto the motorized stage (with Encoders). In all experiments, the microscope was programmed to acquire images for each fluorescence channel every 15 min for a total of 80 hours or more. The exposure and intensity setting for each channel were set as follows: Phase 50 ms, GFP 10 ms at 10% lamp intensity with an EM Gain of 50, mCherry 50 ms at 10% lamp intensity with an EM Gain of 200, and iRFP 300 ms at 15% lamp intensity with an EM Gain of 300. The EM Gain settings are within the linear range. We confirmed that this fluorescence imaging setting did not affect lifespan (See Chapter 2).

4.7.4 Quantification of single-cell traces

Fluorescence images were processed with a custom MATLAB code. Background of images from each channel was subtracted. Cell nuclei were identified by thresholding the iRFP images. Each image was evenly divided into 6 parts, each containing a single cell trap. The position of the dent in the cell trap was labeled. In each trap, the positions of all nuclei of each single cell were labeled. Mother cells are identified by comparing the positions of the dent and the positions of nuclei. Since the fluorescence reporter of rDNA silencing is evenly distributed inside the cell, nuclei of mother cells were further dilated to generate a mask to quantify the intensities of fluorescence reporters. The mean intensity value of the top 50% pixels of fluorescence reporter

is used as the intensity of the rDNA silencing reporter. All single-cell time traces were normalized by the mean reporter intensity of WT cells' 1st cell cycle and smoothed with local regression using weighted linear least squares and a 2nd degree polynomial model. The normalized and smoothed data were used for plotting of trajectories and density maps.

We also tested segmenting the whole cell using phase images and quantified the mean fluorescence intensities of the whole cell. The resulting time traces were similar to those obtained using nuclei segmentation and quantification as described above. Because nuclei segmentation and quantification is more robust than whole cell segmentation and allows us to identify and analyze more cells automatically, we used the former method for all imaging analysis.

Cell divisions of each mother cell were manually identified and counted at the time that the nuclei separated between mother and daughter cells. Cells were categorized based on their aging phenotypes, characterized by the morphologies of later daughters they produced. Mothers continually producing elongated daughters at the last few generations were categorized as "cells aging with elongated daughters", whereas mothers continually producing round daughters at the last few generations were categorized as "cells aging with rounded daughters." A small fraction of cells show abnormal morphologies even at the very beginning of the experiment and have a lifespan shorter than 5 generations. Those cells were excluded from analysis.

To identify the peaks and troughs of silencing loss pulses for aging cells, we first took the time derivative of the fluorescence trajectory of each single cell and then digitalized the curve by setting positive derivatives as 1 and negative derivatives as -1. The time points with the derivative transition from -1 to 1 were identified as "troughs" and the time points with the derivative transition from 1 to -1 were identified as "peaks". This identification process is illustrated in Fig. 4.6b.

During aging experiments, about 25% of mother cells escaped from chambers before their final death. The major reason for a mother cell to escape from the chamber is that when the mother produces a daughter cell toward the bottom of the chamber, depending on the bud

position, occasionally the daughter cell will not go through the small opening at the bottom of the chamber. Instead, the daughter will stay in the chamber and push the mother out. We observed that the times that these cells escaped were randomly distributed throughout the experiments. We further quantified the silencing time traces of these escaped cells. During their time in the device, all of the escaped cells showed intermittent silencing loss dynamics with no obvious difference to those presented in Fig. 4.2. The data from escaped cells have been excluded from further analysis or presentation in this work.

4.7.5 Correlation analysis of single-cell data

Correlation coefficients(R) for all the scatter plots were calculated using the MATLAB function: 'corrcoef.' To determine the time-dependent relationship between silencing loss in aging mother cells and the occurrence of elongated daughters, we calculated the cross-correlation between silencing reporter fluorescence trajectories of each mother cell (from Fig 4.2a) and the morphology change trajectories of its daughters. The daughter morphology was mapped as a binary variable that is set to "1" when the daughter is elongated and "0" when the daughter is rounded. Because daughter morphology traces are digitalized, we also digitized silencing reporter fluorescence trajectories of mother cells. To this end, we first took the time derivatives of a fluorescence trajectory, and then set positive derivatives as 1(representing the silencing loss state)and negative derivatives as -1(representing the silenced state).For each pair of mother silencing loss trajectory, M_{SL}(1, 2, ... n), and daughter morphology trace i, D_M(1, 2, ... n), with n time points, we aligned them with a time shift $\Delta\tau$: $M_{SL(i)}$ (1, 2, ... n-$\Delta\tau$) and $D_{M(i)}$ (1+$\Delta\tau$, 2+$\Delta\tau$, ... n) for $\Delta\tau \geq 0$, or $M_{SL(i)}$ (1+$|\Delta\tau|$, 2+$|\Delta\tau|$, ... n) and $D_{M(i)}$ (1, 2, ... n-$|\Delta\tau|$) for $\Delta\tau < 0$. For each $\Delta\tau$, we concatenated all mother silencing loss trajectories into one long silencing loss trajectory and all daughter morphology trajectories into one long morphology trajectory. We then calculated the correlation coefficient between the concatenated pair of mother-daughter trajectories with the shift using Matlab function corrcoef. To provide a control for this cross

correlation analysis, we disrupted the original pairing between mother silencing loss and daughter morphology trajectories. Instead of pairing each mother silencing loss trajectory with its own daughter morphology trajectory, we randomly paired mother silencing loss trajectories with daughter morphology trajectories, and then performed the same cross correlation calculation for the concatenated mother trajectory and "randomly reshuffled" daughter trajectory (the dash line in Fig. 4.2d).The correlation analysis revealed a 140 min time lag between silencing loss and daughter morphology trajectories, indicating a 140 min time delay between the changes at the molecular level –the occurrence of silencing loss and the changes at the phenotypic level –the production of elongated daughters during the aging process.

4.7.6 Development of the phenomenological model of cell aging

We developed a phenomenological model that relates silencing and cell aging based on our experimental data. The model only considers the aging process with elongated daughters and postulates that each mother cell can be in one of two states during aging: state 0 –the silencing state in which it produces normal daughters, and state 1 –the silencing loss state with elongated daughters, and a cell may only die from state 1 (Fig. 4.5a).

The transitions between the states are purely stochastic and are characterized by transition probabilities p_{01} and p_{10} that depend on the replicative age of the cell. All the experimental data are from Fig. 4.2a. Due to the phenomenological nature of the model, we only used the age-dependent phenotypic change (elongated daughter) data for model fitting. To deduce the transition probabilities from the single-cell data, we computed the fraction of all the cells at the state with normal daughters (state 0) of a given generation that switch to the state with elongated daughters (state 1) at the next cell cycle f_{01} and the fraction of the cells at the state with elongated daughters (state 1) that return to state 0 at the next cell cycle f_{10}, as a function of the replicative age. As this data shows, the transition rate from state 0 to state 1 gradually increases with age, while the rate of the reverse process decreases and reaches zero after about 25 generations (Fig.

4B). Using linear regression of the data, we approximate the dependence of p_{01} and p_{10} on the replicative age of n by linear functions p_{01}(n) = 0.016n - 0.04 and p_{10}(n) = 0.27 - 0.01n.

We also postulate that in the silencing loss state (state 1), a damage factor D accumulates continuously, and the probability of a cell to die is proportional to D. To obtain the relationship between damage accumulation and cell death, we calculated the fraction f_{1D} cells that died after N consecutive generations in state 1 to total number of cells that lived through N consecutive generations in state 1 (Fig 4.5c). Evidently, this fraction becomes higher with N, however at large N>10 the data becomes very noisy since only small number of cells remain living. We use the data for N<10 to approximate the probability of transition to death from state 1 by a linear function of N, p_{1D}(N)=0.0297N+0.00025and used this expression for all N. We assume that the damage D is proportional to the time the cell spent in state 1 and, once a cell transits back to the silencing state 0, D is reset to zero.

Thus, the phenomenological model depends on two transition rates p_{01} and p_{10} that are linear functions of the generation number n, and the death rate p_{1D} that is a linear function of the number of consecutive generations in state 1. Time unit in simulations is one generation. Based on the experimental data we set one generation in the silencing state is 80 min, and in the silencing loss state, 110 min. We simulated this model stochastically and in each in silico experiment we generated 79 cell state trajectories (same number as cells in experimental data in (Fig. 4.2a). Using these data and averaging over 200 in silico experiments, we computed the number of cells alive at replicative age n as a function of n (Fig. 4.5d, red line), the fraction of cells in state 1 as a function of their replicative age (Fig. 4.5e, red line), and the distribution of continuous generations in state 1 before death (Fig. 4.5f, red line). The error bars indicate standard deviations of the distribution for the corresponding results from multiple runs. All these simulation results match our experimental data very well. We also plotted the individual cell trajectories from one in silicorun ordered according to the replicative lifespan (Fig. 4.5g).

To simulate the effects of silencing perturbations, we increased p_{01} and decreased p_{10} by

ten-fold to generate an induced silencing loss, see Fig. 4.5h. To simulate the transient silencing loss (Fig. 4.5i), we used the same high p_{01} and low p_{10} as in Fig. 4.5h at the beginning of simulation for 4 generations then switch them back to the p_{01} and p_{10} used in Fig. 4.5g.

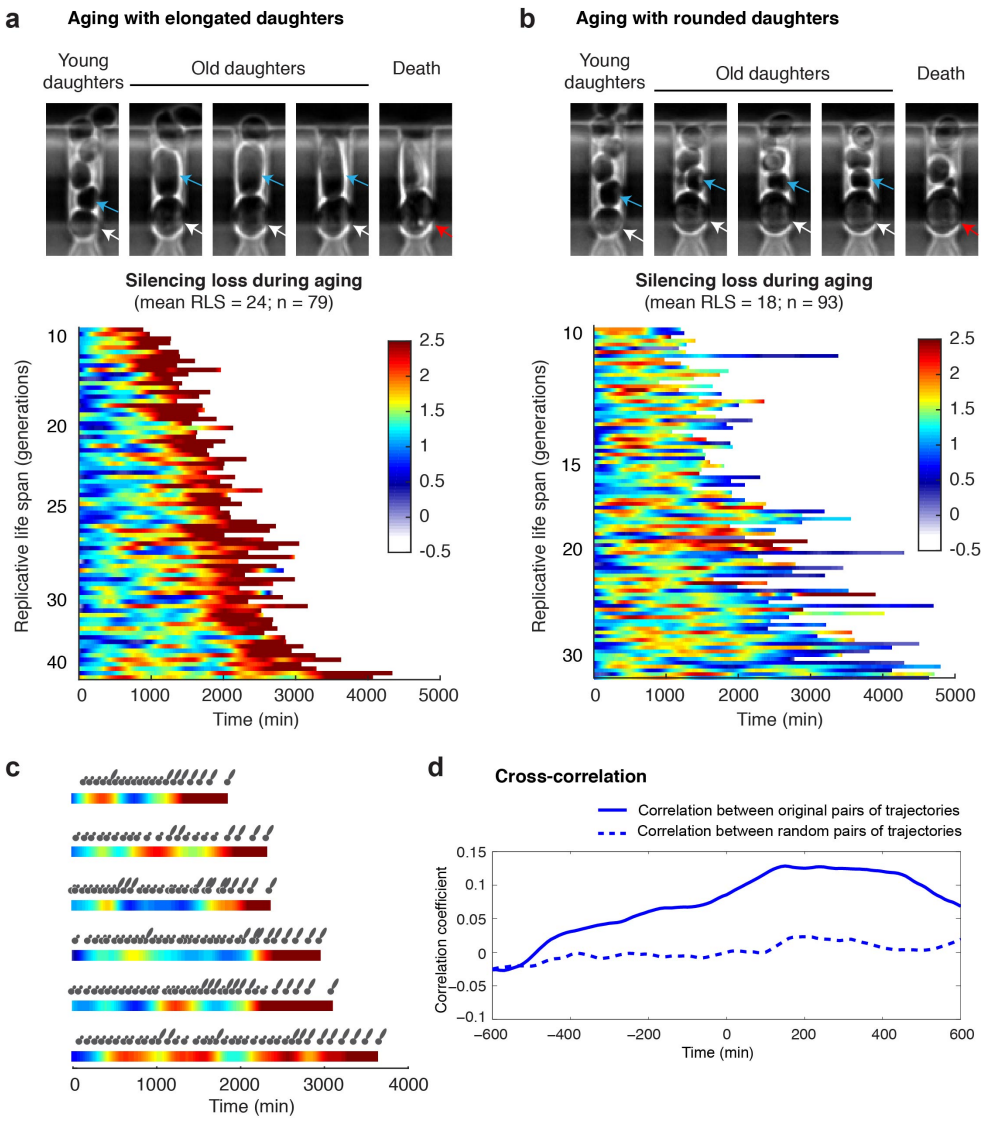

Figure 4.2: Dynamic patterns of silencing loss during aging. (a) Dynamics of silencing loss in cells aging with elongated daughters. (Top) Representative images of cell aging and death with elongated daughters. Blue arrows point to daughter cells, white arrows point to the living mother cell, and the red arrow points to the dead mother cell. (Bottom) Single-cell color map trajectories of reporter fluorescence. Each row represents the time trace of a single cell throughout its life span. Color represents the normalized fluorescence intensity as indicated in the color bar, which is used throughout to allow comparisons between different conditions. Cells are sorted based on their RLSs. (b) Dynamics of silencing loss in cells aging with rounded daughters. (c) Daughter cell morphology is correlated with the silencing state of mother cells. Color map trajectories of representative mothers are aligned with the morphology (round vs. elongated) of daughters produced throughout their life spans. (d) Cross-correlation analysis of daughter morphology and mother silencing dynamics.

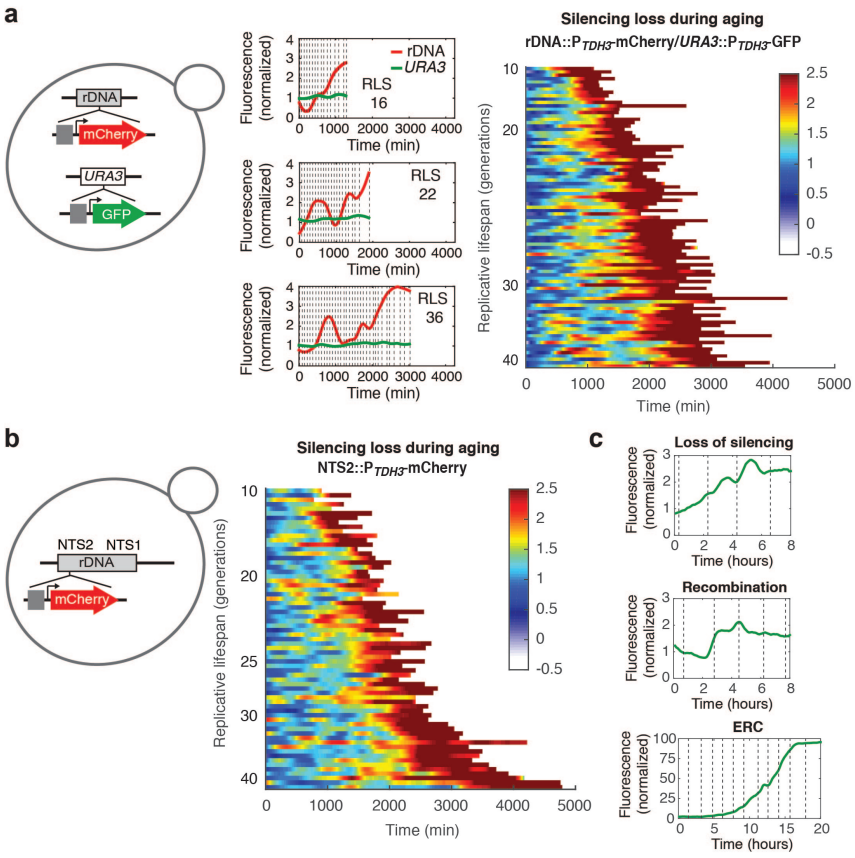

Figure 4.3: Validation of the silencing reporter dynamics during aging. (a) Dynamic patterns of reporter fluorescence are not caused by age-associated global effects on gene expression. Left: A schematic illustrating the dual-color strain, in which mCherry under the TDH3 promoter is inserted at the NTS1 region at rDNA and GFP under the same promoter is inserted at URA3. Middle: Representative single-cell time traces of the dual-color cells throughout their lifespans. Each plot shows the time traces of NTS1-mCherry and URA3-GFP in a single cell. Vertical dashed lines represent division times of the cell, in which the distance between two adjacent dashed lines indicates the cell cycle duration. The number of dashed lines in each trace represents the cell's lifespan. Reporter fluorescence is normalized to the baseline level. Right: Single-cell density map trajectories for rDNA-mCherry divided by URA3-GFP in the same cells (cells aging with elongated daughters). Because the expression of URA3-GFP reporter shows little change during aging, the density map trajectories of rDNA-mCherry, normalized by URA3-GFP in the same cells, show similar patterns to those observed in Fig. 2A. (b) Dynamic patterns of silencing loss are not specific to the NTS1 region of rDNA. Left: A schematic illustrating the strain in which mCherry under the TDH3 promoter is inserted at the NTS2 region at rDNA. Right: Single-cell density map trajectories for NTS2-mCherry during aging. Silencing loss at the NTS2 region shows similar patterns to those observed for the NTS1 region. (c) Representative single-cell time traces for loss of silencing, recombination, or ERC of the reporter gene. Top: Loss of silencing features a gradual fluorescence increase. Middle: Recombination features a fast 2-fold fluorescence change in one cell division and at the same time the daughter cell from that cell division stably loses the reporter gene. Bottom: ERC features a drastic exponential fluorescence increase until detection saturation.

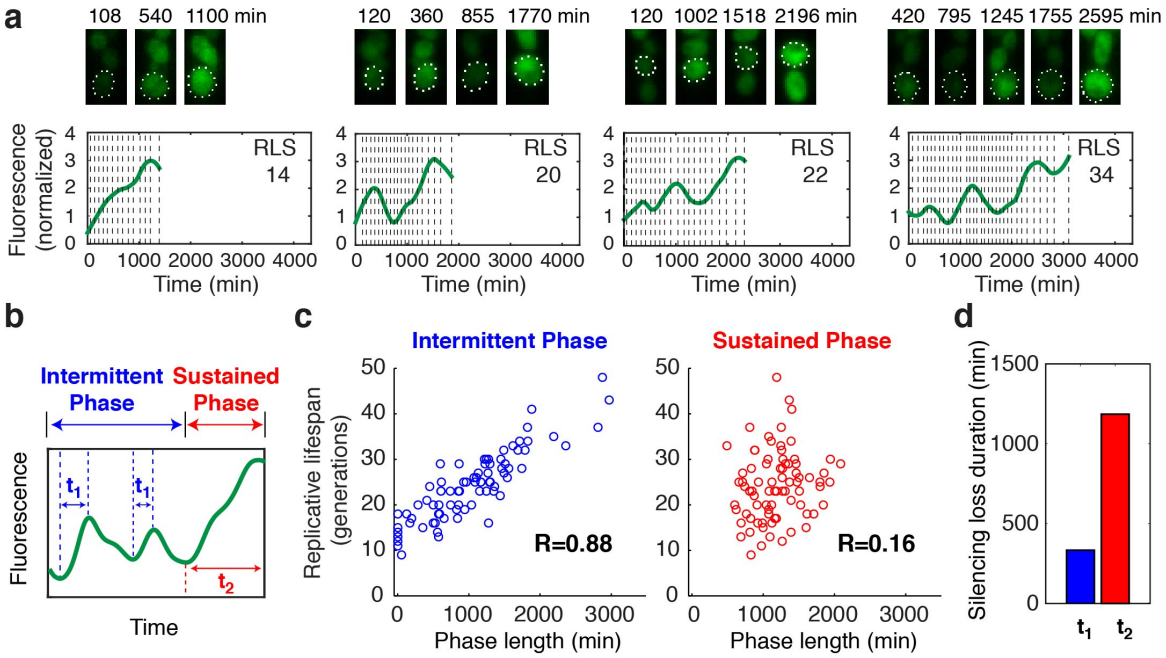

Figure 4.4: A quantitative analysis of silencing loss dynamics in single cells. (a) Dynamics of silencing loss in representative single cells with different life spans. For each cell, (Top) time-lapse images for the cell have been shown with (Bottom) the fluorescence time trace throughout its life span. Vertical dashed line represents each division time of the cell, in which the distance between two adjacent dashed lines indicates the cell cycle length. Reporter fluorescence is normalized to the baseline level. (b) A schematic illustrates the dissection of two phases based on the silencing loss dynamics. The rise times of early sporadic and final sustained silencing loss are defined as t1 and t2,respectively. (c) Scatter plots showing the relationships between the length of (Left) Intermittent Phase or(Right) Sustained Phase and life span at the single-cell level. Single-cell data are from Fig. 2A. Each circle represents a single cell. Correlation coefficient (R) is calculated and shown. (d) Bar graph showing the average durations of (blue) early sporadic and (red) final sustained silencing loss.

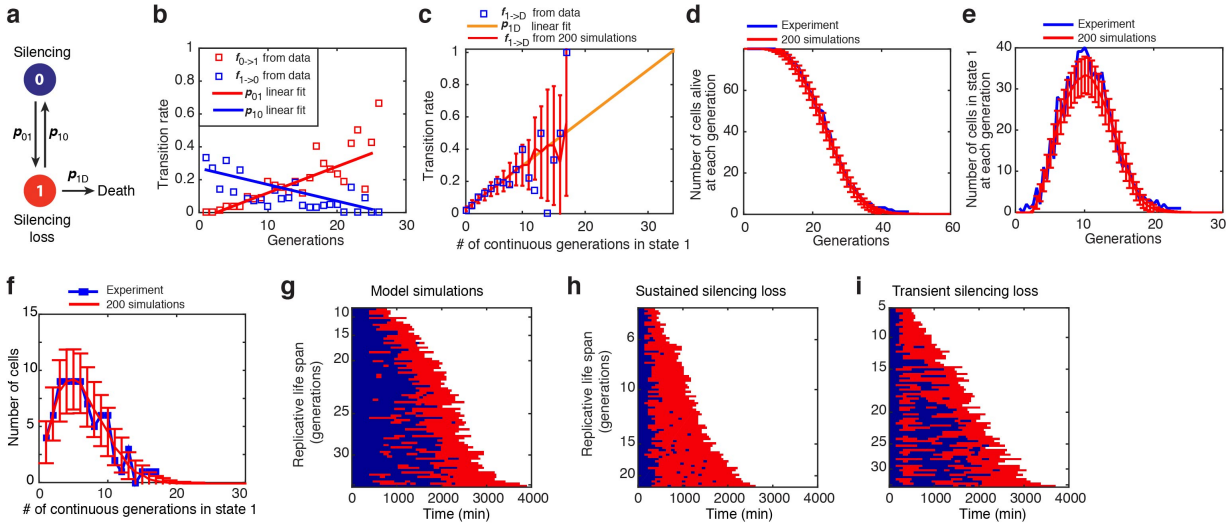

Figure 4.5: A phenomenological model of cell aging. (a) Schematic diagram of the model. The circles indicate the cellular states, and the arrows depict transitions between the states. (b) The statistics of silencing state transitions as a function of age. The fraction of all cells at state 0 of a given generation that switch to state 1 at the next cell cycle (red) and the fraction of the cells at state 1 that return to state 0 at the next cell cycle (blue) have been computed as a function of age. (c) The transition rates from state 1 to death as a function of the number of consecutive generations in state 1. Blue squares are experimentally measured fractions of cells that died exactly after N consecutive generation in state 1 over the total number of cells that lived for at least N generations.Yellow straight line is a linear fit of these data ($0<N<10$). The red line and the error bars indicate the mean and SD of the fraction f_{1D} from simulations. (d) The average number of cells alive as a function of age and the SD in simulations (red line and error bars) and experimental data (blue line). (e) The average number of cells in state 1 as a function of the age and the SD in simulations (red line and error bars) and experimental data (blue line). (f) The distribution of the number of consecutive generations in state 1 until death in simulations (red line and error bars) and experimental data (blue line). All simulation results in c–f were obtained from 200 stochastic simulations of 79 cells. (g) Single-cell state trajectories from a single stochastic simulation of the model with 79 cells at time 0. Each row represents the time trace of a single cell throughout its life span. Blue corresponds to state 0, and red to state 1. Cells are sorted based on their RLSs. (h) Single-cell state trajectories simulated using modified transition rates to reflect sustained silencing loss. (i) Single-cell state trajectories simulated using modified transition rates for four generations to reflect transient silencing loss.

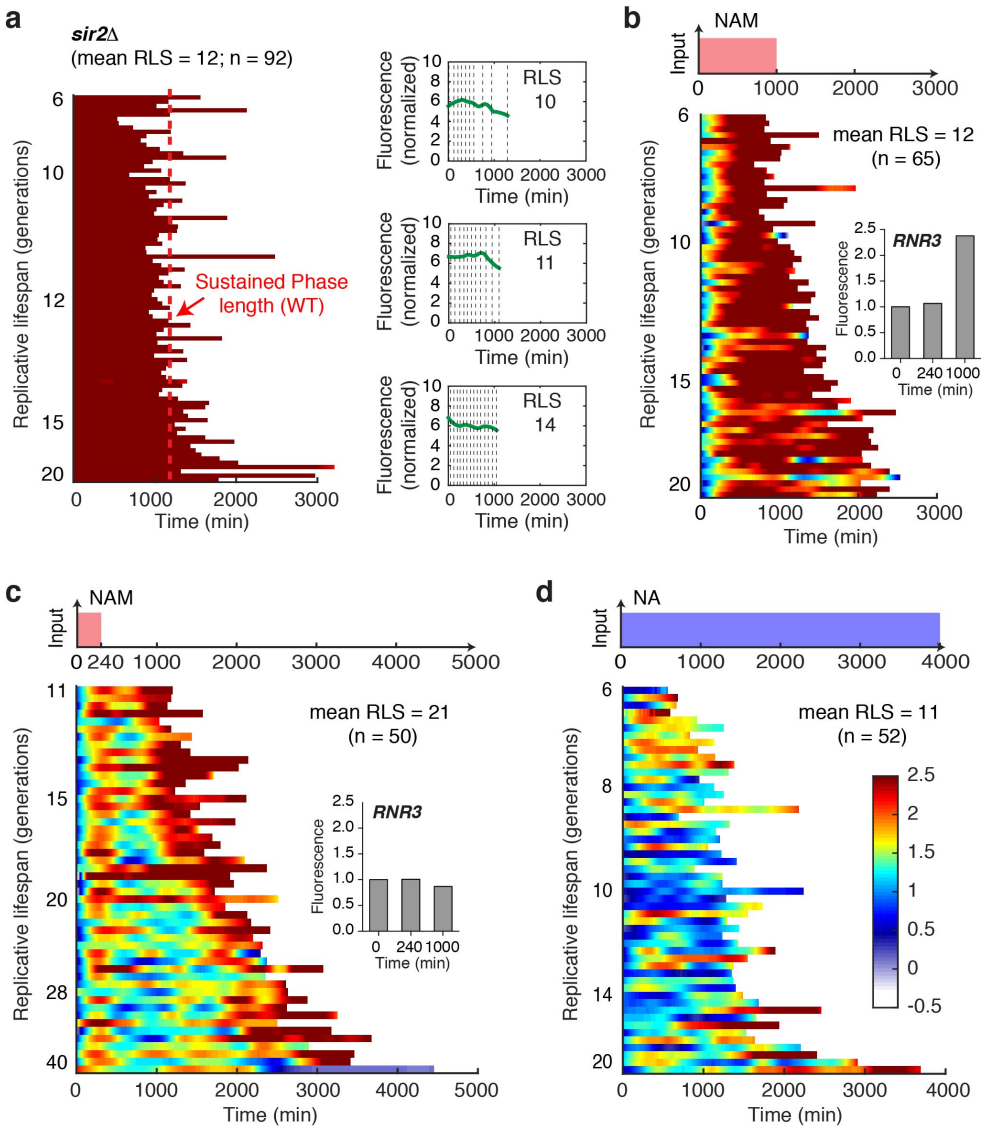

Figure 4.6: Perturbations of silencing dynamics shorten life span. (a) Dynamics of silencing loss in sir2Δ cells. (Left) Single-cell color map trajectories of reporter fluorescence. Each row represents the time trace of a single cell throughout its life span. Color bar is identical to Fig. 4.2. Cells are sorted based on their RLS. The red dashed line represents the average length of Sustained Phase in WT cells, defined in Fig. 4.4b.(Right) Representative single-cell time traces with different life spans. Dynamics of silencing loss in WT cells are shown in response to chemical perturbations. (b) A 1,000-min 5 mM NAM pulse. (Inset) Expression of RNR3-mCherry in response to a 1,000-min 5 mM NAM pulse at indicated times. (c) A 240-min 5 mM NAM pulse. Inset shows the expression of RNR3-mCherry in response to a 240-min 5 mM NAM pulse at indicated times. (d) A constant treatment of 2.5 mM NA. For each condition, (Top) a schematic illustrating the time-based drug treatment has been shown with (Bottom) the corresponding single-cell color map trajectories of reporter fluorescence.

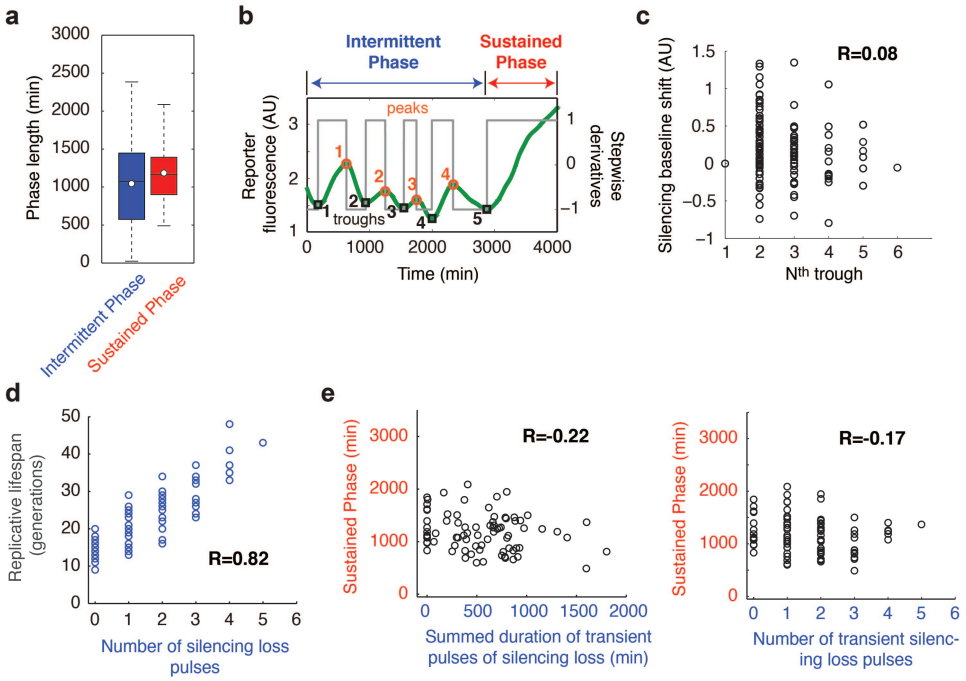

Figure 4.7: Additional quantification of silencing loss dynamics in single cells. (a) A boxplot showing the distributions of (blue) Intermittent Phase length and (red) Sustained Phase length in single cells. Single-cell data are from Fig. 2A. In the plot, the bottom and top of the box are first (the 25th percentile of the data, q1) and third quartiles (the 75th percentile of the data, q3); the band inside the box is the median; the white circle is the mean; the whiskers cover the range between q1-1.5 x (q3-q1) and q3+1.5 x (q3-q1). (b) A schematic illustrates the identification of peaks (orange circles) and troughs (black squares) within Intermittent Phase in a representative single-cell time trace (green curve). The grey trace is the stepwise derivative trajectory of the time trace. (c) A scatter plot showing the relationship between the baseline shift values of troughs and their sequential positions in time traces. For each time trace, the fluorescence value of each trough is subtracted with the value of the 1st trough to calculate the silencing baseline shift during aging of this cell. The baseline shift value of each trough versus its sequential position (1st, 2nd, 3rd, etc.) in a single-cell time trace was plotted. (d) A scatter plot showing the relationship between the number of early silencing loss pulses and final lifespan at the single-cell level. Each circle represents a single cell. (e) Sporadic transient waves of silencing loss have little contribution to cell death. Left: A scatter plot showing the relationship between the summed duration of sporadic transient silencing loss (summed t1 in Fig. 4.4b for each cell) and the duration of Sustained Phase preceding cell death (t2 in Fig. 3B for each cell) at the single-cell level. Single-cell data are from Fig. 4.2a. Each circle represents a single cell. Correlation coefficient (R) has been calculated and shown. Right: A scatter plot showing the relationship between total number of sporadic transient waves of silencing loss and the duration of Sustained Phase at the single-cell level.

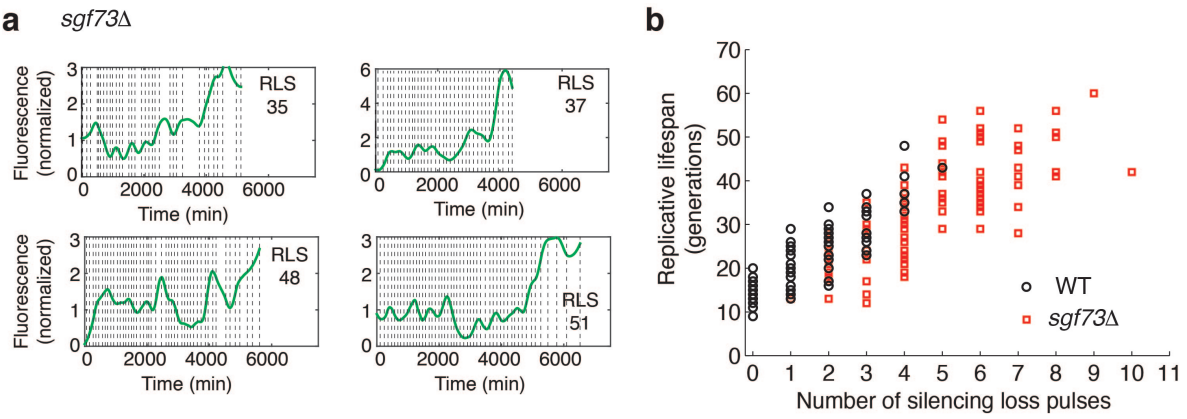

Figure 4.8: Dynamics of silencing loss in *sgf73*Δ. (a) Representative single-cell time traces of silencing loss in *sgf73*Δ. Vertical dashed line represents each division time of the cell, in which the distance between two adjacent dashed lines indicates the cell cycle length. Reporter fluorescence is normalized to the baseline level. (b) A scatter plot showing the relationship between the number of early silencing loss pulses and final lifespan at the single-cell level for WT (black circles) and *sgf73*Δ (red squres). Each symbol represents a single cell.

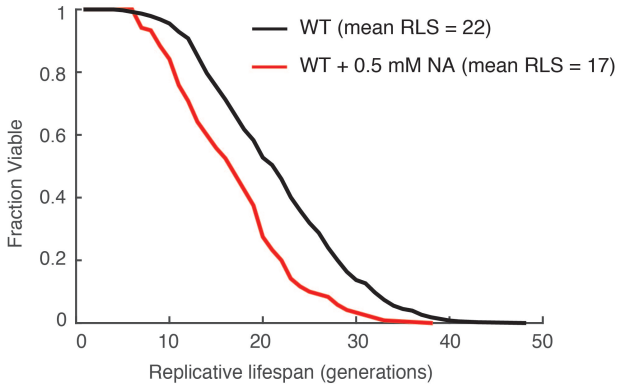

Figure 4.9: A constant treatment of 0.5 mM NA shortens the lifespan. Lifespan curves have been shown for WT cells with (red solid curve) or without (black solid curve) 0.5 mM NA treatment. The NA concentration used in Fig. 4.6D (2.5 mM) is lower than that used in most previous studies (5 mM)(Anderson et al, Nature, 2003 [156]; Bitterman et al, JBC, 2002 [149]). Here, the dosage of NA has been further reduced by 5 times to 0.5 mM, which is the lowest dose that can be found in the literature (Mei et al, PLoS Biol, 2015 [157]). A constant treatment of this very low dose of NA also resulted in a significantly shortened lifespan.

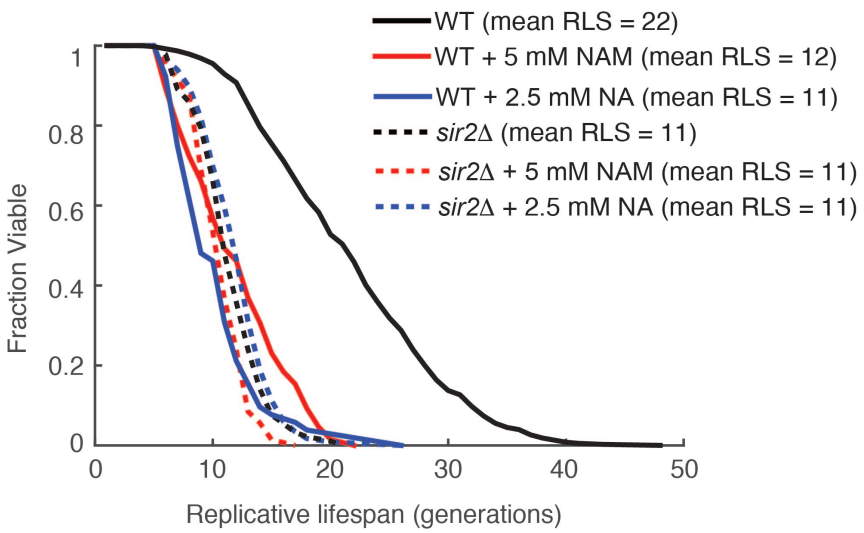

Figure 4.10: The effects of NAM and NA treatments on lifespan are mediated through Sir2. Lifespan curves have been shown for WT cells with 5 mM NAM (red solid curve) or 2.5 mM NA (blue solid curve) treatments, or in normal growth medium (black solid curve), as well as sir2Δ cells with 5 mM NAM (red dashed curve) or 2.5 mM NA (blue dashed curve) treatments, or in normal growth medium (black dashed curve).

4.8 Acknowledgements

This chapter contains material that was originally published as Li, Y.*, Jin, M.*, O'Laughlin, R.*, Bittihn, P., Tsimring, L.S., Pillus, L., Hasty, J. and Hao, N., 2017. Multigenerational silencing dynamics control cell aging. Proceedings of the National Academy of Sciences, 114(42), pp.11253-11258.(*equal contribution). The dissertation author, Richard O'Laughlin, was a primary investigator and author of this work.

Chapter 5

A high-throughput microfluidic platform for monitoring gene expression dynamics in yeast

5.1 Introduction

As discussed in Chapters 3 and 4, the use of microfluidic devices combined with time-lapse fluorescence microscopy can yield powerful insights into dynamic biological processes inside single cells. Yet, despite the power of this approach, it has certain limitations in the amount of information it can obtain in a single experiment. One reason for this is that there are limits in the number of distinguishable fluorescent markers that can be visualized in a single experiment; the upper limit of this number is typically around 4 (meaning that, for example, 4 different genes can be tagged in a cell with distinct fluorescent proteins whose excitation and emission spectra do not overlap with one another). Further, the finite times required for microscope stages to move to, focus and acquire images limits time-resolution, scale and extent of what can be imaged in a microfluidics experiment. As such, microfluidic platforms such as the ones described in Chapter

2 are best suited to targeted studies in which the genes one wishes to study are known ahead of time and relatively small in number. On the other hand, these devices not efficient for studies in which one wishes to obtain the dynamics of hundreds or thousands of genes simultaneously in an unbiased manner. To conduct such studies in yeast, a new kind of microfluidic device is needed to study gene expression dynamics at the genome-scale.

5.1.1 The 'Dynomics' platform

The Hasty Lab has recently developed a custom high-throughput microfluidic device, optical enclosure and imaging platform termed 'Dynomics' [179]. The microfluidic device that composes the 'Dynomics' platform consists of an array of 'spotting regions' where 2,176 different strains of *E. coli* can be robotically arrayed onto the device [179]. A custom optical system houses the microfluidic device and a single image can capture the entirety of the chip. Both GFP fluorescence images and transmitted light images can be obtained [179]. Finally, the power of this platform was demonstrated by utilizing the *E. coli* GFP promoter library [180] growing on the microfluidic device to sense heavy metal toxins, and machine learning was was utilized to detect which metals were present [179].

However, despite the tremendous utility of the 'Dynomics' platform in monitoring gene expression dynamics in *E. coli* in response to different environmental conditions, the microfluidic device was not able to support robust growth of budding yeast. Although various designs were tested in order to try to obtain healthy growth of yeast cells, most strategies failed. Thus, I set out to solve this problem and develop at robust 'Dynomics' microfluidic device for *S. cerevisiae*. However in order demonstrate the power of this new technology, we had to select an experimental area on which to test and validate the device. We selected the yeast diauxic shift as the testing condition for the device, as it is a well-studied phenomenon where gene expression is highly dynamic.

5.1.2 The yeast diauxic shift

The budding yeast *Saccharomyces cerevisiae* is a 'facultative fermenter' [181, 182], meaning that in the presence of oxygen, fermentation is the dominant form of metabolism, not respiration via oxidative phosphorylation in the mitochondria. Thus, for yeast cells grown in a culture flask with glucose supplied as the carbon source, this so-called 'Crabtree effect' [181–183] predominates; yeast uptake glucose from the media, convert it into pyruvate via glycolysis and then pyruvate is converted into ethanol and carbon dioxide in a reaction that oxidizes NADH and regenerates NAD+ that can be used for glycolysis [181, 183]. This continues as the yeast culture grows exponentially in the flask, until nearly all of the glucose is exhausted from the media. At that point, yeast cells can no longer rely on glucose as a carbon source, and switch to uptaking and oxidizing the built up ethanol in the media to power cellular respiration in the mitochondria [181–183]. This switch from fermentive to oxidative metabolism is known as the diauxic shift and is typically characterized by a short lag phase after the exponential growth phase of the culture — in which cell growth is halted to alter the metabolic machinery of the cell to oxidize ethanol— and a subsequent resumption of growth at a slower rate than during the exponential phase [181–186]. Interestingly, a similar phenomenon to the 'Crabtree effect' is also observed in some cancer cells, whereby glycolysis is elevated at the expense of respiration, known as the Warburg effect [187]

Given the extensive changes in cellular metabolism that occur during the diauxic shift, it is perhaps no surprise that gene expression during this process is highly dynamic. As a result, multiple studies have characterized the gene expression changes that occur during the diauxic shift by using transcriptomic and proteomic approaches [184–186]. These studies have revealed a great deal about how have cells respond to changing carbons sources in the media, including upregulation of enzymes involved in the glyoxylate cycle and cellular respiration [184, 185], the downregulation of many ribosome-associated genes [184, 186], the upregulation of many stress response genes [184] and the induction of distinct enzymatic isoforms [184]. However, despite

the great deal of information about metabolic gene regulation that has been discovered by the recent omics studies on the diauxic shift [184–186], the transcriptomic and proteomic methods utilized in previous work could be greatly complemented through a microfluidics and time-lapse fluorescence microscopy based approach.

Firstly, monitoring the diauxic shift on the genome scale in a microfluidic device could provide increased time resolution for monitoring gene expression dynamics, on the scale of minutes rather than hours for transcriptomic and proteomic approaches [184–186], which could aid in understanding the temporal ordering of cellular events during diauxic shift by revealing phenomena such as 'just-in-time' gene expression [188]. Secondly, the media environment of the microfluidic chip can be dynamically modified throughout the course of the diauxic shift, allowing a researcher to study how various perturbations affect the diauxic shift. Finally, the use of a microfluidic platform capable of detecting the diauxic shift could serve as a valuable real-time monitoring tool in the ferementation industry where yeast fermentations result in the production of beer and wine.

5.2 Results

5.2.1 Design and validation of a high-throughput microfluidic platform for *S. cerevisiae*

To develop a 'Dynomics' microfluidic device for culturing yeast, we drew inspiration from the microfluidic device described in Chapter 2.3.1. As a brief review, this device uses media channels that turn back on themselves in order to carry flow in two opposite directions. Cell traps are positioned perpedicular to these channels so that some portion of the media will flow from the media channel closest to the entrance of the trap directly through the trap an out to the portion of the media channel next to the exit of trap. The cell traps consist of two layers,

one that is taller than the height of a single cell which serves to collect cells in the trap and another which is smaller than the height of a single cell which functions to prevent movement past a certain point in the trap. As previously discussed in Chapter 2.2.2., this is a strategy for hydrodynamic trapping [72–77]. Since this approaches allows for rapid and autonomous loading of cells traps and also maintains a healthy nutrient environment for cells, a high-throughput microfluidic platform was designed according to this strategy (Fig. 5.1).

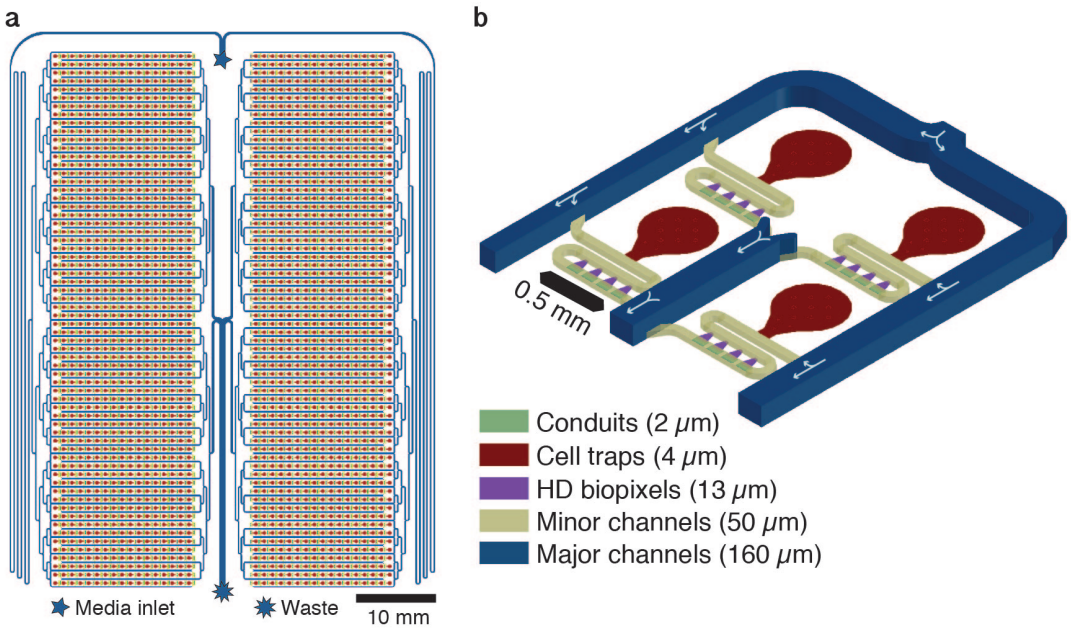

Figure 5.1: A high-throughput microfluidic platform for gene expression dynamics in budding yeast. (a) Device design, consisting of a single fluidic layer with five different feature heights. Up to 2,176 unique strains can be loaded onto the device. (b) Close-up of individual strain banks on the device. A Singer ROTOR robot deposits individual strains onto the 4 μm spotting regions shown in red. Major and minor channels, shown in blue and yellow respectively, carry media to supply nutrients to these cells once fluidic lines are connected and experiments have begun. Cells subsequently grow out of these spotting regions where they are carried by the media flow into the HD biopixel regions, shown in purple. Cells are then trapped in this region during the entire course of the experiment as they cannot proceed past the 2 μm conduits, shown in green.

The yeast 'Dynomics' device consists of 2,176 strain bank regions arranged in a layout similar to the previously published chip for *E. coli* [179] (Fig. 5.1a). However, instead of measuring cellular fluorescence from the spotting regions (Fig. 5.1b, 4 μm red features) as done

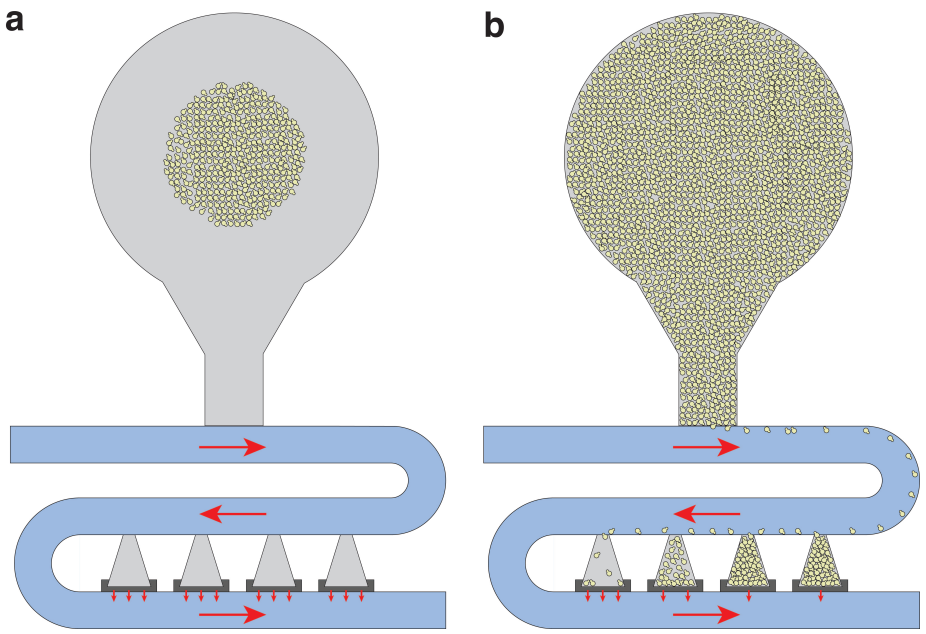

Figure 5.2: Loading of HD biopixels from the spotting region. (a) Cells are initially deposited in the spotting region at the very start of the experiment. (b) Media supplied via the major and minor channels stimulates growth of the spotted cells. Following the flow of media (red arrow) through each minor channel, cells are loaded into the cone-shaped HD biopixels. The loading of each HD biopixel increases the fluidic resistance through that trap, thereby promoting loading of downstream HD biopixels.

by Graham et al. [179], fluorescence is measured in what are called HD (hydrodynamic) biopixels. To accomplish this, we designed the minor media channels (Fig. 5.1b, 50 μm yellow features) to snake back on themselves, allowing media to flow through a set of four cone-shaped 70 μm by μm 'biopixels' [176] (Fig. 5.1b, 13 μm tall purple features). A set of 'conduits' (Fig. 5.1b, 2 μm green features) fluidically connect the media channels at each end of the biopixels. This design thereby allows hydrodynamic trapping of cells in the biopixel region; as cells grow out of the spotting region (Fig. 5.2a), they are guided by the fluid flow into the HD biopixels and not able to pass under the conduits. They subsequently grow to fill the HD biopixels (Fig. 5.2b). This approach allows for very efficient and automatic loading of cells from the spotting regions into the biopixel regions, which provide a superior environment for uniform and exponential cell growth, relative to the mouth of the spotting region. Further, because the HD biopixels are 13

μm in height, they allow for increased fluorescence signal to be obtained compared to the 4 μm spotting regions.

We susequently validated the performance of the HD biopixels across the entire microfluidioc device in a dynamic environment. A strain expressing a GFP tagged HXT2 gene was arrayed onto every strain bank of the device. We measured the response of this strain across the entire device to a gradual carbon source shift from glucose to galactose and then back to glucose. Fluorescence from all biopixels, totaling 8,704, was measured (Fig. 5.3). The expression of HXT2-GFP was extremely uniform across the device and displayed expression dynamics similar to what has been reported in the literature [189]. As glucose was decreased we observed a sharp increase in HXT2-GFP expression, consistent with Ruiz et al. [189]. However when glucose levels fell below 0.02% with 2% galactose also in the media, HXT2-GFP expression began to decrease, yet recovered to the original baseline value when 2% glucose was added back to the media (Fig. 5.3).

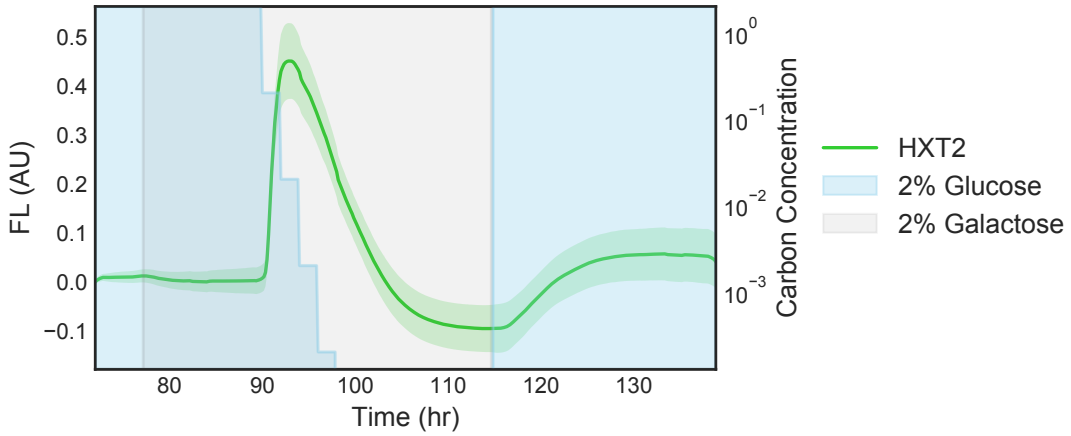

Figure 5.3: Performance of HD biopixels across the microfluidic device. The HXT2-GFP strain from the yeast GFP-fusion library [190] was arrayed onto every position of the device. The response of this strain to a dynamic shift in the carbon source of the media, from 2% glucose to 2% galactose was measured. A low pass filter of the mean GFP signal from each biopixel on the chip (a total of 8,704 bioxpixels from 2,176 spotting regions) is displayed, with the solid green line representing the mean and the shaded region representing the standard deviation.

5.2.2 Quantitative real-time observation of the yeast diauxic shift using the Dynomics platform

Having validated the performance of the HD biopixels, we next sought to test the capability of the device in monitoring genome-wide expression changes in a naturally occurring dynamic environment. Toward this end, the yeast diauxic shift (Chapter 5.1.2) provides an ideal condition in which to perform such tests. To conduct this experiment, flasks containing growing yeast cultures were continuously sampled each hour for 56 hours. Media was filtered to remove cells and added onto the two microfluidic devices which each contained one half of the yeast GFP library [190]. Over this time, the culture went through the diauxic shift, growing exponentially on glucose at first, followed by a short lag phase in which the OD600 of the culture remained relatively flat, followed by another period of growth (the post-diauxic shift growth phase) before stationary phase was entered (Fig. 5.4). In this way, the diauxic shift occurring in the flask cultures could be mirrored on microfluidic devices.

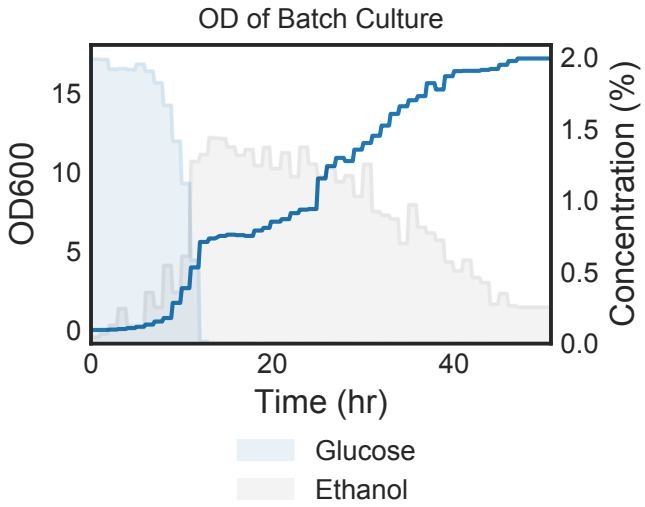

Figure 5.4: Growth, glucose and ethanol levels of batch cultures undergoing the diauxic shift. All values were measured hourly. Exponential growth was observed before until glucose depletion (shown in blue). After an approximately 10 hour lag phase the culture resumed growth by metabolizing ethanol, as demonstrated by the decreasing ethanol levels in the media (shown in gray) after the lag phase.

As the flask cultures underwent the diauxic shift, we also observed changes in gene expression across the genome on the Dynomics microfluidic device (Fig. 5.5). Groups of genes were observed to significantly increase after the diauxic shift while others noticeably decreased after the diauxic shift. More minor changes could be seen throughout the genome (Fig. 5.5). Having observed these patterns we performed follow-up analysis on the gene expression profiles obtained from the experiment.

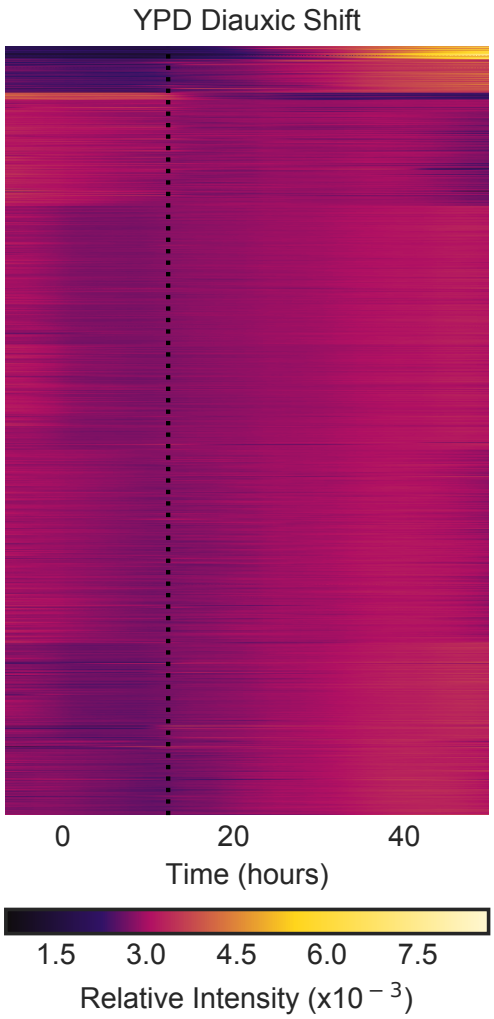

Figure 5.5: Heat map of gene expression dynamics during the diauxic shift. Relative intensity is plotted for the 3,761 strains on the chip with detectable fluorescence levels. Batch culture media was added to the device at time 0 and exhaustion of glucose from the batch culture is indicated by the black dotted line.

To better understand the patterns of gene expression observed during the diauxic shift, clustering analysis was performed. Using hierarchical agglomerative clustering, we were able to extract six clusters that expressed distinct patterns of gene expression dynamics during the diauxic shift experiment (Fig. 5.6). The first cluster consisted of 64 strains in which those genes increased dramatically after the glucose in the media was depleted. Gene ontology term enrichment revealed that genes involved in the TCA cycle, oxidative phosphorylation and gluconeogenesis were in this cluster. Similarly, cluster 2 contained genes that increased after glucose depletion but to a somewhat lesser extent. This cluster included also genes for oxidation-reduction processes as well as gluconeogenesis and the cellular response to oxidative stress.

Genes that were down-regulated during the diauxic shift fell into clusters 3 and 4. Notably, both of these clusters contained genes related to ribosome function. The genes belonging to cluster 3 dropped precipitously after glucose was depleted from the media, while the genes in cluster 4 gradually decreased as glucose levels dropped, yet remained relatively constant during the post-diauxic shift growth phase before decreasing again during stationary phase. Finally the dynamics of genes belonging to clusters 5 and 6 were much more difficult to discern. In both clusters, gene expression modestly drops during glucose depletion, increases when glucose is exhausted and decreases again during stationary. Since the overall change in these signals in low compared to genes that are members of the other 4 clusters, it is possible that these modest changes in fluorescence do not reflect meaningful changes in gene expression. This notion is further supported by the fact that YPD media used during this experiment is has considerable GFP fluorescence. Thus, strains in clusters 5 and 6 may have relatively flat GFP levels across the experiment, but changes in media fluorescence during the experiment, or other such minor perturbations, could have had an effect on their fluorescence. A full list of significant GO terms for each cluster can be found in Table 5.2, Table 5.3 and Table 5.4.

We can also explore the individual time traces of different genes to further validate that the strains on the chip underwent the diauxic shift along with the batch cultures. The proteomic study

by Murphy et al. [184] revelaed that different enzyme isoforms are differentially regulated during the diauxic shift. In Fig. 5.6, we plot four groups of enzymes that were also analyzed by Murphy et al. [184]. Alcohol dehydrogenase genes ADH3 and ADH5, which convert acetaldehyde to ethanol, were found to have relatively constant expression by Murphy et al. [184]. On the other hand, ADH2 expression, which converts ethanol to acetaldehyde, was found to sharply increase after glucose depletion [184]. Results from our microfluidics experiment recapitulated these findings (Fig. 5.7a). Similarly, for trios-phosphate dehydrogenase and glutamate dehydrogenase genes, TDH1 and GDH2 genes exhibited strong induction upon glucose depletion, wereas their respective isoforms did not, consistent with results from Murphy et al. [184] (Fig. 5.7c, d). However, in the case of aldehyde dehydrogenase genes, there was a modest departure between our results and those of Murphy et al. [184]. While ALD4 expression increased in both our study and that of Murphy et al. [184], we did not see much increase in ALD2 or ALD3 expression as reported by Murphy et al. [184]. Further for ALD6 expression, we saw a drop in expression that did not return to baseline values, while Murphy et al. [184] saw a drop in ALD6 expression around the time of glucose depletion that then returned to baseline. However, taken together, our results and those from Murphy et al. [184] are largely in agreement with respect to expression levels of these various enzymatic isoforms.

5.3 Discussion

By analyzing gene expression dynamics of strains from the yeast GFP-fusion library [190], the data indicates that the diauxic shift of the growing batch culture could be detected on the Dynomics chip. This is supported by expression changes in a number of genes which are in agreement with what has been obtained in the literature [184–186]. Perhaps most noteably, genes involved in the TCA cycle, cellular respiration and gluconeogenesis were all upregulated upon glucose depletion in the media, as expected from numerious previous studies on the yeast

diauxic shift [184–186]. This indicates that cells growing in the microfluidic device indeed underwent a change in metabolism when glucose was depleted, switching to oxidizing ethanol and conducting cellular respiration in order to grow and divide. Further ribosome related genes were present in the clusters that were downregulated upon glucose exhaustion from the culture, as previously observed [184, 186]. Furthermore, we also observed upregulation of genes involved in cellular stress response when glucose was depleted from the media, as observed by Murphy et al. [184]. For example, as shown in Fig. 5.6, the general stress response genes HSP42, a heat shock protein [191], is upregulated during the diauxic shift and is present in cluster 2 of Fig. 5.6. Along these lines, we also observed upregulation of genes that are known to be repressed under fermentable carbon sources such as ACS1 [192].

These results are a proof-of-principle that dynamic environmental conditions, such as the changing carbon source utilization of yeast during the diauxic shift, can be accurately tracked in real-time on the yeast Dynomics platform. This approaches offers a number of advantages and the present results and approach can be enhanced in a number of ways for both basic science and technology purposes. We envision that this platform can greatly aid in understanding genetic regulation in yeast in dynamically changing environments, as well as aid in improving industrially relevant processes using yeast by providing real-time feedback on the state of liquid yeast cultures.

5.4 Methods

The yeast Dynomics wafer was built using standard photolithography protocols that have been detailed previously [23, 179]. In the fabrication of all feature heights of the device, SU8 2000 series (MicroChem Corp.) photoresist was used. Spin speeds are heights are shown below in Table 5.1. Loading of the yeast GFP-fusion library [190] was performed similar to Graham et al. [179], with temperature and waiting times for a number of steps optimized to budding yeast.

Table 5.1: Photolithography fabrication parameters for the yeast Dynomics device. Photoresist for the major channels was spun on top of the undeveloped photoresist for the minor channels.

SU8 photoresist	Spin speed	Height
2002	1000 rpm	2.3 μm
2005	2600 rpm	5.3 μm
2007	1000 rpm	13.1 μm
2075	4000 rpm	55-65 μm
2075	2400 rpm	145-170 μm

For the control experiments for validating the device (Fig. 5.3), complete supplemental mixture (CSM) media (Sunrise Science Product) without histidine was used to grow cells. For the diauxic shift experiment, four cultures of the yeast strain DBY12020 were grown in 400 mL of YPD media in 2L flasks. Flasks were inoculated with starter cultures that were at 0.02OD and were subsequently grown at 30°C. Every hour thereafter, 5 mL was sampled from each of the 4 flasks was taken, combined together and the OD600 was measured and recorded. These samples were then filtered to remove cells and 7 mL was placed on each of the two microfluidic devices that were running. Each device contained half of the yeast GFP-fusion library [190]. The remaining approximately 6 mL of media was frozen at -20°C, and later analyzed for glucose and ethanol measurements. The glucose level in the media was measured by the Cancer Metabolism group at the Sanford Burnham Prebys Medical Discovery Institute using a YSI 2950. Ethanol concentrations were determined with the Millipore-Sigma Ethanol Assay Kit (MAK076-1KT). In all yeast Dynomics experiments 0.04% tween-20 (Sigma) was added to the media. Images were acquired every 10 minutes with 1 second exposure time for transmitted light images and 1 minute exposure time for GFP fluorescence images.

Fluorescence values for the biopixels were background subtracted and background normalized. A strain containing only a histidine selection marker without GFP was present of each microfluidic device. This strain was yRO136 (BY4741 his3::SpHIS5 (HISMX6)). The histidine selection marker inserted into this strain was from Addgene plasmid 44836. We subtracted the

mean HD biopixel fluorescence values from these strains on each chip from all other strain fluorescence values on that chip in order to aid in trends in fluorescence not due to changes in GFP fluorescence (for example, due to changing fluorescence of the media during the experiment). To remove small negative values in traces that resulted from pre-processing we added 0.1 to each trace value. We plotted relative intensity of fluorescence, the percentage each measured value was divided by the total value of all measurements for that trace, as was done by Murphy et al. [184]. We note that a number of strains were removed from analysis before clustering and follow-up data analysis was performed. These were strains where either clogging was observed or the fluorescence signal was not high enough to rise over our detection limit. We defined this detection limit as any raw fluorescence traces whose integral or area under the curve over the course of the experiment was less than that of the lowest area under the curve of the yRO136 control strains present on each chip. Also we excluded the initial seeding and growth phases of the cells in the biopixels from anlaysis, only including values from eight hours before samples from the culture flasks were added to the chip.

Data analysis was performed in Python using the Dynomics package in Python [179] and scikit-learn was used for clustering analysis. The GOATOOLS package was used for gene ontology (GO) analysis [193].

5.5 Acknowledgements

This chapter contains material that will be incorporated into a manuscript for eventual submission and publication. The following individuals were involved in the work described in this chapter which will be utilized for submission: O'Laughlin, R.*, Stasiowski, L.*, Thouvenin, G.* and Hasty, J. (*equal contribution). "A genome-scale microfluidic platform for monitoring gene expression dynamics in yeast." (title tentative). The dissertation author, Richard O'Laughlin, was a primary investigator and author of this work.

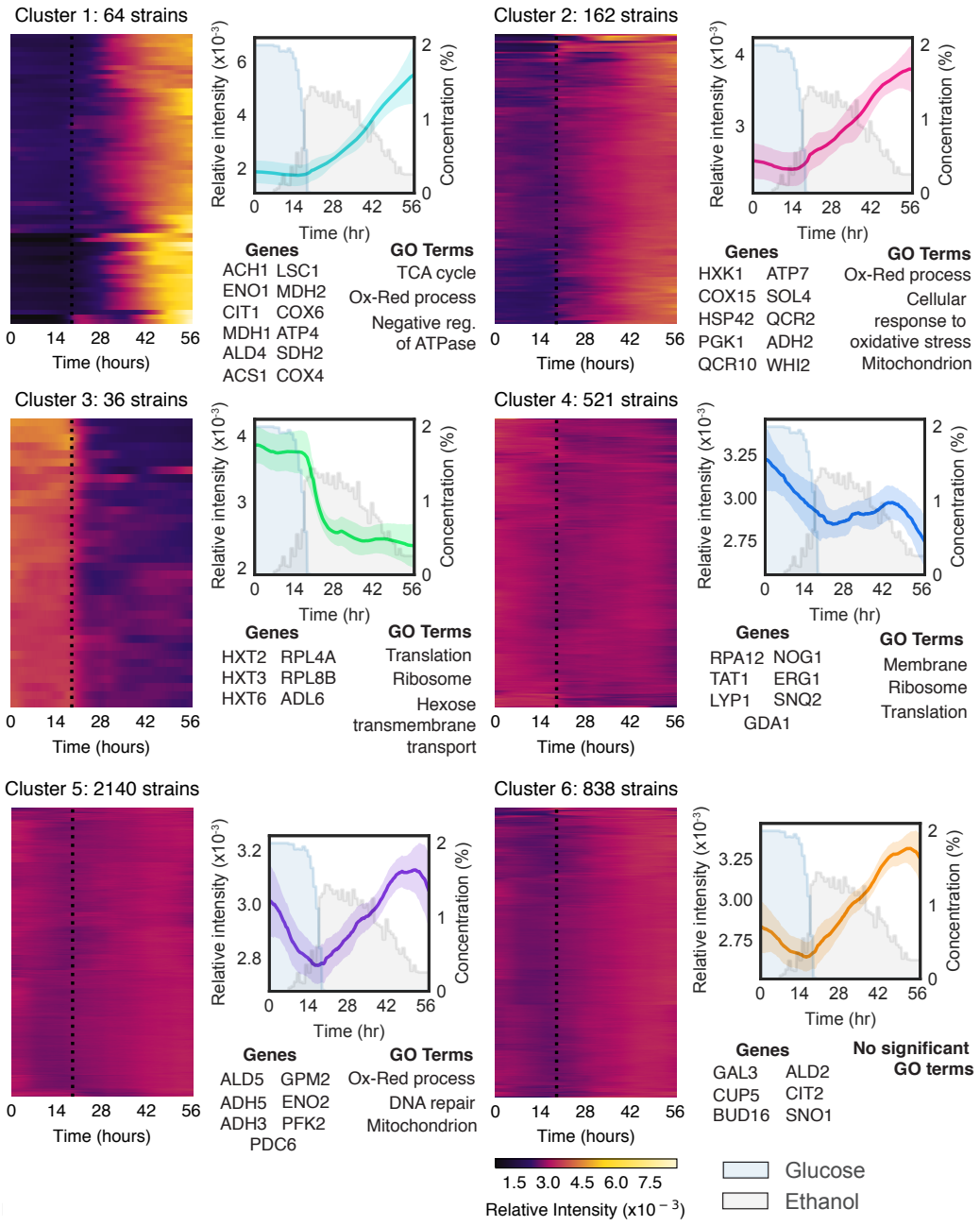

Figure 5.6: Analysis of gene expression dynamics during the diauxic shift through hierarchical agglomerative clustering and gene ontology enrichment. Data can be grouped in six different clusters. Heat maps of relative intensities for genes in each cluster are shown. Mean relative intensity (solid lines) and standard deviation (shaded region) are plotted for each cluster. Genes belonging to each of the clusters, along with examples of significant GO terms associated with the genes present in those clusters are shown. Significant was determined at $P < 0.05$, with the Benjamini-Hochberg method used to adjust false discovery rate.

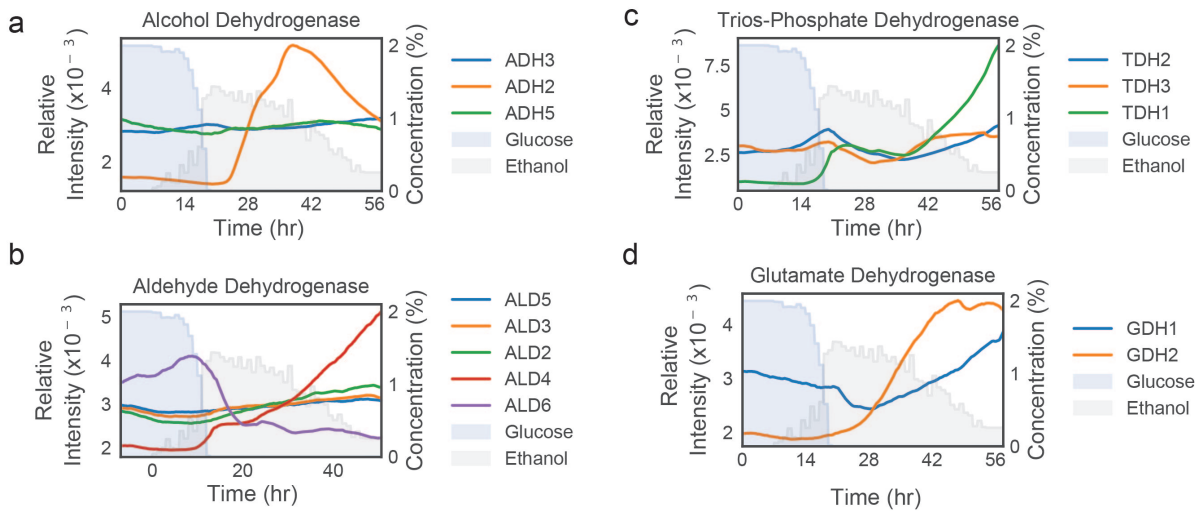

Figure 5.7: Expression patterns of enzymatic isoforms during the diauxic shift. (a) Gene expression dynamics of alcohol dehydrogenase genes ADH2, ADH3 and ADH5 during the diauxic shift. (b) Gene expression dynamics of aldehyde dehydrogenase genes ALD6, ALD5, ALD4, ALD3 and ALD2 during the diauxic shift. (c) Gene expression dynamics of trios-phosphate dehydrogenase genes TDH1, TDH2 and TDH3 during the diauxic shift. (d) Gene expression dynamics of glutamate dehydrogenase genes GDH1 and GDH2 during the diauxic shift. Similar gene expression profiles for these isoforms were obtained by Murphy et al. [184].

Table 5.2: Gene ontology terms associated with genes significantly upregulated during the diauxic shift from clusters 1 and 2 from Figure 5.5, $P < 0.05$.

Cluster	Term	Term Name	P-Value
1	GO:0006099	tricarboxylic acid cycle	7.681185e-11
1	GO:0005739	mitochondrion	7.681185e-11
1	GO:0055114	oxidation-reduction process	1.042798e-09
1	GO:0016491	oxidoreductase activity	8.751906e-07
1	GO:0006103	2-oxoglutarate metabolic process	3.135549e-03
1	GO:0032780	negative regulation of ATPase activity	3.135549e-03
1	GO:0009353	mitochondrial oxoglutarate dehydrogenase complex	3.135549e-03
1	GO:0004591	oxoglutarate dehydrogenase (succinyl-transferr...	3.135549e-03
1	GO:0042645	mitochondrial nucleoid	3.849536e-03
1	GO:0005759	mitochondrial matrix	5.223755e-03
1	GO:0046872	metal ion binding	6.496136e-03
1	GO:0006119	oxidative phosphorylation	6.607367e-03
1	GO:0006546	glycine catabolic process	6.607367e-03
1	GO:0005960	glycine cleavage complex	6.607367e-03
1	GO:0004375	glycine dehydrogenase (decarboxylating) activity	6.607367e-03
1	GO:0006090	pyruvate metabolic process	1.074172e-02
1	GO:0003824	catalytic activity	1.074172e-02
1	GO:0015986	ATP synthesis coupled proton transport	1.370487e-02
1	GO:0046933	proton-transporting ATP synthase activity, rot...	1.370487e-02
1	GO:0005743	mitochondrial inner membrane	1.686306e-02
1	GO:0006094	gluconeogenesis	1.713736e-02
2	GO:0005739	mitochondrion	1.726741e-08
2	GO:0055114	oxidation-reduction process	2.804730e-08
2	GO:0016491	oxidoreductase activity	1.939967e-05
2	GO:0006096	glycolytic process	1.719811e-04
2	GO:0005758	mitochondrial intermembrane space	1.911379e-04
2	GO:0005737	cytoplasm	4.148816e-04
2	GO:0003779	actin binding	1.148191e-03
2	GO:0003824	catalytic activity	1.148191e-03
2	GO:0051015	actin filament binding	4.852143e-03
2	GO:0006094	gluconeogenesis	7.088189e-03
2	GO:0034599	cellular response to oxidative stress	1.901500e-02
2	GO:0046323	glucose import	3.221135e-02
2	GO:0000340	RNA 7-methylguanosine cap binding	3.221135e-02
2	GO:0051016	barbed-end actin filament capping	4.013873e-02

Table 5.3: Gene ontology terms associated with genes significantly down-regulated during the diauxic shift from clusters 3 and 4 from Figure 5.5, $P < 0.05$.

Cluster	Term	Term Name	P-Value
3	GO:0002181	cytoplasmic translation	2.328590e-06
3	GO:0005840	ribosome	1.649079e-05
3	GO:0003735	structural constituent of ribosome	4.736327e-05
3	GO:0022625	cytosolic large ribosomal subunit	1.838265e-04
3	GO:0006412	translation	2.055458e-04
3	GO:1904659	glucose transmembrane transport	3.070526e-04
3	GO:0015761	mannose transmembrane transport	3.070526e-04
3	GO:0015755	fructose transmembrane transport	3.070526e-04
3	GO:0098704	carbohydrate import across plasma membrane	3.070526e-04
3	GO:0005351	carbohydrate:proton symporter activity	3.070526e-04
3	GO:0005353	fructose transmembrane transporter activity	3.070526e-04
3	GO:0015149	hexose transmembrane transporter activity	3.070526e-04
3	GO:0015578	mannose transmembrane transporter activity	3.070526e-04
3	GO:0005355	glucose transmembrane transporter activity	3.070526e-04
3	GO:0055085	transmembrane transport	5.564942e-04
3	GO:0005886	plasma membrane	8.872409e-04
3	GO:0008643	carbohydrate transport	2.495324e-03
3	GO:0022857	transmembrane transporter activity	3.810879e-03
3	GO:0071944	cell periphery	4.946921e-03
3	GO:0005215	transporter activity	5.270063e-03
3	GO:0005634	nucleus	1.365578e-02
3	GO:0008645	hexose transmembrane transport	2.150518e-02
3	GO:0003746	translation elongation factor activity	2.924513e-02
3	GO:1902600	proton transmembrane transport	3.622409e-02
4	GO:0016021	integral component of membrane	5.195558e-10
4	GO:0016020	membrane	7.699885e-07
4	GO:0002181	cytoplasmic translation	3.090864e-06
4	GO:0022625	cytosolic large ribosomal subunit	1.547123e-05
4	GO:0003735	structural constituent of ribosome	1.683960e-04
4	GO:0005840	ribosome	9.070519e-04
4	GO:0005737	cytoplasm	9.185954e-04
4	GO:0000139	Golgi membrane	1.646644e-03
4	GO:0005783	endoplasmic reticulum	2.175216e-03
4	GO:0005524	ATP binding	3.952228e-03
4	GO:0055085	transmembrane transport	7.190739e-03
4	GO:0006412	translation	4.189781e-02

Table 5.4: Gene ontology terms associated with genes from cluster 5 from Figure 5.5, $P < 0.05$.

Cluster	Term	Term Name	P-Value
5	GO:0005739	mitochondrion	1.784191e-07
5	GO:0055114	oxidation-reduction process	2.820886e-05
5	GO:0003735	structural constituent of ribosome	3.471530e-04
5	GO:0005840	ribosome	3.807108e-04
5	GO:0005634	nucleus	1.005850e-03
5	GO:0016491	oxidoreductase activity	1.760415e-03
5	GO:0006281	DNA repair	4.826727e-03
5	GO:0006412	translation	5.203735e-03
5	GO:0006974	cellular response to DNA damage stimulus	7.110102e-03
5	GO:0002181	cytoplasmic translation	7.110102e-03
5	GO:0003677	DNA binding	7.110102e-03
5	GO:0007049	cell cycle	1.354622e-02
5	GO:0003824	catalytic activity	1.423408e-02
5	GO:0051301	cell division	4.409527e-02

Chapter 6

Summary

The work detailed in this dissertation describes how microfluidic technologies can be designed and applied to uncover dynamics-based regulatory processes in budding yeast. In Chapter 2, I described my work in developing single-cell microfluidic technologies for monitoring cell division and replicative aging in *S. cerevisiae*. In Chapter 3, I described how single-cell microfluidics was used to uncover the existence of metabolic oscillations in yeast. The fact that these metabolic cycles could be observed in the absence of cellular respiration highlights a key insight into their nature and function that may not be possible to obtain using the traditional chemostat-based approaches [105] typically used to study this phenomenon. Similarly, in Chapter 4, single-cell analysis of yeast during replicative aging revealed two different aging paths that were characterized by different patterns of rDNA silencing dynamics. These insights also would be very difficult to obtain with the classical yeast microdissection approach [53]. Finally, high-throughput microfluidics can offer an unprecedented look at gene expression dynamics during the diauxic shift, as described in Chapter 5. High-throughput microfluidic devices, such as the one described in Chapter 5, could be a useful technology in basic science by complementing omics style approaches in recording gene expression changes in dynamic environments, as well as in industry, where this device could be used as a real-time biosensor for a variety of applications.

My hope is that the microfluidic technologies that I have developed, as well as the scientific studies I have conducted to apply them, will be useful for a plethora of future studies. Such work could utilize these devices, or similar ones based off of their designs, to continue to reveal how the complex web of biological components present inside cells gives rise to the beauty and diversity of the natural world. Further, I hope that these insights can help point the way for designing interventions to improve human health.

Bibliography

[1] Rainer Breitling. What is systems biology? *Frontiers in physiology*, 1:159, 2010.

[2] Steven A Benner and A Michael Sismour. Synthetic biology. *Nature Reviews Genetics*, 6(7):533–543, 2005.

[3] Uri Alon. *An introduction to systems biology: design principles of biological circuits*. Chapman and Hall/CRC, 2006.

[4] Jeffrey D Orth, Ines Thiele, and Bernhard Ø Palsson. What is flux balance analysis? *Nature biotechnology*, 28(3):245–248, 2010.

[5] Bernhard Ø Palsson. *Systems biology: properties of reconstructed networks*. Cambridge university press, 2006.

[6] Jonathan R Karr, Jayodita C Sanghvi, Derek N Macklin, Miriam V Gutschow, Jared M Jacobs, Benjamin Bolival Jr, Nacyra Assad-Garcia, John I Glass, and Markus W Covert. A whole-cell computational model predicts phenotype from genotype. *Cell*, 150(2):389–401, 2012.

[7] Markus W Covert. *Fundamentals of systems biology: from synthetic circuits to whole-cell models*. CRC Press, 2015.

[8] Timothy S Gardner, Charles R Cantor, and James J Collins. Construction of a genetic toggle switch in escherichia coli. *Nature*, 403(6767):339–342, 2000.

[9] Michael B Elowitz and Stanislas Leibler. A synthetic oscillatory network of transcriptional regulators. *Nature*, 403(6767):335–338, 2000.

[10] Jesse Stricker, Scott Cookson, Matthew R Bennett, William H Mather, Lev S Tsimring, and Jeff Hasty. A fast, robust and tunable synthetic gene oscillator. *Nature*, 456(7221):516–519, 2008.

[11] Tal Danino, Octavio Mondragón-Palomino, Lev Tsimring, and Jeff Hasty. A synchronized quorum of genetic clocks. *Nature*, 463(7279):326–330, 2010.

[12] Alvin Tamsir, Jeffrey J Tabor, and Christopher A Voigt. Robust multicellular computing using genetically encoded nor gates and chemical 'wires'. *Nature*, 469(7329):212–215, 2011.

[13] Tae Seok Moon, Chunbo Lou, Alvin Tamsir, Brynne C Stanton, and Christopher A Voigt. Genetic programs constructed from layered logic gates in single cells. *Nature*, 491(7423):249–253, 2012.

[14] Dae-Kyun Ro, Eric M Paradise, Mario Ouellet, Karl J Fisher, Karyn L Newman, John M Ndungu, Kimberly A Ho, Rachel A Eachus, Timothy S Ham, James Kirby, et al. Production of the antimalarial drug precursor artemisinic acid in engineered yeast. *Nature*, 440(7086):940–943, 2006.

[15] Stephanie Galanie, Kate Thodey, Isis J Trenchard, Maria Filsinger Interrante, and Christina D Smolke. Complete biosynthesis of opioids in yeast. *Science*, 349(6252):1095–1100, 2015.

[16] Le Cong, F Ann Ran, David Cox, Shuailiang Lin, Robert Barretto, Naomi Habib, Patrick D Hsu, Xuebing Wu, Wenyan Jiang, Luciano A Marraffini, et al. Multiplex genome engineering using crispr/cas systems. *Science*, 339(6121):819–823, 2013.

[17] Martin Jinek, Krzysztof Chylinski, Ines Fonfara, Michael Hauer, Jennifer A Doudna, and Emmanuelle Charpentier. A programmable dual-rna–guided dna endonuclease in adaptive bacterial immunity. *science*, 337(6096):816–821, 2012.

[18] Prashant Mali, Luhan Yang, Kevin M Esvelt, John Aach, Marc Guell, James E DiCarlo, Julie E Norville, and George M Church. Rna-guided human genome engineering via cas9. *Science*, 339(6121):823–826, 2013.

[19] Daniel G Gibson, John I Glass, Carole Lartigue, Vladimir N Noskov, Ray-Yuan Chuang, Mikkel A Algire, Gwynedd A Benders, Michael G Montague, Li Ma, Monzia M Moodie, et al. Creation of a bacterial cell controlled by a chemically synthesized genome. *science*, 329(5987):52–56, 2010.

[20] Yangyang Shao, Ning Lu, Zhenfang Wu, Chen Cai, Shanshan Wang, Ling-Li Zhang, Fan Zhou, Shijun Xiao, Lin Liu, Xiaofei Zeng, et al. Creating a functional single-chromosome yeast. *Nature*, 560(7718):331–335, 2018.

[21] Brian Munsky, Karen Tkach Tuzman, Dirk Fey, Maciej Dobrzynski, Boris N Kholodenko, Sarah Olson, Jianjun Huang, Zachary Fox, Abhyudai Singh, Ramon Grima, et al. *Quantitative biology: theory, computational methods, and models*. The MIT Press, 2018.

[22] Matthew R Bennett and Jeff Hasty. Microfluidic devices for measuring gene network dynamics in single cells. *Nature Reviews Genetics*, 10(9):628, 2009.

[23] MS Ferry, IA Razinkov, and J Hasty. Microfluidics for synthetic biology: from design to execution. *Methods in enzymology*, 497:295, 2011.

[24] Gürol M Süel, Jordi Garcia-Ojalvo, Louisa M Liberman, and Michael B Elowitz. An excitable gene regulatory circuit induces transient cellular differentiation. *Nature*, 440(7083):545–550, 2006.

[25] Gürol M Süel, Rajan P Kulkarni, Jonathan Dworkin, Jordi Garcia-Ojalvo, and Michael B Elowitz. Tunability and noise dependence in differentiation dynamics. *Science*, 315(5819):1716–1719, 2007.

[26] Nan Hao and Erin K O'shea. Signal-dependent dynamics of transcription factor translocation controls gene expression. *Nature structural & molecular biology*, 19(1):31, 2012.

[27] Zohreh AkhavanAghdam, Joydeb Sinha, Omar P Tabbaa, and Nan Hao. Dynamic control of gene regulatory logic by seemingly redundant transcription factors. *Elife*, 5:e18458, 2016.

[28] Lacramioara Bintu, John Yong, Yaron E Antebi, Kayla McCue, Yasuhiro Kazuki, Narumi Uno, Mitsuo Oshimura, and Michael B Elowitz. Dynamics of epigenetic regulation at the single-cell level. *Science*, 351(6274):720–724, 2016.

[29] Michael B Elowitz, Arnold J Levine, Eric D Siggia, and Peter S Swain. Stochastic gene expression in a single cell. *Science*, 297(5584):1183–1186, 2002.

[30] Bruno MC Martins and James CW Locke. Microbial individuality: how single-cell heterogeneity enables population level strategies. *Current opinion in microbiology*, 24:104–112, 2015.

[31] Edward R Sumner and Simon V Avery. Phenotypic heterogeneity: differential stress resistance among individual cells of the yeast saccharomyces cerevisiae. *Microbiology*, 148(2):345–351, 2002.

[32] Andriy Marusyk, Vanessa Almendro, and Kornelia Polyak. Intra-tumour heterogeneity: a looking glass for cancer? *Nature Reviews Cancer*, 12(5):323–334, 2012.

[33] Tsung-li Liu, Srigokul Upadhyayula, Daniel E Milkie, Ved Singh, Kai Wang, Ian A Swinburne, Kishore R Mosaliganti, Zach M Collins, Tom W Hiscock, Jamien Shea, et al. Observing the cell in its native state: Imaging subcellular dynamics in multicellular organisms. *Science*, 360(6386):eaaq1392, 2018.

[34] Allon M Klein, Linas Mazutis, Ilke Akartuna, Naren Tallapragada, Adrian Veres, Victor Li, Leonid Peshkin, David A Weitz, and Marc W Kirschner. Droplet barcoding for single-cell transcriptomics applied to embryonic stem cells. *Cell*, 161(5):1187–1201, 2015.

[35] Evan Z Macosko, Anindita Basu, Rahul Satija, James Nemesh, Karthik Shekhar, Melissa Goldman, Itay Tirosh, Allison R Bialas, Nolan Kamitaki, Emily M Martersteck, et al. Highly parallel genome-wide expression profiling of individual cells using nanoliter droplets. *Cell*, 161(5):1202–1214, 2015.

[36] Ce Zhang, Hsiung-Lin Tu, Gengjie Jia, Tanzila Mukhtar, Verdon Taylor, Andrey Rzhetsky, and Savaş Tay. Ultra-multiplexed analysis of single-cell dynamics reveals logic rules in differentiation. *Science Advances*, 5(4):eaav7959, 2019.

[37] Aaron McKenna, Gregory M Findlay, James A Gagnon, Marshall S Horwitz, Alexander F Schier, and Jay Shendure. Whole-organism lineage tracing by combinatorial and cumulative genome editing. *Science*, 353(6298):aaf7907, 2016.

[38] Kirsten L Frieda, James M Linton, Sahand Hormoz, Joonhyuk Choi, Ke-Huan K Chow, Zakary S Singer, Mark W Budde, Michael B Elowitz, and Long Cai. Synthetic recording and in situ readout of lineage information in single cells. *Nature*, 541(7635):107, 2017.

[39] Brian K Kennedy, Shelley L Berger, Anne Brunet, Judith Campisi, Ana Maria Cuervo, Elissa S Epel, Claudio Franceschi, Gordon J Lithgow, Richard I Morimoto, Jeffrey E Pessin, et al. Geroscience: linking aging to chronic disease. *Cell*, 159(4):709–713, 2014.

[40] Matt Kaeberlein. Translational geroscience: A new paradigm for 21st century medicine. *Translational Medicine of Aging*, 1:1–4, 2017.

[41] Ana M Valdes, Daniel Glass, and Tim D Spector. Omics technologies and the study of human ageing. *Nature Reviews Genetics*, 14(9):601, 2013.

[42] Judith Campisi, Pankaj Kapahi, Gordon J Lithgow, Simon Melov, John C Newman, and Eric Verdin. From discoveries in ageing research to therapeutics for healthy ageing. *Nature*, 571(184):183–192, 2019.

[43] Luigi Fontana, Linda Partridge, and Valter D Longo. Extending healthy life span—from yeast to humans. *science*, 328(5976):321–326, 2010.

[44] Valter D Longo and Brian K Kennedy. Sirtuins in aging and age-related disease. *Cell*, 126(2):257–268, 2006.

[45] Brian M Wasko and Matt Kaeberlein. Yeast replicative aging: a paradigm for defining conserved longevity interventions. *FEMS yeast research*, 14(1):148–159, 2014.

[46] Matt Kaeberlein and Brian K Kennedy. Large-scale identification in yeast of conserved ageing genes. *Mechanisms of ageing and development*, 126(1):17–21, 2005.

[47] Chong He, Chuankai Zhou, and Brian K Kennedy. The yeast replicative aging model. *Biochimica et Biophysica Acta (BBA)-Molecular Basis of Disease*, 1864(9):2690–2696, 2018.

[48] Erica D Smith, Mitsuhiro Tsuchiya, Lindsay A Fox, Nick Dang, Di Hu, Emily O Kerr, Elijah D Johnston, Bie N Tchao, Diana N Pak, K Linnea Welton, et al. Quantitative evidence for conserved longevity pathways between divergent eukaryotic species. *Genome research*, 18(4):564–570, 2008.

[49] Konrad T Howitz, Kevin J Bitterman, Haim Y Cohen, Dudley W Lamming, Siva Lavu, Jason G Wood, Robert E Zipkin, Phuong Chung, Anne Kisielewski, Li-Li Zhang, et al. Small molecule activators of sirtuins extend saccharomyces cerevisiae lifespan. *Nature*, 425(6954):191, 2003.

[50] Valter D Longo, Gerald S Shadel, Matt Kaeberlein, and Brian Kennedy. Replicative and chronological aging in saccharomyces cerevisiae. *Cell metabolism*, 16(1):18–31, 2012.

[51] Robert K Mortimer and John R Johnston. Life span of individual yeast cells. 1958.

[52] Todd A Duncombe, Augusto M Tentori, and Amy E Herr. Microfluidics: reframing biological enquiry. *Nature Reviews Molecular Cell Biology*, 16(9):554, 2015.

[53] Kristan K Steffen, Brian K Kennedy, and Matt Kaeberlein. Measuring replicative life span in the budding yeast. *JoVE (Journal of Visualized Experiments)*, (28):e1209, 2009.

[54] Sung Sik Lee, Ima Avalos Vizcarra, Daphne HEW Huberts, Luke P Lee, and Matthias Heinemann. Whole lifespan microscopic observation of budding yeast aging through a microfluidic dissection platform. *Proceedings of the National Academy of Sciences*, 109(13):4916–4920, 2012.

[55] Zhengwei Xie, Yi Zhang, Ke Zou, Onn Brandman, Chunxiong Luo, Qi Ouyang, and Hao Li. Molecular phenotyping of aging in single yeast cells using a novel microfluidic device. *Aging cell*, 11(4):599–606, 2012.

[56] James Ryley and Olivia M Pereira-Smith. Microfluidics device for single cell gene expression analysis in saccharomyces cerevisiae. *Yeast*, 23(14-15):1065–1073, 2006.

[57] Anders S Hansen, Nan Hao, and Erin K O'shea. High-throughput microfluidics to control and measure signaling dynamics in single yeast cells. *Nature protocols*, 10(8):1181, 2015.

[58] Scott Cookson, Natalie Ostroff, Wyming Lee Pang, Dmitri Volfson, and Jeff Hasty. Monitoring dynamics of single-cell gene expression over multiple cell cycles. *Molecular Systems Biology*, 1(1), 2005.

[59] Bridget L Baumgartner, Richard O'Laughlin, Meng Jin, Lev S Tsimring, Nan Hao, and Jeff Hasty. Flavin-based metabolic cycles are integral features of growth and division in single yeast cells. *Scientific reports*, 8(1):18045, 2018.

[60] Matthew M Crane and Matt Kaeberlein. The paths of mortality: how understanding the biology of aging can help explain systems behavior of single cells. *Current opinion in systems biology*, 8:25–31, 2018.

[61] Fred Sherman. Getting started with yeast. In *Methods in enzymology*, volume 350, pages 3–41. Elsevier, 2002.

[62] Matt Kaeberlein, R Wilson Powers, Kristan K Steffen, Eric A Westman, Di Hu, Nick Dang, Emily O Kerr, Kathryn T Kirkland, Stanley Fields, and Brian K Kennedy. Regulation of yeast replicative life span by tor and sch9 in response to nutrients. *Science*, 310(5751):1193–1196, 2005.

[63] Yi Zhang, Chunxiong Luo, Ke Zou, Zhengwei Xie, Onn Brandman, Qi Ouyang, and Hao Li. Single cell analysis of yeast replicative aging using a new generation of microfluidic device. *PloS one*, 7(11):e48275, 2012.

[64] Steffen Fehrmann, Camille Paoletti, Youlian Goulev, Andrei Ungureanu, Hugo Aguilaniu, and Gilles Charvin. Aging yeast cells undergo a sharp entry into senescence unrelated to the loss of mitochondrial membrane potential. *Cell reports*, 5(6):1589–1599, 2013.

[65] Matthew M Crane, Ivan BN Clark, Elco Bakker, Stewart Smith, and Peter S Swain. A microfluidic system for studying ageing and dynamic single-cell responses in budding yeast. *PloS one*, 9(6):e100042, 2014.

[66] Myeong Chan Jo, Wei Liu, Liang Gu, Weiwei Dang, and Lidong Qin. High-throughput analysis of yeast replicative aging using a microfluidic system. *Proceedings of the National Academy of Sciences*, 112(30):9364–9369, 2015.

[67] Ping Liu, Thomas Z Young, and Murat Acar. Yeast replicator: A high-throughput multiplexed microfluidics platform for automated measurements of single-cell aging. *Cell reports*, 13(3):634–644, 2015.

[68] Yang Li, Meng Jin, Richard O'Laughlin, Philip Bittihn, Lev S Tsimring, Lorraine Pillus, Jeff Hasty, and Nan Hao. Multigenerational silencing dynamics control cell aging. *Proceedings of the National Academy of Sciences*, page 201703379, 2017.

[69] Ethan A Sarnoski, Ruijie Song, Ege Ertekin, Noelle Koonce, and Murat Acar. Fundamental characteristics of single-cell aging in diploid yeast. *iScience*, 7:96–109, 2018.

[70] Leland H Hartwell and Michael W Unger. Unequal division in saccharomyces cerevisiae and its implications for the control of cell division. *The Journal of cell biology*, 75(2):422–435, 1977.

[71] Brian K Kennedy, Nicanor R Austriaco, and Leonard Guarente. Daughter cells of saccharomyces cerevisiae from old mothers display a reduced life span. *The Journal of cell biology*, 127(6):1985–1993, 1994.

[72] Wei-Heong Tan and Shoji Takeuchi. A trap-and-release integrated microfluidic system for dynamic microarray applications. *Proceedings of the national academy of sciences*, 104(4):1146–1151, 2007.

[73] Dino Di Carlo, Nima Aghdam, and Luke P Lee. Single-cell enzyme concentrations, kinetics, and inhibition analysis using high-density hydrodynamic cell isolation arrays. *Analytical chemistry*, 78(14):4925–4930, 2006.

[74] Vigneswaran Narayanamurthy, Sairam Nagarajan, Fahmi Samsuri, TM Sridhar, et al. Microfluidic hydrodynamic trapping for single cell analysis: mechanisms, methods and applications. *Analytical Methods*, 9(25):3751–3772, 2017.

[75] Mengsu Yang, Cheuk-Wing Li, and Jun Yang. Cell docking and on-chip monitoring of cellular reactions with a controlled concentration gradient on a microfluidic device. *Analytical chemistry*, 74(16):3991–4001, 2002.

[76] Amelia Ahmad Khalili, Mohd Ahmad, Masaru Takeuchi, Masahiro Nakajima, Yasuhisa Hasegawa, and Razauden Mohamed Zulkifli. A microfluidic device for hydrodynamic trapping and manipulation platform of a single biological cell. *Applied Sciences*, 6(2):40, 2016.

[77] Di Jin, Bin Deng, JX Li, W Cai, L Tu, J Chen, Q Wu, and WH Wang. A microfluidic device enabling high-efficiency single cell trapping. *Biomicrofluidics*, 9(1):014101, 2015.

[78] Georges E Janssens and Liesbeth M Veenhoff. The natural variation in lifespans of single yeast cells is related to variation in cell size, ribosomal protein, and division time. *PloS one*, 11(12):e0167394, 2016.

[79] Tod Smeal, James Claus, Brian Kennedy, Francesca Cole, and Leonard Guarente. Loss of transcriptional silencing causes sterility in old mother cells of s. cerevisiae. *Cell*, 84(4):633–642, 1996.

[80] Peter U Park, Mitch Mcvey, and Leonard Guarente. Separation of mother and daughter cells. In *Methods in enzymology*, volume 351, pages 468–477. Elsevier, 2002.

[81] Jing Yang, Mark A McCormick, Jiashun Zheng, Zhengwei Xie, Mitsuhiro Tsuchiya, Scott Tsuchiyama, Hana El-Samad, Qi Ouyang, Matt Kaeberlein, Brian K Kennedy, et al. Systematic analysis of asymmetric partitioning of yeast proteome between mother and daughter cells reveals "aging factors" and mechanism of lifespan asymmetry. *Proceedings of the National Academy of Sciences*, 112(38):11977–11982, 2015.

[82] Meng Jin, Yang Li, Richard O'Laughlin, Philip Bittihn, Lorraine Pillus, Lev S Tsimring, Jeff Hasty, and Nan Hao. Divergent aging of isogenic yeast cells revealed through single-cell phenotypic dynamics. *Cell systems*, 2019.

[83] Kenneth L Chen, Matthew M Crane, and Matt Kaeberlein. Microfluidic technologies for yeast replicative lifespan studies. *Mechanisms of ageing and development*, 161:262–269, 2017.

[84] Mark A McCormick, Joe R Delaney, Mitsuhiro Tsuchiya, Scott Tsuchiyama, Anna Shemorry, Sylvia Sim, Annie Chia-Zong Chou, Umema Ahmed, Daniel Carr, Christopher J Murakami, et al. A comprehensive analysis of replicative lifespan in 4,698 single-gene deletion strains uncovers conserved mechanisms of aging. *Cell metabolism*, 22(5):895–906, 2015.

[85] Yang Li, Yanfei Jiang, Julie Paxman, Richard O'Laughlin, Lorraine Pillus, Lev S Tsimring, Jeff Hasty, and Nan Hao. An epigenetic landscape governs early fate decision in cellular aging. *bioRxiv*, page 630921, 2019.

[86] Matt Kaeberlein, Mitch McVey, and Leonard Guarente. The sir2/3/4 complex and sir2 alone promote longevity in saccharomyces cerevisiae by two different mechanisms. *Genes & development*, 13(19):2570–2580, 1999.

[87] Susan L Forsburg and Leonard Guarente. Identification and characterization of hap4: a third component of the ccaat-bound hap2/hap3 heteromer. *Genes & development*, 3(8):1166–1178, 1989.

[88] Deborah Bell-Pedersen, Vincent M Cassone, David J Earnest, Susan S Golden, Paul E Hardin, Terry L Thomas, and Mark J Zoran. Circadian rhythms from multiple oscillators: lessons from diverse organisms. *Nature Reviews Genetics*, 6:544–556, 2005.

[89] Jintao Liu, Rosa Martinez-Corral, Arthur Prindle, D Lee Dong-yeon, Joseph Larkin, Marçal Gabalda-Sagarra, Jordi Garcia-Ojalvo, and Gürol M Süel. Coupling between distant biofilms and emergence of nutrient time-sharing. *Science*, 356(6338):638–642, 2017.

[90] Renato E Mirollo and Steven H Strogatz. Synchronization of pulse-coupled biological oscillators. *SIAM Journal on Applied Mathematics*, 50(6):1645–1662, 1990.

[91] Katherine C Chen, Laurence Calzone, Attila Csikasz-Nagy, Frederick R Cross, Bela Novak, and John J Tyson. Integrative analysis of cell cycle control in budding yeast. *Molecular biology of the cell*, 15:3841–3862, 2004.

[92] Hiromi Hirata, Shigeki Yoshiura, Toshiyuki Ohtsuka, Yasumasa Bessho, Takahiro Harada, Kenichi Yoshikawa, and Ryoichiro Kageyama. Oscillatory expression of the bhlh factor hes1 regulated by a negative feedback loop. *Science*, 298:840–843, 2002.

[93] Galit Lahav, Nitzan Rosenfeld, Alex Sigal, Naama Geva-Zatorsky, Arnold J Levine, Michael B Elowitz, and Uri Alon. Dynamics of the p53-mdm2 feedback loop in individual cells. *Nature genetics*, 36(2):147–150, 2004.

[94] James E Ferrell, Tony Yu-Chen Tsai, and Qiong Yang. Modeling the cell cycle: why do certain circuits oscillate? *Cell*, 144(6):874–885, 2011.

[95] Anna-Karin Gustavsson, David D van Niekerk, Caroline B Adiels, Franco B du Preez, Mattias Goksör, and Jacky L Snoep. Sustained glycolytic oscillations in individual isolated yeast cells. *The FEBS journal*, 279(16):2837–2847, 2012.

[96] Benjamin JT Dodd and Joel M Kralj. Live cell imaging reveals ph oscillations in saccharomyces cerevisiae during metabolic transitions. *Scientific Reports*, 7(1):13922, 2017.

[97] Benjamin P Tu and Steven L McKnight. Metabolic cycles as an underlying basis of biological oscillations. *Nature reviews Molecular cell biology*, 7(9):696–701, 2006.

[98] Ling Cai and Benjamin P Tu. Driving the cell cycle through metabolism. *Annual review of cell and developmental biology*, 28:59–87, 2012.

[99] Alexandros Papagiannakis, Bastian Niebel, Ernst C Wit, and Matthias Heinemann. Autonomous metabolic oscillations robustly gate the early and late cell cycle. *Molecular cell*, 65(2):285–295, 2017.

[100] John S O'Neill and Akhilesh B Reddy. Circadian clocks in human red blood cells. *Nature*, 469(7331):498–503, 2011.

[101] Mian Zhou, Wei Wang, Sargis Karapetyan, Musoki Mwimba, Jorge Marqués, Nicolas E Buchler, and Xinnian Dong. Redox rhythm reinforces the circadian clock to gate immune response. *Nature*, 523(7561):472–476, 2015.

[102] RK Finn and RE Wilson. Fermentation process control, population dynamics of a continuous propagator for microorganisms. *Journal of Agricultural and Food Chemistry*, 2(2):66–69, 1954.

[103] Martin T Küenzi and Armin Fiechter. Changes in carbohydrate composition and trehalase-activity during the budding cycle of saccharomyces cerevisiae. *Archives of Microbiology*, 64(4):396–407, 1969.

[104] Aidar D Satroutdinov, Hiroshi Kuriyama, and Harumi Kobayashi. Oscillatory metabolism of saccharomyces cerevisiae in continuous culture. *FEMS microbiology letters*, 98(1-3):261–267, 1992.

[105] Benjamin P Tu, Andrzej Kudlicki, Maga Rowicka, and Steven L McKnight. Logic of the yeast metabolic cycle: temporal compartmentalization of cellular processes. *Science*, 310(5751):1152–1158, 2005.

[106] Kalesh Sasidharan, Masaru Tomita, Miguel Aon, David Lloyd, and Douglas B Murray. Time-structure of the yeast metabolism in vivo. In *Advances in Systems Biology*, pages 359–379. Springer, 2012.

[107] Benjamin P Tu, Rachel E Mohler, Jessica C Liu, Kenneth M Dombek, Elton T Young, Robert E Synovec, and Steven L McKnight. Cyclic changes in metabolic state during the life of a yeast cell. *Proceedings of the National Academy of Sciences*, 104(43):16886–16891, 2007.

[108] Douglas B Murray, Manfred Beckmann, and Hiroaki Kitano. Regulation of yeast oscillatory dynamics. *Proceedings of the National Academy of Sciences*, 104(7):2241–2246, 2007.

[109] Helen C Causton, Kevin A Feeney, Christine A Ziegler, and John S O'Neill. Metabolic cycles in yeast share features conserved among circadian rhythms. *Current Biology*, 25(8):1056–1062, 2015.

[110] Anthony J Burnetti, Mert Aydin, and Nicolas E Buchler. Cell cycle start is coupled to entry into the yeast metabolic cycle across diverse strains and growth rates. *Molecular biology of the cell*, 27(1):64–74, 2016.

[111] Allan K Poulsen, Mai Østergaard Petersen, and Lars Folke Olsen. Single cell studies and simulation of cell–cell interactions using oscillating glycolysis in yeast cells. *Biophysical chemistry*, 125(2):275–280, 2007.

[112] Anna-Karin Gustavsson, David D Niekerk, Caroline B Adiels, Bob Kooi, Mattias Goksör, and Jacky L Snoep. Allosteric regulation of phosphofructokinase controls the emergence of glycolytic oscillations in isolated yeast cells. *The FEBS journal*, 281(12):2784–2793, 2014.

[113] Anna-Karin Gustavsson, David D van Niekerk, Caroline B Adiels, Mattias Goksör, and Jacky L Snoep. Heterogeneity of glycolytic oscillatory behaviour in individual yeast cells. *FEBS letters*, 588(1):3–7, 2014.

[114] Sunil Laxman, Benjamin M Sutter, and Benjamin P Tu. Behavior of a metabolic cycling population at the single cell level as visualized by fluorescent gene expression reporters. *PloS one*, 5(9):e12595, 2010.

[115] Sanford J Silverman, Allegra A Petti, Nikolai Slavov, Lance Parsons, Ryan Briehof, Stephan Y Thiberge, Daniel Zenklusen, Saumil J Gandhi, Daniel R Larson, Robert H Singer, et al. Metabolic cycling in single yeast cells from unsynchronized steady-state populations limited on glucose or phosphate. *Proceedings of the National Academy of Sciences*, 107(15):6946–6951, 2010.

[116] Nikolai Slavov, Joanna Macinskas, Amy Caudy, and David Botstein. Metabolic cycling without cell division cycling in respiring yeast. *Proceedings of the National Academy of Sciences*, 108(47):19090–19095, 2011.

[117] J Brian Robertson, Chris C Stowers, Erik Boczko, and Carl Hirschie Johnson. Real-time luminescence monitoring of cell-cycle and respiratory oscillations in yeast. *Proceedings of the National Academy of Sciences*, 105(46):17988–17993, 2008.

[118] Nirmala Ramanujam. Fluorescence spectroscopy of neoplastic and non-neoplastic tissues. *Neoplasia*, 2(1-2):89–117, 2000.

[119] Irene Georgakoudi and Kyle P Quinn. Optical imaging using endogenous contrast to assess metabolic state. *Annual review of biomedical engineering*, 14:351–367, 2012.

[120] Caroline A Schneider, Wayne S Rasband, and Kevin W Eliceiri. Nih image to imagej: 25 years of image analysis. *Nature methods*, 9(7):671–675, 2012.

[121] Robertus AM de Bruin, W Hayes McDonald, Tatyana I Kalashnikova, John Yates, and Curt Wittenberg. Cln3 activates g1-specific transcription via phosphorylation of the sbf bound repressor whi5. *Cell*, 117(7):887–898, 2004.

[122] Boris Magasanik and Chris A Kaiser. Nitrogen regulation in saccharomycescerevisiae. *Gene*, 290(1):1–18, 2002.

[123] Vittoria Zinzalla, Michele Graziola, Andrea Mastriani, Marco Vanoni, and Lilia Alberghina. Rapamycin-mediated g1 arrest involves regulation of the cdk inhibitor sic1 in saccharomyces cerevisiae. *Molecular microbiology*, 63(5):1482–1494, 2007.

[124] David Lloyd, L Eshantha, J Salgado, Michael P Turner, and Douglas B Murray. Respiratory oscillations in yeast: clock-driven mitochondrial cycles of energization. *FEBS letters*, 519(1-3):41–44, 2002.

[125] David Lloyd, Katey M Lemar, L Eshantha J Salgado, Timothy M Gould, and Douglas B Murray. Respiratory oscillations in yeast: mitochondrial reactive oxygen species, apoptosis and time; a hypothesis. *FEMS yeast research*, 3(4):333–339, 2003.

[126] David Lloyd. Respiratory oscillations in yeasts. In *Cellular Oscillatory Mechanisms*, pages 118–140. Springer, 2008.

[127] Misook Uh, Deborah Jones, and David M Mueller. The gene coding for the yeast oligomycin sensitivity-conferring protein. *Journal of Biological Chemistry*, 265(31):19047–19052, 1990.

[128] Jane C Schneider and Leonard Guarente. Regulation of the yeast cyt1 gene encoding cytochrome c1 by hap1 and hap2/3/4. *Molecular and Cellular Biology*, 11(10):4934–4942, 1991.

[129] Kai Stefan Dimmer, Stefan Fritz, Florian Fuchs, Marlies Messerschmitt, Nadja Weinbach, Walter Neupert, and Benedikt Westermann. Genetic basis of mitochondrial function and morphology insaccharomyces cerevisiae. *Molecular biology of the cell*, 13(3):847–853, 2002.

[130] Young-Yon Kwon, Kyung-Mi Choi, ChangYeon Cho, and Cheol-Koo Lee. Mitochondrial efficiency-dependent viability of saccharomyces cerevisiae mutants carrying individual electron transport chain component deletions. *Molecules and cells*, 38(12):1054, 2015.

[131] André B Canelas, Nicola Harrison, Alessandro Fazio, Jie Zhang, Juha-Pekka Pitkänen, Joost Van den Brink, Barbara M Bakker, Lara Bogner, Jildau Bouwman, Juan I Castrillo, et al. Integrated multilaboratory systems biology reveals differences in protein metabolism between two reference yeast strains. *Nature communications*, 1(9):145, 2010.

[132] Jane Mellor. The molecular basis of metabolic cycles and their relationship to circadian rhythms. *Nature structural & molecular biology*, 23(12):1035–1044, 2016.

[133] Gavin Schlissel, Marek K Krzyzanowski, Fabrice Caudron, Yves Barral, and Jasper Rine. Aggregation of the whi3 protein, not loss of heterochromatin, causes sterility in old yeast cells. *Science*, 355(6330):1184–1187, 2017.

[134] Ping Liu, Ruijie Song, Gregory L Elison, Weilin Peng, and Murat Acar. Noise reduction as an emergent property of single-cell aging. *Nature communications*, 8(1):680, 2017.

[135] Christophe Dez and David Tollervey. Ribosome synthesis meets the cell cycle. *Current opinion in microbiology*, 7(6):631–637, 2004.

[136] Long Cai, Chiraj K Dalal, and Michael B Elowitz. Frequency-modulated nuclear localization bursts coordinate gene regulation. *Nature*, 455(7212):485, 2008.

[137] Kristen M Thyng, Chad A Greene, Robert D Hetland, Heather M Zimmerle, and Steven F DiMarco. True colors of oceanography: Guidelines for effective and accurate colormap selection. *Oceanography*, 29(3):9–13, 2016.

[138] Michael A McMurray and Daniel E Gottschling. Aging and genetic instability in yeast. *Current opinion in microbiology*, 7(6):673–679, 2004.

[139] Carlos López-Otín, Maria A Blasco, Linda Partridge, Manuel Serrano, and Guido Kroemer. The hallmarks of aging. *Cell*, 153(6):1194–1217, 2013.

[140] Jeremy E Purvis and Galit Lahav. Encoding and decoding cellular information through signaling dynamics. *Cell*, 152(5):945–956, 2013.

[141] Marcelo Behar and Alexander Hoffmann. Understanding the temporal codes of intracellular signals. *Current opinion in genetics & development*, 20(6):684–693, 2010.

[142] Joe H Levine, Yihan Lin, and Michael B Elowitz. Functional roles of pulsing in genetic circuits. *Science*, 342(6163):1193–1200, 2013.

[143] KA Steinkraus, Matt Kaeberlein, and Brian K Kennedy. Replicative aging in yeast: the means to the end. *Annual review of cell and developmental biology*, 24:29–54, 2008.

[144] Jan Vijg and Yousin Suh. Genome instability and aging. *Annual review of physiology*, 75:645–668, 2013.

[145] Marc R Gartenberg and Jeffrey S Smith. The nuts and bolts of transcriptionally silent chromatin in saccharomyces cerevisiae. *Genetics*, 203(4):1563–1599, 2016.

[146] Kimiko Saka, Satoru Ide, Austen RD Ganley, and Takehiko Kobayashi. Cellular senescence in yeast is regulated by rdna noncoding transcription. *Current Biology*, 23(18):1794–1798, 2013.

[147] Derek L Lindstrom, Christina K Leverich, Kiersten A Henderson, and Daniel E Gottschling. Replicative age induces mitotic recombination in the ribosomal rna gene cluster of saccharomyces cerevisiae. *PLoS genetics*, 7(3), 2011.

[148] David A Sinclair and Leonard Guarente. Extrachromosomal rdna circles—a cause of aging in yeast. *Cell*, 91(7):1033–1042, 1997.

[149] Kevin J Bitterman, Rozalyn M Anderson, Haim Y Cohen, Magda Latorre-Esteves, and David A Sinclair. Inhibition of silencing and accelerated aging by nicotinamide, a putative negative regulator of yeast sir2 and human sirt1. *Journal of Biological Chemistry*, 277(47):45099–45107, 2002.

[150] Eugenia Y Xu, Karl A Zawadzki, and James R Broach. Single-cell observations reveal intermediate transcriptional silencing states. *Molecular cell*, 23(2):219–229, 2006.

[151] Anne E Dodson and Jasper Rine. Heritable capture of heterochromatin dynamics in saccharomyces cerevisiae. *Elife*, 4:e05007, 2015.

[152] Zheng Hu, Kaifu Chen, Zheng Xia, Myrriah Chavez, Sangita Pal, Ja-Hwan Seol, Chin-Chuan Chen, Wei Li, and Jessica K Tyler. Nucleosome loss leads to global transcriptional up-regulation and genomic instability during yeast aging. *Genes & development*, 28(4):396–408, 2014.

[153] Weiwei Dang, Kristan K Steffen, Rocco Perry, Jean A Dorsey, F Brad Johnson, Ali Shilatifard, Matt Kaeberlein, Brian K Kennedy, and Shelley L Berger. Histone h4 lysine 16 acetylation regulates cellular lifespan. *Nature*, 459(7248):802, 2009.

[154] Mark A McCormick, Amanda G Mason, Stephan J Guyenet, Weiwei Dang, Renee M Garza, Marc K Ting, Rick M Moller, Shelley L Berger, Matt Kaeberlein, Lorraine Pillus, et al. The saga histone deubiquitinase module controls yeast replicative lifespan via sir2 interaction. *Cell reports*, 8(2):477–486, 2014.

[155] Charles Evans, Katrina L Bogan, Peng Song, Charles F Burant, Robert T Kennedy, and Charles Brenner. Nad+ metabolite levels as a function of vitamins and calorie restriction: evidence for different mechanisms of longevity. *BMC chemical biology*, 10(1):2, 2010.

[156] Rozalyn M Anderson, Kevin J Bitterman, Jason G Wood, Oliver Medvedik, and David A Sinclair. Nicotinamide and pnc1 govern lifespan extension by calorie restriction in saccharomyces cerevisiae. *Nature*, 423(6936):181–185, 2003.

[157] Szu-Chieh Mei and Charles Brenner. Calorie restriction-mediated replicative lifespan extension in yeast is non-cell autonomous. *PLoS biology*, 13(1), 2015.

[158] Aisha Ellahi, Deborah M Thurtle, and Jasper Rine. The chromatin and transcriptional landscape of native saccharomyces cerevisiae telomeres and subtelomeric domains. *Genetics*, 200(2):505–521, 2015.

[159] Mingguang Li, Veena Valsakumar, Kunal Poorey, Stefan Bekiranov, and Jeffrey S Smith. Genome-wide analysis of functional sirtuin chromatin targets in yeast. *Genome biology*, 14(5):R48, 2013.

[160] Georges E Janssens, Anne C Meinema, Javier Gonzalez, Justina C Wolters, Alexander Schmidt, Victor Guryev, Rainer Bischoff, Ernst C Wit, Liesbeth M Veenhoff, and Matthias

Heinemann. Protein biogenesis machinery is a driver of replicative aging in yeast. *Elife*, 4:e08527, 2015.

[161] Danesh Moazed, Amy Kistler, Amy Axelrod, Jasper Rine, and Alexander D Johnson. Silent information regulator protein complexes in saccharomyces cerevisiae: a sir2/sir4 complex and evidence for a regulatory domain in sir4 that inhibits its interaction with sir3. *Proceedings of the National Academy of Sciences*, 94(6):2186–2191, 1997.

[162] Wenying Shou, Jae Hong Seol, Anna Shevchenko, Christopher Baskerville, Danesh Moazed, ZW Susan Chen, Joanne Jang, Andrej Shevchenko, Harry Charbonneau, and Raymond J Deshaies. Exit from mitosis is triggered by tem1-dependent release of the protein phosphatase cdc14 from nucleolar rent complex. *Cell*, 97(2):233–244, 1999.

[163] Aaron F Straight, Wenying Shou, Gustave J Dowd, Christoph W Turck, Raymond J Deshaies, Alexander D Johnson, and Danesh Moazed. Net1, a sir2-associated nucleolar protein required for rdna silencing and nucleolar integrity. *Cell*, 97(2):245–256, 1999.

[164] Christopher M Gallo, Daniel L Smith, and Jeffrey S Smith. Nicotinamide clearance by pnc1 directly regulates sir2-mediated silencing and longevity. *Molecular and cellular biology*, 24(3):1301–1312, 2004.

[165] Jeffrey S Smith, Carrie Baker Brachmann, Ivana Celic, Margaret A Kenna, Shabazz Muhammad, Vincent J Starai, Jose L Avalos, Jorge C Escalante-Semerena, Charles Grubmeyer, Cynthia Wolberger, et al. A phylogenetically conserved nad+-dependent protein deacetylase activity in the sir2 protein family. *Proceedings of the National Academy of Sciences*, 97(12):6658–6663, 2000.

[166] Jeffrey S Smith, Carrie Baker Brachmann, Lorraine Pillus, and Jef D Boeke. Distribution of a limited sir2 protein pool regulates the strength of yeast rdna silencing and is modulated by sir4p. *Genetics*, 149(3):1205–1219, 1998.

[167] Yihan Lin, Chang Ho Sohn, Chiraj K Dalal, Long Cai, and Michael B Elowitz. Combinatorial gene regulation by modulation of relative pulse timing. *Nature*, 527(7576):54–58, 2015.

[168] Jeremy E Purvis, Kyle W Karhohs, Caroline Mock, Eric Batchelor, Alexander Loewer, and Galit Lahav. p53 dynamics control cell fate. *Science*, 336(6087):1440–1444, 2012.

[169] John G Albeck, Gordon B Mills, and Joan S Brugge. Frequency-modulated pulses of erk activity transmit quantitative proliferation signals. *Molecular cell*, 49(2):249–261, 2013.

[170] Kunio Kitada, Emi Yamaguchi, and Mikio Arisawa. Cloning of the candida glabrata trp1 and his3 genes, and construction of their disruptant strains by sequential integrative transformation. *Gene*, 165(2):203–206, 1995.

[171] Julie Huang and Danesh Moazed. Association of the rent complex with nontranscribed and coding regions of rdna and a regional requirement for the replication fork block protein fob1 in rdna silencing. *Genes & development*, 17(17):2162–2176, 2003.

[172] R Daniel Gietz and Robert H Schiestl. Quick and easy yeast transformation using the liac/ss carrier dna/peg method. *Nature protocols*, 2(1):35, 2007.

[173] Ieong Wong and Chih-Ming Ho. Surface molecular property modifications for poly (dimethylsiloxane)(pdms) based microfluidic devices. *Microfluidics and nanofluidics*, 7(3):291, 2009.

[174] Keir Boxshall, Min-Hsien Wu, Zheng Cui, Zhangfeng Cui, John F Watts, and Mark A Baker. Simple surface treatments to modify protein adsorption and cell attachment properties within a poly (dimethylsiloxane) micro-bioreactor. *Surface and Interface Analysis: An International Journal devoted to the development and application of techniques for the analysis of surfaces, interfaces and thin films*, 38(4):198–201, 2006.

[175] Octavio Mondragón-Palomino, Tal Danino, Jangir Selimkhanov, Lev Tsimring, and Jeff Hasty. Entrainment of a population of synthetic genetic oscillators. *Science*, 333(6047):1315–1319, 2011.

[176] Arthur Prindle, Phillip Samayoa, Ivan Razinkov, Tal Danino, Lev S Tsimring, and Jeff Hasty. A sensing array of radically coupled genetic 'biopixels'. *Nature*, 481(7379):39–44, 2012.

[177] Bridget L Baumgartner, Matthew R Bennett, Michael Ferry, Tracy L Johnson, Lev S Tsimring, and Jeff Hasty. Antagonistic gene transcripts regulate adaptation to new growth environments. *Proceedings of the National Academy of Sciences*, 108(52):21087–21092, 2011.

[178] Chung Sze Luke, Jangir Selimkhanov, Leo Baumgart, Susan E Cohen, Susan S Golden, Natalie A Cookson, and Jeff Hasty. A microfluidic platform for long-term monitoring of algae in a dynamic environment. *ACS synthetic biology*, 5(1):8–14, 2016.

[179] Garrett Graham, Nicholas Csicsery, Elizabeth Stasiowski, Gregoire Thouvenin, William H Mather, Michael Ferry, Scott Cookson, and Jeff Hasty. Genome-scale transcriptional dynamics and environmental biosensing. *Proceedings of the National Academy of Sciences*, 2020.

[180] Alon Zaslaver, Anat Bren, Michal Ronen, Shalev Itzkovitz, Ilya Kikoin, Seagull Shavit, Wolfram Liebermeister, Michael G Surette, and Uri Alon. A comprehensive library of fluorescent transcriptional reporters for escherichia coli. *Nature methods*, 3(8):623–628, 2006.

[181] Horst Feldmann. *Yeast: molecular and cell biology*. John Wiley & Sons, 2011.

[182] Johannes P van Dijken, Ruud A Weusthuis, and Jack T Pronk. Kinetics of growth and sugar consumption in yeasts. *Antonie van leeuwenhoek*, 63(3-4):343–352, 1993.

[183] J Richardson Dickinson. *Metabolism and molecular physiology of Saccharomyces cerevisiae*. Taylor & Francis, 1998.

[184] J Patrick Murphy, Ekaterina Stepanova, Robert A Everley, Joao A Paulo, and Steven P Gygi. Comprehensive temporal protein dynamics during the diauxic shift in saccharomyces cerevisiae. *Molecular & Cellular Proteomics*, 14(9):2454–2465, 2015.

[185] Paola Picotti, Bernd Bodenmiller, Lukas N Mueller, Bruno Domon, and Ruedi Aebersold. Full dynamic range proteome analysis of s. cerevisiae by targeted proteomics. *Cell*, 138(4):795–806, 2009.

[186] Joseph L DeRisi, Vishwanath R Iyer, and Patrick O Brown. Exploring the metabolic and genetic control of gene expression on a genomic scale. *Science*, 278(5338):680–686, 1997.

[187] Rodrigo Diaz-Ruiz, Michel Rigoulet, and Anne Devin. The warburg and crabtree effects: On the origin of cancer cell energy metabolism and of yeast glucose repression. *Biochimica et Biophysica Acta (BBA)-Bioenergetics*, 1807(6):568–576, 2011.

[188] Alon Zaslaver, Avi E Mayo, Revital Rosenberg, Pnina Bashkin, Hila Sberro, Miri Tsalyuk, Michael G Surette, and Uri Alon. Just-in-time transcription program in metabolic pathways. *Nature genetics*, 36(5):486–491, 2004.

[189] Amparo Ruiz, Raquel Serrano, and Joaquín Ariño. Direct regulation of genes involved in glucose utilization by the calcium/calcineurin pathway. *Journal of Biological Chemistry*, 283(20):13923–13933, 2008.

[190] Won-Ki Huh, James V Falvo, Luke C Gerke, Adam S Carroll, Russell W Howson, Jonathan S Weissman, and Erin K O'Shea. Global analysis of protein localization in budding yeast. *Nature*, 425(6959):686–691, 2003.

[191] David Wotton, Katie Freeman, and David Shore. Multimerization of hsp42p, a novel heat shock protein of saccharomyces cerevisiae, is dependent on a conserved carboxyl-terminal sequence. *Journal of Biological Chemistry*, 271(5):2717–2723, 1996.

[192] Steffen Kratzer and Hans-Joachim Schüller. Carbon source-dependent regulation of the acetyl-coenzyme a synthetase-encoding gene acsi from saccharomyces cerevisiae. *Gene*, 161(1):75–79, 1995.

[193] DV Klopfenstein, Liangsheng Zhang, Brent S Pedersen, Fidel Ramírez, Alex Warwick Vesztrocy, Aurélien Naldi, Christopher J Mungall, Jeffrey M Yunes, Olga Botvinnik, Mark Weigel, et al. Goatools: A python library for gene ontology analyses. *Scientific reports*, 8(1):1–17, 2018.